Applications of Micromagnetic Simulations for Use in the Development of Novel Magnetic Computer Memory

by

George Lertzman-Lepofsky

Thesis Submitted in Partial Fulfillment of the
Requirements for the Degree of
Bachelor of Applied Science (Honours)

in the
School of Engineering Science
Faculty of Applied Science

SIMON FRASER UNIVERSITY
Spring 2023

Declaration of Committee

Name:	**George Lertzman-Lepofsky**
Degree:	**Bachelor of Applied Science (Honours)**
Thesis title:	**Applications of Micromagnetic Simulations for Use in the Development of Novel Magnetic Computer Memory**
Committee:	**Dr. Erol Girt** Technical Supervisor Professor, Physics
	Dr. Bonnie Gray Academic Supervisor Professor, Engineering Science
	Dr. Michael Adachi Committee Member Assistant Professor, Engineering Science

APPROVAL

Name: George Lertzman-Lepofsky

Degree: Bachelor of Applied Science Honours

Title of Thesis: Applications of Micromagnetic Simulations for Use in the Development of Novel Magnetic Computer Memory

---

Dr. Michael Sjoerdsma, P. Eng.
Acting Director, School of Engineering Science

Examining Committee:

Dr. Erol Girt
Professor, Department of Physics

Dr. Bonnie Gray, P. Eng.
Professor, School of Engineering Science

Dr. Michael Adachi, P. Eng.
Professor, School of Engineering Science

Date Approved: March 23, 2023

Abstract

Traditional transistor memory has saturated all areas of the computer memory market, but leaves much to be desired in certain applications, opening opportunities for new and exciting technologies. In this thesis I expand the existing capabilities of the Physics of Nanomagnetic Materials and Devices lab by informing experimental decisions with the results from micromagnetic simulations, assisting with the ongoing goal of developing novel designs of STT-MRAM. In particular, I investigate and optimize the impact and interplay of each of the known magnetic phenomena and properties on the behaviour of magnetoresistive memory: saturation magnetization, anisotropy, exchange stiffness, interlayer exchange coupling, and thermal stability. Performance is judged quantitatively, considering switching current, switching fields, structure size, and homogeneity of states. This work uses magnum.pi, a proprietary Python library for solving micromagnetic problems using finite-element methods, developed by the Physics of Functional Materials lab of the University of Vienna. Simulated results show that reasonably sized structures undergo magnetic reversal noncoherently and that it is possible to reliably achieve and control a wide range of interlayer angles in synthetic antiferromagnets with careful choices of realistic anisotropy and other material parameters. Finally, simulations show that particular ranges of interlayer coupling strengths lead to substantially decreased switching currents.

Keywords: undergraduate thesis; micromagnetics; simulations; magnum.pi; STT-MRAM; optimization

Dedication

For Baba and Grandpa

Acknowledgements

I owe everything from the words on these pages to the software in which I did this work to the wonderful people around me. I thank Paul Omelchenko for introducing me to micromagnetic theory, Spencer Myrtle for answering constant (and repeated) questions about the lab equipment, and Drs. Bonnie Gray and Michael Adachi for serving on my committee. This work would have been impossible without the generous support and guidance by the authors of magnum.pi, especially Sabri Koraltan and Dr. Claas Abert. I will be forever grateful to Dr. Erol Girt for welcoming me into his lab, the editorial support and guidance he provided for this thesis, and the patience to do another degree with me. This thesis would still just be a blank page without the love, support, and food provided by my parents and my wonderful partner, Amitis Haghdadi.

Table of Contents

List of Tables

List of Figures

Chapter 1

Introduction

While magnetic computer memory dominated the nascent stages of the computing industry, it was quickly supplanted by solid-state, transistor-based, dynamic random-access memory (DRAM) in the mid 1970s [1], relegating magnetic architectures to mass storage media. Now, cheap flash storage drives are again reducing magnetic memory's relevance in consumer electronics. However, recent discoveries allowing the reading and writing of magnetic bits not with magnetic fields, but with currents, have led to a renewed academic and commercial interest in memory of this type. One such design, spin-transfer torque magnetic random-access memory (STT-MRAM), is especially exciting, promising to combine the density and low-cost of DRAM, the performance of static RAM (SRAM), and the non-volatility of hard disk drives [2].

In its simplest implementation, magnetoresistive memory is composed of two layers of ferromagnetic (FM) material separated by a layer of non-magnetic (NM) material. Information (a "one" or a "zero") is stored in the relative orientation of the bulk magnetization of the FM layers, either parallel or antiparallel. The difference in orientation is measured by passing a current through the layers, which will encounter a large resistance (when antiparallel) or a small resistance (when parallel), Fig 1.1. If the NM spacer layer is conducting, this effect is known as giant magnetoresistance (GMR) - if it is insulating, this is known as tunneling magnetoresistance (TMR). The use of GMR and TMR is already ubiquitous in spinning disk magnetic hard drives, magnetic sensors, and medical imaging [3]. The two layers are engineered such that the magnetization of one layer is difficult to change (the "Fixed Layer") and the other is easy (the "Free Layer"). Write operations only affect the Free Layer.

The most prevalent recent application of magnetic memory is in hard disk drives, where cells are distributed across the surface of a thin, multi-layered magnetic film on a spinning platter. Write operations are carried out by applying an external magnetic field to saturate the magnetic layer in either direction within minuscule regions. This field is emitted by a mechanical read-and-write head positioned above the disk [4]. The mechanical nature of hard disk drives reduces their serviceable lifetimes, increases auditory noise, and decreases

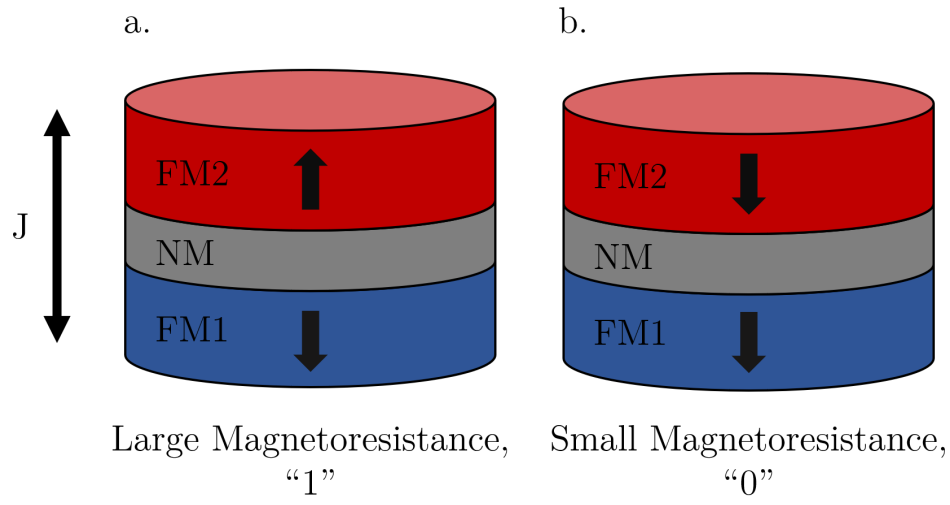

Figure 1.1: A magnetoresistive memory cell. Resistance is high when the ferromagnetic layers are antiparallel (a.) and low when they are parallel (b.), corresponding to the binary memory states "one" and "zero". Resistance is read by either inducing a current through the stack from a field emitter or directly through electrical contacts on the top and bottom.

their read-write speeds—the head must physically move to a given location on the disk while the disk rotates beneath it to read from or write to a bit. However, disk drives are inherently non-volatile (retain information without power), have very high write endurance, and have achieved superb areal densities [4].

There are two types of semiconductor computer memory used in most modern applications: dynamic and static random-access memory (DRAM, SRAM). DRAM is valued for its areal density (consumers can cheaply buy 32GB modules), and low cost, but is volatile: it must be refreshed as often as 31 times per second [5]. This dramatically reduces its power efficiency [6]. Meanwhile, SRAM has superb read/write performance, but is still volatile, has poor areal densities, and is prohibitively expensive in large amounts [7]. Today, DRAM is primarily used for main-memory (storing the operating system and running programs) while SRAM is used for high-speed applications like the central processing unit (CPU) cache, of which there is usually less than 32MB [7, 8].

Combining the physics of memory storage in magnetic moments of spinning disk memory and the reading/writing transistor of DRAM, a single STT-MRAM cell comprises a $\sim$ 50nm diameter nanopillar [9, 10, 11, 12] of layered magnetic material connected to a transistor, Fig 1.2. The primary operational difference (and largest benefit) of STT-MRAM from traditional magnetic drives is in its method of writing. Rather than relying on an external field to reverse the magnetization of a magnetic grain in a thin film, a current is used to both read from and write to a bit. All input/output (I/O) is controlled by the transistor. During write operations, a large current is developed from the Bit to the Source Line. This current passes through the MRAM cell and interacts with the magnetization of the Free

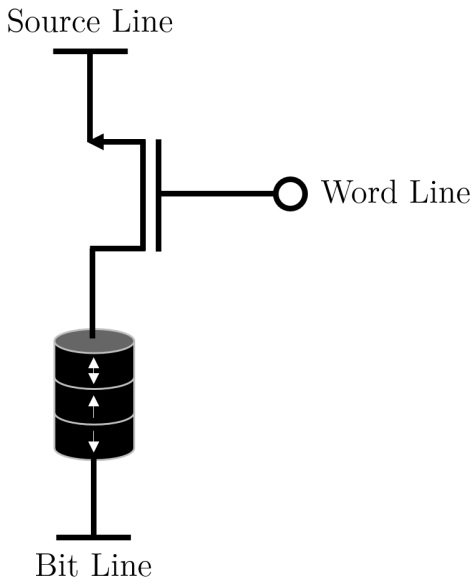

Figure 1.2: A typical control circuit for an STT-MRAM cell embedded in a block of memory. The individual cell is selected and driven by two voltage rails: a Word Line and a Bit Line. To write, a large voltage difference is applied across the Source and Bit Lines, with a voltage on the Word Line large enough to operate the FET in the linear region. This combination drives a large current through the cell, flipping the FL. The direction of the applied current selects the direction of magnetization of the FL and thus the memory state. To read, the FET is still operated in the linear region, but a current only just large enough to measure GMR or TMR (produced by the relative orientation of FM2 and FM3) is developed across the Source and Bit Lines [13]

Layer through an effect known as spin-transfer torque (STT): a spin-polarized current can induce magnetic reversal by exerting a torque on the local magnetic moment [14]. Thus, the direction of the applied current determines the direction of magnetization in the Free Layer. In practice, STT-MRAM devices are often composed of three layers: the free layer (FM3), the fixed layer (FM2), and a coupling layer (FM1). FM1 and FM2 are strongly antiferromagnetically exchange coupled, i.e. their moments are antiparallel. This coupling improves the stability of FM2 and helps to eliminate unwanted stray fields on FM3.

While there *is* widespread industry and academic interest in STT-MRAM [15, 16, 17, 18], all extant commercial offerings fail to realize most of the theorized benefits of the technology: switching currents are unacceptably large and capacities remain small [19]. Reducing the switching current and increasing the writing speed while maintaining short- and long-term thermal stability is of critical importance. It is believed that the introduction of non-collinear coupling (an interlayer angle between 90° and 180°) between the magnetic moments of FM1 and FM2 will substantially improve the performance of STT-MRAM devices in this regard [20, 11], a strategy which is of central focus in the Physics of Nanomagnetic Materials and Devices (PNMD) lab of SFU [21].

The PNMD lab has the experience, knowledge, and equipment for the creation and characterization of thin-film magnetic structures. However, it is difficult to impossible to fully understand or predict the behaviour of certain magnetic structures. Thus, this work informs the ongoing process of optimizing the design parameters of STT-MRAM by simulating existing and planned structures in a specialized micromagnetic simulation environment. Optimization parameters include all relevant magnetic and physical properties: saturation magnetization, interlayer exchange coupling strength, exchange coupling, crystallographic anisotropy, layer dimensions, and externally applied currents and fields. The figures of merit for the optimization of MRAM are switching speed, switching current, structure size, and cost of materials.

Chapter 2

Theory

2.1 Magnetic hysteresis

Ferromagnets are distinguished from other materials in that they generate a field that acts to align internal atomic dipole moments parallel to one another in the absence of an external magnetic field [22]. This is in contrast to materials that exhibit paramagnetic (attractive) or diamagnetic (repulsive) properties only while under the effect of an external field. Likewise, ferromagnetic materials are marked in their non-linear response to an external field, referred to as "hysteresis". This is best shown in a plot of total magnetization in a material, M, against external field, H, Fig 2.1. Clearly, the ferromagnetic material retains some

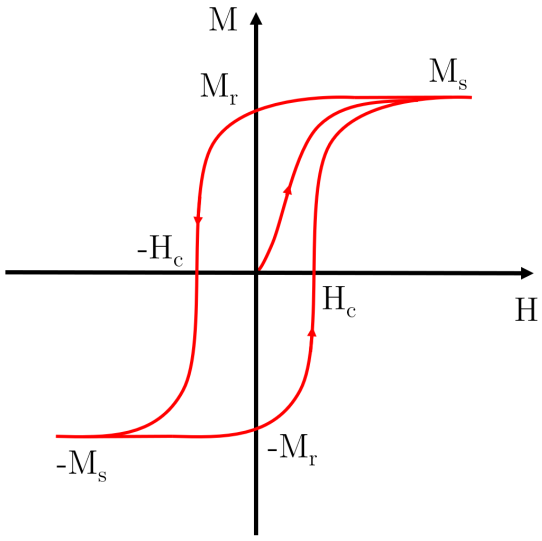

Figure 2.1: A magnetic hysteresis loop for a ferromagnetic material in an external field, with the total magnetic moment, M, plotted as a function of applied external magnetic field, H. Points of interest are labeled, showing the saturation magnetization, M_s, the remanent magnetization, M_r, and the coercivity, H_c.

magnetization even when the external field is removed: the magnetic remanence, M_r. The field required to "coerce" the material into magnetic alignment in either direction is the

coercivity, H_c, while the maximum total magnetic moment achieved at the strongest field is the saturation magnetization, M_s. M_s is an innate property of a given elemental lattice or alloy, while H_c and M_r also depend heavily on the microstructure of a material. The source of the magnetic dipole moment of each atom is thought to be produced by the orbit and quantum mechanical spin of each atom's constituent electrons [23].

2.2 Magnetic free energy

There are many distinct energies present in a magnetic material and the total energy of a given magnetic state is the sum of each. In general, a material will "prefer" to relax into a magnetic state that minimizes these energies. Generally, the total magnetic energy is defined as,

$$E_{Tot} = E_{Ex} + E_{Iex} + E_{Zee} + E_K + E_D, \tag{2.1}$$

where: E_{Ex} = Exchange interaction energy,
E_{Iex} = Interlayer exchange coupling energy,
E_{Zee} = Zeeman energy,
E_K = Anisotropy energy,
E_D = Demagnetization energy.

For brevity, only short descriptions and mathematical definitions of each term will be included here. More complete definitions and derivations can be found in the citations.

2.2.1 Exchange energy

Exchange energy arises completely from the quantum mechanical interactions of the spins of neighbouring atoms (i.e. magnetic dipoles) in a crystal lattice. It is a combination of both the Pauli exclusion principle and the principle of indistinguishable particles [24].

For select FCC and BCC lattice directions, the energy of the exchange interaction is given by [24, 25]:

$$E_{Ex} = \frac{-2A_{Ex}}{d} \sum_{i=1}^{N} \cos\left(\theta_i - \theta_{i+1}\right), \tag{2.2}$$

where: A_{Ex} = Exchange stiffness,
d = spacing between between atomic planes in the lattice,
N = number of lattice planes,
θ_i = angle of the atomic spin in plane i.

Although its value is most often taken from empirical measurements, the exchange stiffness, A_{Ex}, is defined as follows [25],

$$A_{Ex} = \frac{nJS^2}{a}, \tag{2.3}$$

where: n = number of atoms in the unit cell,
J = exchange interaction integral,
S = magnitude of spin.

The value of A_{Ex} captures much of the underlying physics. Its magnitude depends on the lattice constant, the type of unit cell, the number of nearest neighbours, and the strength of interaction between two neighbouring magnetic atoms.

2.2.2 Interlayer exchange energy

Where the exchange energy represents the strength of coupling between individual atomic planes in a ferromagnet, the *interlayer* exchange energy represents the strength of coupling between layers of magnetic material separated by a non-magnetic spacer layer.

Interlayer exchange coupling is most commonly modeled phenomenologically, where the coupling is thought to arise from multiple sources. It can be expressed as [21],

$$E_{Iex} = J_1 \cos(\theta) + J_2 \cos^2(\theta), \tag{2.4}$$

where: J_1 = bilinear coupling constant,
J_2 = biquadratic coupling constant,
θ = angle between the magnetic moments of the coupled layers.

As this energy term is of particular interest in this work, a plot of its behaviour is shown in Fig 2.2. Interlayer exchange coupling is best understood in two parts. The bilinear term has energy minima at either 0° or 180° depending on the sign of J_1, where these two angles correspond to the magnetic moments of the layers being either parallel or antiparallel. The antiparallel case is sometimes referred to as a synthetic antiferromagnet (SAF)—"synthetic" because it is not individual neighbouring spins that are antiparallel, but rather neighbouring layers. This is shown in Fig 1.1(a.). Meanwhile, the biquadratic term has minima at 90° and 270°. These two minima are symmetric: they correspond to the layer's moments being perpendicular to each other. When J_2 is zero or very small relative to J_1, the moments of the layers lie along the same line and are referred to as "collinear". However, for,

$$\frac{J_1}{2J_2} < 1, \tag{2.5}$$

the biquadratic term begins to dominate and energy minima somewhere *between* 180° and 90° appear. This is referred to as "non-collinearity". It has been shown experimentally that the strength and sign of the bilinear term (determined by J_1) oscillates depending on the thickness and composition of the spacer as well as the crystallographic structure of the FM layers near the interface [26, 27]. The contribution of the biquadratic term (J_2) is believed to be determined by spatial variations in J_1, the atomic surface roughness of the coupled layers, pin-holes, and loose spins [28]. Additionally, it was recently discovered

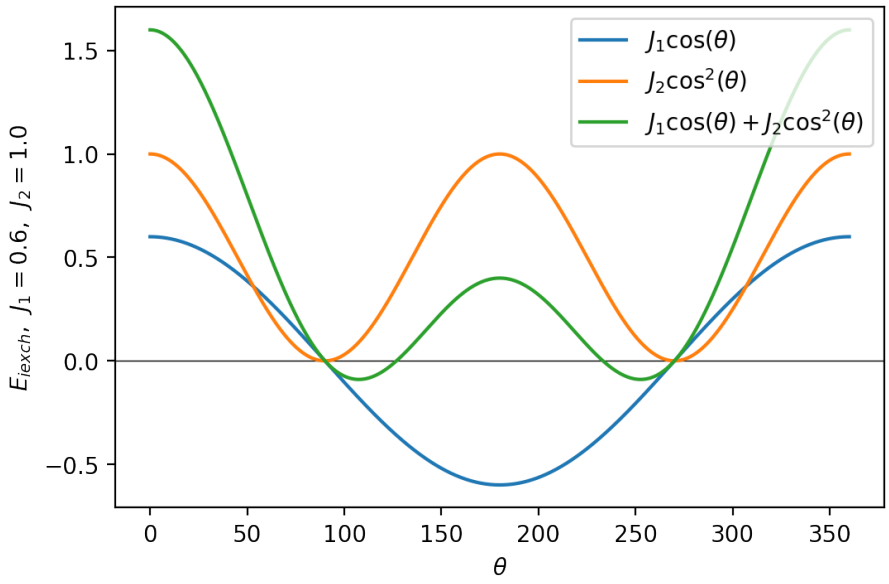

Figure 2.2: Each term of the interlayer exchange energy plotted against coupling angle, along with their sum. Note: the bilinear term (dependent on J_1) has a minimum at 180° (collinear) and the biquadratic term (dependent on J_2) has minima at 90° and 270° (perpendicular). The sum of the bilinear and biquadratic terms has minima between these two extremes, at 107° and 253°. These two minima are symmetric.

that a new class of magnetic spacer layers containing a non-magnetic material (Ru) alloyed with a ferromagnetic material (Fe) can be used to precisely control non-collinear alignment between the magnetic moments of ferromagnetic layers [21].

2.2.3 Zeeman energy

Zeeman energy arises from the interaction of a magnetic material with an externally applied magnetic field. It is a product of the torque exerted on each dipole acting to align them along the field. For the case of homogeneous reversal of a layer, the Zeeman energy per unit area can be defined as [25],

$$E_{Zee} = -M_s H_{Ext} d \sum_{i=1}^{N} \cos\left(\theta_i - \theta_{H_{Ext}}\right), \tag{2.6}$$

where: H_{Ext} = magnitude of the external field,
θ_i = angle of magnetization of an atomic layer,
$\theta_{H_{Ext}}$ = angle of the external field.

Zeeman energy is minimized when the magnetic moment is aligned in the same direction as the field.

2.2.4 Anisotropy energy

Magnetic anisotropy is the tendency of magnetic materials to "prefer" to magnetize along certain directions. Anisotropy can arise from the crystal structure, the quality of the thin film, the local environment in the lattice, and the shape of the magnetic material. Directions (angles of magnetization) where the anisotropy energy is minimized are called "easy", while directions where it's maximized are "hard".

Uniaxial anisotropy

When the easy axis of the material is along a single axis, e.g. the crystallographic direction [0001] for hexagonal close-packed (HCP) Cobalt [13], it is referred to as uniaxial anisotropy, E_{K_u}. This is typically an empirically measured value, but its origin in the structures studied in this thesis can be understood to come from three sources: magnetoelastic (ME), magnetocrystalline (MC), and surface anisotropy (SA) [29]. The films grown in the PNMD lab are all textured (grown along a single crystallographic direction) out-of-plane ($\pm z$). These films consist of magnetic grains that are randomly oriented *within* the film plane. Thus, there is no preferential crystallographic direction in the film plane: the magnetic anisotropy in the x- and y-directions cancel out. For polycrystalline samples, the phenomenological uniaxial anisotropy energy is given by [24],

$$E_{K_u} = -\frac{K_u}{M_s^2} M_\perp^2, \tag{2.7}$$

where: K_u = uniaxial anisotropy constant,
$M_\perp$ = component of magnetization perpendicular to the plane.

ME anisotropy arises at the interface between layers of elements with different lattice constants. This difference induces mechanical stress on the unit cells of both layers, changing the shape, distances, and therefore interaction energies of the constituent particles. So-called because the preferred directions are along crystallographic directions, the magnitude and type of MC anisotropy depends on the crystal lattice in the magnetic material [29]. SA arises due to the asymmetry in the local environment of particles at the edge of a thin film: such a particle does not have a complete set of nearest neighbours [30]. K_u is defined by [13],

$$K_u = K_{ME} + K_{MC} + K_{SA}. \tag{2.8}$$

Shape anisotropy

The aspect ratio of a sample can impose a strongly preferred direction of magnetization. Shape anisotropy arises because unpaired magnetic dipoles at the surfaces of materials create a magnetic field *against* the direction of overall magnetization, giving rise to an internal "demagnetizing field". Unpaired dipoles are maximized when pointing out of the

plane of a thin film rather than parallel to the surface, so the easy axis of a thin film is typically in-plane. The shape anisotropy energy is defined as [13],

$$E_{K_s} = N\frac{\mu_0}{2}M_s^2\cos^2(\theta), \tag{2.9}$$

where: N = demagnetizing factor, a function of the sample aspect ratio,
θ = angle between the magnetization and the sample surface normal.

For a thin film magnetized out-of-plane, which is a good approximation of the structures discussed in this thesis, this becomes,

$$E_{K_s} = \frac{\mu_0}{2}M_s^2. \tag{2.10}$$

The length scale of the exchange interaction (defined above) is limited by its competition with shape anisotropy. This defines the exchange length, which is the shortest scale over which neighbouring spins are homogeneous, given by [29],

$$\delta_{Ex} = \sqrt{\frac{A_{Ex}}{\mu_0 M_s^2}}, \tag{2.11}$$

where: μ_0 = permeability of free space.

δ_{Ex} is directly related to the exchange stiffness and inversely related to the demagnetization, M_s^2.

Effective anisotropy

In practice, the combined effect of E_{K_u} and E_{K_s} is considered most relevant—whichever is larger will dominate and determine the relaxed state. This gives rise to a quantity known as the "effective anisotropy" energy, defined as,

$$E_{K_{Eff}} = E_{K_u} - E_{K_s}. \tag{2.12}$$

Thermal stability

An energy input is required to overcome the energy barrier between easy directions of magnetization and induce magnetic reversal. Thermal energy is present in magnetic systems at all temperatures above 0 Kelvin, which acts to increase the probability of stochastically "jumping" over this barrier in a given timescale. While an increase in thermal fluctuations has been shown to reduce switching currents in STT-MRAM, it also increases the bits' susceptibility to unintentional switching. The probability of random thermal switching in a given time is given by [31],

$$p(t) = f\exp\left(-\frac{E_b}{k_B T}\right) < 1, \tag{2.13}$$

where: $p(t)$ = probability of switching in t time,
f = gyro-magnetic spin precession frequency,
E_b = energy barrier of switching,
k_B = Boltzmann constant,
T = absolute temperature.

This probability increases with increasing temperature and decreases with increasing magnetic energy. The expression can be rearranged to give the thermal stability factor, Δ, which is a key design parameter for STT-MRAM. It is given by [32],

$$\Delta = \frac{E_b}{k_B T} = \frac{K_{eff} V}{k_B T}, \tag{2.14}$$

where: Δ = thermal stability factor,
V = volume of material.

To prevent a single bit from flipping over ten years (a standard figure for hard disks), we require $\Delta \geq 45$ at room temperature [32]. For a 128Mb memory chip to maintain data integrity of each bit over this same period, we require at least $\Delta \geq 59$ [31]. This work will exclusively treat with structures well above this critical value.

2.3 Dynamics

2.3.1 Landau-Lifshitz-Gilbert equation

The interplay between the above energy terms defines the preferred static direction of magnetization at each point of a magnetic material, but it makes no statement about the dynamic process of *reaching* that state. The physical process of changing the orientation of a magnetic moment is described by the Landau-Lifshitz-Gilbert equation (LLG), given by [33],

$$\frac{d\vec{M}}{dt} = -\frac{\gamma}{1+\alpha^2}\vec{M} \times \vec{H}_{Eff} - \frac{\alpha\gamma}{1+\alpha^2}\vec{M} \times \left(\vec{M} \times \vec{H}_{Eff}\right), \tag{2.15}$$

where: $\vec{M}$ = magnetization,
γ = reduced gyromagnetic ratio,
α = damping,
$\vec{H}_{Eff}$ = effective field.

This relates the change in magnetization to both the current magnetization and a quantity called the "effective field". This effective field is in fact the combination of all of the effects of minimizing the energy terms defined above, modeled as a field acting to align the magnetic moment in a single direction. It is defined as [33],

$$H_{Eff} = -\frac{1}{\mu_0 M_s}\frac{\delta E}{\delta M}, \tag{2.16}$$

where this is a variational derivative of energy in magnetization. Importantly, the LLG shows that magnetic moments do not simply "snap" along the direction of H_{Eff}. Instead, in a combination of precessional and dissipative motion, they spiral in towards an energetic minimum [33]. The speed of precessional decay is controlled by the damping, α. As well, thermal energy causes some degree of perpetual precession about the direction of H_{Eff}.

2.3.2 Spin-dependent scattering

Each energy state of a system is degeneratively filled by one spin-up and one spin-down electron. In the ground state, every state is occupied by a pair of electrons up to a certain level, the Fermi energy, E_f. The number of electrons in each energy interval is often represented by a function, the density of states, $D(E)$. For a non-magnetic material, the density of states function is symmetric for both spin-up and spin-down electrons, i.e. there are equal populations of occupied states for both spins, Fig 2.3(a.). However, magnetic materials are "spin-polarized"—there is a preponderance of one electron spin, lending to a net overall polarization of atoms, Fig 2.3(b.). Importantly, the shape of $D(E)$ at E_F, and thus the population of locally unfilled states, is different for spin-up and spin-down electrons [34].

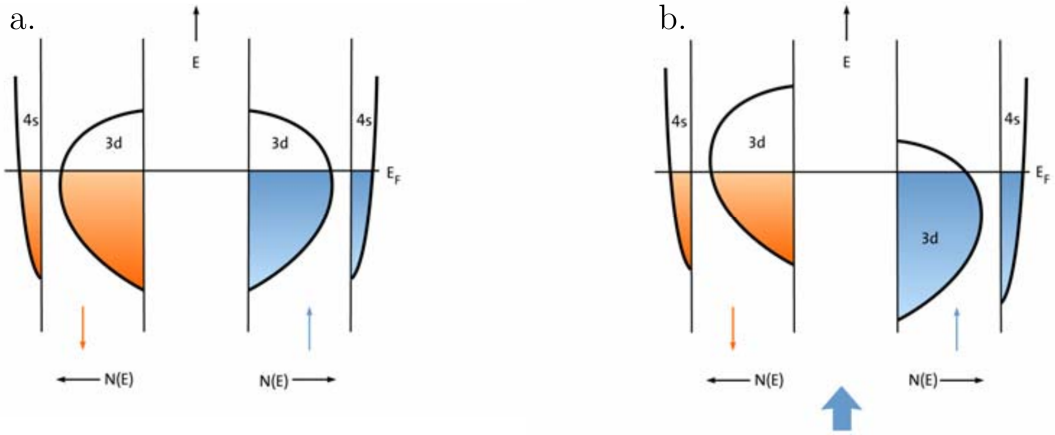

Figure 2.3: A schematic representation of the density of states, $D(E)$ (here referred to as $N(E)$), of a non-magnetic d-transition metal (a.) and of a ferromagnetic d-transition metal (b.). The thin blue and orange arrows indicate the directions of electron spin, the large blue arrow indicates the direction of magnetization in (b.). Note that in (a.), the density of states and occupied states at E_F is symmetric for spin-up and spin-down electrons, where in (b.), $D(E)$ is skewed. There are more occupied states of spin-up electrons. Adapted from [34].

The d-transition metals have both 3d and 4s valence electrons that contribute to conduction. However, it is only the behaviour of the 3d electrons that contributes to the unique ferromagnetic properties of Fe, Co, and Ni [34]. Mott theorized that while the s-electrons have high mobility, they are heavily scattered into the many available d-states at E_F, increasing their felt resistance [34]. Similarly, depending on spin, the d-electrons have differing numbers of available states at E_F to which they can scatter. Thus, spin-up and spin-down

electrons experience a difference in resistance in magnetized materials. This imbalance in resistance has a filtering effect on applied currents, where a majority of the non-scattered conduction electrons have spin along the direction of local magnetization [13]. Sometimes, in a parallel to semiconductor devices, the more and less common spins in a spin-polarized current are called "majority" and "minority" carriers, respectively.

Giant magnetoresistance

Two ferromagnetic layers (FM1 and FM2) coupled across a non-magnetic spacer can relax to one of two homogeneous states: parallel and antiparallel. As above, a current applied to FM1 will pick up a degree of spin-polarization, i.e. conduction electrons with spin *not* in the direction of magnetization of FM1 will be preferentially scattered, leaving a majority of aligned electrons. In the parallel case, as this current passes through the spacer and into FM2, it encounters the same electronic band structure as in FM1 and the majority spins do not scatter further. In contrast, the minority spin electrons are scattered strongly within *both* layers. This situation mirrors a parallel circuit with a low-resistance and a high-resistance path: the measured resistance in this case is low. In the antiparallel configuration, both spin-up *and* spin-down electrons are scattered strongly in one of the layers, because they are antiparallel to the direction of magnetization in at least one magnetic layer. This mirrors a parallel circuit with two paths of equal, moderate resistance [34]. Measured resistance in this case is high. The dependence of resistance on magnetization, giant magnetoresistance (GMR), is most often quantified as the ratio of the resistance of the antiparallel state to the parallel state. GMR is not used in the results of this work, but is an important aspect of the function of STT-MRAM.

Spin-transfer torque

Consider again the arrangement in Fig 1.1(a.), being cognizant that FM1 is "hard" (high anisotropy - difficult to reverse) and FM2 is "soft" (low anisotropy - easy to reverse). In the case where a current is passed through FM1 to FM2, the current is spin-polarized with the majority carriers being in the direction of FM1's magnetization. This current passes into FM2, where many of the majority carriers interact with the local magnetic moment by exerting a torque on the spins in FM2. This causes them to precess. If the magnitude of the applied current is sufficient, this torque can cause the spins in FM2 to switch direction *en masse* to a parallel state, Fig 1.1(b.) [33, 29]. Note that as the spin-polarized current passes through the spacer, minority carriers from FM2 are reflected back into FM1. However, for the antiparallel configuration, the minority carriers of FM2 are parallel to FM1. These reflected carriers only act to stabilize FM1 [33].

The inverse operation is slightly different: it relies on the interaction of minority carriers reflected back at FM2. When parallel, current is instead passed *from* FM2 to FM1. As before, the current is spin-polarized with majority carriers along FM2's direction of magnetization.

As this current passes through the spacer and into FM1, it again exerts a torque on FM1 and causes a stream of carriers *antiparallel* to FM1 (and thus FM2) to reflect back at FM2 [33]. These reflected carriers exert a torque on FM2 in the opposite direction to its magnetization. FM2 is softer than FM1, so it succumbs to the applied spin-transfer torque (STT) at lower currents than FM1 and returns to an antiparallel state [13, 33].

STT is considered to contribute a "fieldlike" torque that causes precession and a "dampinglike" torque that causes alignment of the layer with the polarized current [33],

$$\vec{T}_{field} = \eta_{field}\left(\theta\right)\frac{j_e\hbar}{2e\mu_0 M_s}\vec{M}\times\vec{P}, \quad \vec{T}_{damp} = \eta_{damp}\left(\theta\right)\frac{j_e\hbar}{2e\mu_0 M_s}\vec{M}\times\left(\vec{M}\times\vec{P}\right), \tag{2.17}$$

where: η_{damp} = angular dependence of the damping-like torque,
η_{field} = angular dependence of the field-like torque,
j_e = current density,
$\hbar$ = reduced Plank constant,
e = electron charge,
$\vec{M}$ = magnetization of FM2,
$\vec{P}$ = spin-polarized current due to the magnetization of FM1.

These two components can be expressed as an effective field, similar to the static magnetic energies, and are incorporated into the LLG as follows [33, 35]:

$$\begin{aligned}\frac{d\vec{M}}{dt} = &-\frac{\gamma}{1+\alpha^2}\vec{M}\times\left[\vec{H}_{Eff}+\frac{j_e\hbar}{2e\mu_0 M_s}\left(\alpha\eta_{damp}-\eta_{field}\right)\vec{P}\right] \\ &-\frac{\alpha\gamma}{1+\alpha^2}\vec{M}\times\left(\vec{M}\times\left[\vec{H}_{Eff}+\frac{j_e\hbar}{2e\mu_0 M_s}\times\left(-\frac{1}{\alpha}\eta_{damp}-\eta_{field}\right)\vec{P}\right]\right).\end{aligned} \tag{2.18}$$

Importantly, the magnitude of the dampinglike torque exerted on a magnetic moment by a spin-polarized current is proportional to the cross-product between $\vec{M}$ and $\vec{P}$ (Eq. 2.17), which represents the angle between the spins in the current and the local magnetic moment, and is "0" when $\vec{M}$ and $\vec{P}$ are parallel. If the biquadratic coupling constant, J_2, were zero, the only source of non-collinearity between FM1 and FM2 would be the random thermal motion of the magnetic moments of the ferromagnetic layers. Thus, thermal instability and non-collinearity induced by J_2 tend to decrease the switching current [20]. In summary, one can read and write both memory states of a magnetic bit just through the actions of GMR and STT by simply varying the direction and magnitude of current through the cell.

Chapter 3

Methods

3.1 Simulations

3.1.1 magnum.pi

For large-scale and comprehensive micromagnetic simulations, there are a number of open-source and proprietary options available. For this work, I have been generously granted access to a proprietary Python package called "magnum.pi" [36, 37], developed by the Physics of Functional Materials (PFM) lab at the University of Vienna [38]. The PNMD lab and this group have a close working connection.

In short, magnum.pi is an accurate and fast tool where one can simulate all of the dynamic and static effects discussed above and more. It includes accurate numerical implementations of each energy term and material parameter. Its inputs are a meshed 3D model of the structure-in-question and a Python script to customize, run, and log the parameters of a given simulation. Its output is a series of files containing the vector and scalar results at each of a finite number of points in the structure. Exactly which and how many results are sampled from the parameter space is completely up to the user. Output from the simulation can be viewed pictorially in ParaView (see Section 3.1.2) or quantitatively in a plotting environment of the user's choice. As an example, I have provided the results of simulating an interlayer exchange coupled SAF with positive J_1 in magnum.pi, shown in Fig 3.1. For the given material parameters, the structure relaxed (fell into an energy minimum) corresponding to a collinear SAF.

magnum.pi is in the minority of existing micromagnetic simulation software in that it employs finite element (FEM), rather than finite difference (FDM), numerical methods [33, 39]. This is important, as a numerical derivative (as in FDM) has inherent loss of granularity and introduces instability at certain boundary conditions. magnum.pi's approach to micromagnetic modeling is similar to the mechanical stress/strain/deformation modeling that one might perform in SolidWorks or Ansys. FEM introduces another step before simulation, meshing, where one employs additional software to construct a tetrahedral mesh of a custom-made 3D model of one's structure. Tetrahedral meshes (as in FEM)

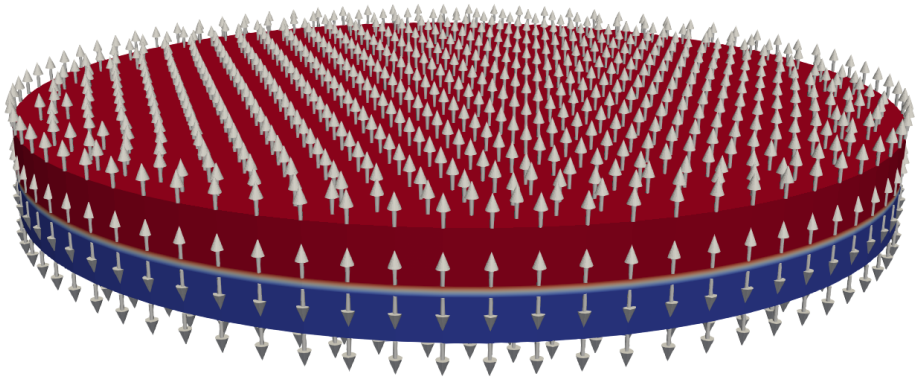

Figure 3.1: Sample simulation results from magnum.pi displayed in Paraview. This is a simple SAF, with the direction of overall magnetization of a layer indicated by the colour (red for +z and blue for -z) and the direction of each node's spin shown with an arrow. The spacer is white (no overall magnetization). Note: this is a still from a set of results spanning about 5ns of simulation time. The complete behaviour of this simulation is visible either in Paraview or as a GIF.

achieve substantially higher resolution than cuboids (as in FDM), even for fewer meshing vertices [33]. In this case, the meshing model is an accurate to-scale recreation of the structures we are interested in simulating, including the layer thicknesses, shapes, and volumes. Magnetic states are calculated at each corner of each tetrahedron, called a vertex. To most accurately model the behaviour of an individual spin, it is important that the side lengths of these tetrahedra (called the mesh length) do not exceed the exchange length, Eq. 2.11. In this work I use Gmsh, a free and open-source command-line or graphical meshing tool [40]. Gmsh's input is a ".geo" file, which contains all of the physical information about the structure. An example Gmsh meshing file is provided in Appendix A.

Competing micromagnetic simulation environments include the Object-Oriented Micromagnetic Framework (OOMMF) [41] and mumax^3 [42]. Both are free and open-source, however, neither framework has any native support for simulations involving the biquadratic coupling constant. Both OOMMF and mumax^3 are GPU-capable, while magnum.pi is bound to the CPU.

3.1.2 ParaView

Paraview is an open-source software platform for data visualization. It is not required to use magnum.pi, but it does allow users to create especially intuitive and attractive output files, as in Fig 3.1. The user has complete control over which logged results are displayed, and these can include any of the magnetic properties that magnum.pi simulates, including anisotropy, magnetization, and demagnetization in any specific direction. As illustrated by Fig 3.1, the user can choose to map either a colour gradient or a "glyph" (the arrows) to the magnetization measured at each vertex of the simulation mesh.

3.1.3 HPC

Unfortunately, while OOMMF and mumax^3 can be run on any Windows desktop computer with a consumer-grade GPU and CPU, magnum.pi can only be run on Linux environments. As well, the simulations that are required of this work require substantially more computing power than is supplied by typical computers. Accordingly, I have been granted access to the Compute Canada High Performance Computing (HPC) network [43]. This allows me the use of multiple supercomputing clusters across Canada, in particular *Cedar*, which is located on the Simon Fraser University (SFU) campus. This HPC cluster has an overwhelming amount of computing power (a theoretic peak double-precision performance of 14 PFlop/s [44]), but its effective use is locked behind a fairly substantial learning curve. This includes the development of batch scripts, the submission and optimization of SLURM Workload Manager jobs (see Appendix B for an example) [45], management of the SLURM queue, efficient storage and archival of massive amounts of research data on a Lustre filesystem [46], and the use of Gentoo Linux [47].

3.2 Experiment

3.2.1 Sample fabrication

The fabrication techniques of the PNMD lab are currently limited to sputter deposition, though there is ongoing work to apply electron-beam lithography and directional etching techniques to manufacture STT-MRAM nanopillars in-house. Sputtering is one of many processes by which one can deposit films of a material from a source (the target) onto a sample (the substrate). In this case, sputtered materials are a range of magnetic and non-magnetic elements, including Fe, Ni, Co, Cu, Ru, Ta, and Pt, which together contribute the range of magnetic material properties required for the PNMD lab's structures. Sputtering is an ablative process, where positively charged ions of an non-reactive plasma (usually Ar) are accelerated toward a negatively charged target, knocking off neutral atoms on impact. These uncharged target atoms fly away in a largely random direction, some of which happen to land on and cover the substrate. Sputtering is typically performed at high vacuum (less than 1.33×10^{-6}Pa) to minimize any chance of scattering the substrate atoms and impurities in the sputtered film.

Our samples are predominantly prepared using radio-frequency (RF) magnetron sputtering. The details of the mechanism by which this method works are unimportant for this thesis, but it is sufficient to know that by employing an alternation field one can sputter non-conducting materials and that magnets beneath the target increase film purity and sputter rates.

3.2.2 VSM

Vibrating-Sample Magnetometry (VSM) is the primary method by which our lab obtains empirical material classifications. Combined with appropriate analysis, VSM data will report values for M_s, M_r, H_c, K_u, J_1, J_2, and A_{Ex} for individual layers of magnetic material and some types of coupled structures.

Internally, the VSM applies a strong magnetic field to the sample. The sample is then mechanically vibrated, producing an oscillatory magnetic field around the sample. This field is picked up by a pair of coils as an induced voltage, the magnitude of which is proportional to the magnetic moment of the sample multiplied by its volume [25]. The external field is swept from positive to negative H_c, ensuring that the magnetic moment is fully saturated in both field directions. One must normalize the results by the volume of the deposited magnetic layers to isolate the magnetic moment. All material parameters given to magnum.pi as inputs in this work are taken from measurements of PNMD samples from the VSM.

3.2.3 MOKE

Where the VSM is a quantitative approach, the Magneto-Optical Kerr Effect (MOKE) can provide a holistic picture of the magnetic hysteresis (and therefore switching behaviour) of a complex magnetic sample, very similar to Fig 2.1. However, its results are entirely relative—they contain no absolute values for M_s and M_r. Combined with the VSM, however, one can obtain a complete picture of the behaviour of sample. As well, because MOKE is an optical method, its results are very sensitive to the conditions at the surface of the film.

The Kerr effect describes the phenomenon that light interacting with a magnetic material can change its polarization. The MOKE experimental setup involves placing a magnetic sample in a large external field, where polarized laser light is reflected off of it. The reflected beam is then passed through a second polarizer, polarized perpendicularly to the first. For a non-magnetic material, this would completely filter all the light. For magnetic materials, however, any measured residual light is then the result of a change in polarization *caused* by the interaction with the material itself. The intensity of the measured light is thus positively related to the magnetization at that particular external field. To obtain a full hysteresis loop, the field is swept forward and back past the saturation field of the sample in both directions.

3.2.4 Van der Pauw method

The Van der Pauw method is the most common method by which one measures sheet resistance (which gives the GMR/TMR ratio). It is a four-point probe method, wherein current is produced between two probes and voltage is measured across the others. Ohm's law then gives total resistance, which is related to sheet resistance, R_s, by [13],

$$R_s = \frac{\pi R_{av}}{\ln 2} f, \tag{3.1}$$

where: R_{av} = average of the resistance between each pair of probes,
f = correction factor for asymmetries in the sample resistance.

To summarize, magnum.pi can be used to predict structure behaviour, sputtering is used to fabricate samples, and VSM, MOKE, and GMR are used to obtain empirical values to act as inputs to magnum.pi.

3.3 Optimization of STT-MRAM

Commercial MRAM devices were first made available on the consumer market in 2006, by Freescale Semiconductor [16] and later by Everspin Technologies [15]. Neither product line has achieved large-scale success, primarily due to their low areal densities and high power draw. These issues, in addition to cost, scalability, and speed are of fundamental concern in the PNMD lab's research.

As mentioned briefly above, it is vital that FM3 does not feel any stray field from FM2. If it does, it would introduce anisotropy in the switching current, i.e. it would require different current densities to write a "1" or a "0" because of the bias in internal field. By coupling FM2 to a very hard third layer, FM3, we can improve the stability of FM2 during write operations and, if M_s is tuned to match, completely eliminate any stray fields felt by FM3. This tuning is accomplished by adjusting M_s/V (the saturation magnetization normalized by volume) for FM1 and FM2 so that when FM1 and FM2 are antiparallel, their stray fields cancel out. As well, because FM1 is slightly farther from FM3 than FM2, M_{s_3} must be slightly larger to completely cancel the stray fields.

There is a very real material cost to magnetic devices. Where semiconductor devices are primarily bulk silicon, precious rare-earth metals like Pt and Ru are commonplace in MRAM structures. Therefore, the overall diameter and thickness of the design must be kept at minimum. This is limited by manufacturing techniques, thermal stability, and film homogeneity.

Switching current, device scalability, and size are all interdependent: the primary limitation on the density of STT-MRAM chips is the size of the driving transistor [48], as shown in Fig 1.2. Existing devices require large currents to write to bits, which in turn requires a large transistor. This increases power draw, increases heat production, and decreases density [49]. To address this shortcoming, it is a common strategy to deliberately *worsen* (decrease) the thermal stability of the memory cells, causing the constituent dipoles to develop a very large random precession [19]. This is in an effort to create non-zero spin-transfer torque at the beginning of the switching process—decreasing switching current and increasing switching speed. While necessary to increase density, this has disastrous effects on the memory's long-term stability: Everspin's 1Gb device is only rated for three months of data retention [50]. This is no-longer considered non-volatile by industry standards.

The key design element of PNMD's memory is the development of a large STT moment arm not through random thermal motion, but through careful optimization of material parameters to produce a naturally non-collinear and thermally stable FM2. In simulations, this has already been shown to cause a two times reduction in switching current and a three times reduction in switching speed [19]. This is of course paired with a decrease in transistor size, which in turn improves areal density and heat management.

Given that the PNMD lab is at the forefront of knowledge and capability to fabricate biquadratically coupled structures at particular angles, understanding the optimization of these structures in nanopillars is of central importance to us. Thus, a focal question of my work is, "how does one design an STT-MRAM structure to maximize the benefits of non-collinearity between FM2 and FM3?"

Chapter 4

Results

4.1 Static simulations

4.1.1 Verification of magnum.pi and exploration of design parameters

In this first set of simulations, my objectives were to verify the behaviour of each energy term as implemented in magnum.pi, demonstrate my own ability and understanding of the physics involved, and determine a few key design parameters of STT-MRAM. All aspects of magnum.pi behaved correctly, as expected, with the exception of the biquadratic coupling term, a bug in which was discovered and subsequently fixed through personal communications with Dr. Abert of the PFM lab.

Selection of structure dimensions: single domain radius

It is necessary that all layers of the MRAM cell have homogeneous relaxation states for the stability and uniformity of the devices, i.e. each layer must be a single magnetic domain. This condition is determined by the single-domain radius, given by [29],

$$R_{sd} = 36\frac{\sqrt{A_{Ex}K_u}}{\mu_0 M_s^2}, \tag{4.1}$$

which gives an upper bound on structure size. Experimental values for the dependencies of this equation are well known for the elements and alloys used in PNMD's structures, so the maximum radius of the nanopillar is trivial to calculate.

Table 4.1 contains the maximum layer radius under this condition for select values of K_u. $A_{ex} = 1.3 \times 10^{-11}$J/m here and for all subsequent simulations, unless stated otherwise, which is appropriate for bulk Cobalt [25]. M_s is chosen to be 900×10^3A/m and FM1 and FM2 thickness are chosen to be 3nm to produce results most applicable to existing PNMD measurements. The thickness of the FM1/FM2 spacer is chosen to be 0.5nm for the same reason, though this does not affect coupling strength in magnum.pi as implemented: J_1 and J_2 and *inputs* to the model, rather than arising physically from properties of the

lattice/interface. By the results from Eq. 4.1, the smallest upper bound radius is $\sim$ 70nm, for $K_u = 3.0 \times 10^5 \text{J/m}^3$.

Table 4.1: Single domain radius, R_{sd}, for various values of K_u, selected to cover a range of appropriate values for FM1 and FM2, calculated by Eq. 4.1.

A_{ex} (J/m)	M_s (A/m)	K_u (J/m^3)	R_{sd} (nm)
1.3×10^{-11}	900×10^3	3.0×10^5	69.85
1.3×10^{-11}	900×10^3	5.0×10^5	90.17
1.3×10^{-11}	900×10^3	7.5×10^5	110.4
1.3×10^{-11}	900×10^3	1.0×10^6	127.5

Selection of structure dimensions: thermal stability

Eq. 2.14 gives a lower bound on the layer radius to maintain long-term stability of a memory bit. Table 4.2 contains values for Δ for a range of potentially appropriate values of K_u, layer radius, and layer thickness at room temperature. To improve areal density, it is desired to design for the smallest radius that maintains the $\Delta > 60$ condition, while also being manufacturable: nanopillars as small as 10nm are considered achievable on a large scale [51]. Likewise, it has been shown that out-of-plane structures are preferable for magnetic media, as they have lower switching currents and higher thermal stability than in-plane [52]. To maintain this condition, the perpendicular anisotropy constant, K_u, must always be larger than the shape anisotropy constant, K_s. By the results from Eq. 2.14, values of K_u from $5.0 \times 10^5 \text{J/m}^3$ to $1.0 \times 10^6 \text{J/m}^3$ produce thermal stabilities far in excess of the minimum with realistically minimized layer radii, while $K_u = 3.0 \times 10^5 \text{J/m}^3$ only produces in-plane (albeit stable) magnetizations.

Biquadratic interlayer exchange coupling

Where the many individual magnetic spins of a ferromagnetic layer are treated as one, this is referred to as a "macrospin" model. Such a simple model does not account for non-homogeneity within a material. Where FM1 and FM2 are treated as macrospins with some separation angle θ interacting only through interlayer exchange coupling i.e., in the absence of any kind of crystalline anisotropy or demagnetization field, the relaxation angle is trivial

Table 4.2: Thermal stability figure of merit (Δ) for a range of potentially appropriate values of K_u, r (layer radius), d (layer thickness) at room temperature, calculated by Eq. 2.14. Note that a negative effective anisotropy (K_{eff}) indicates that the layer is magnetized in-plane. A $\Delta > 60$ in this case means that the layer is stable from pointing out-of-plane, but will magnetize along a random direction in-plane, as the layer is isotropic in x-y, which is inapplicable for GMR measurements in STT-MRAM.

K_u (J/m^3)	K_s (J/m^3)	K_{eff} (J/m^3)	r (nm)	d (nm)	T (K)	Δ
3.0×10^5	3.7×10^5	-6.7×10^4	15	3	300	34.4
3.0×10^5	4.0×10^5	-1.0×10^5	20	3	300	90.6
3.0×10^5	4.2×10^5	-1.2×10^5	25	3	300	170
5.0×10^5	3.7×10^5	1.3×10^5	15	3	300	68.0
5.0×10^5	4.0×10^5	1.0×10^5	20	3	300	91.4
5.0×10^5	4.2×10^5	8.0×10^4	25	3	300	114
7.5×10^5	3.7×10^5	3.8×10^5	15	3	300	196
7.5×10^5	4.0×10^5	3.5×10^5	20	3	300	319
7.5×10^5	4.2×10^5	3.3×10^5	25	3	300	470
1.0×10^6	3.7×10^5	6.3×10^5	15	3	300	324
1.0×10^6	4.0×10^5	6.0×10^5	20	3	300	547
1.0×10^6	4.2×10^5	5.8×10^5	25	3	300	825

to calculate through energy minimization:

$$\begin{aligned} E_{Iex} &= J_1 \cos(\theta) + J_2 \cos^2(\theta), \\ \frac{d}{d\theta} E_{Iex} &= \frac{d}{d\theta}\left[J_1 \cos(\theta) + J_2 \cos^2(\theta)\right] = 0, \\ 0 &= -J_1 \cancel{\sin(\theta)} - 2J_2 \cancel{\sin(\theta)} \cos(\theta), \\ \cos(\theta) &= \frac{-J_1}{2J_2}, \\ \theta_{min} &= \arccos\left(\frac{-J_1}{2J_2}\right). \end{aligned} \tag{4.2}$$

It is clear to see that for all values of $J_2 < J_1/2$, $\theta_{min} = 180°$ i.e., perfectly collinear, while for $J_2 > J_1/2$, the minimum is somewhere between 90° and 180° i.e., non-collinear. This formula can be readily used to verify relaxation angles given coupling constants, as shown in Table 4.3.

I created a magnum.pi simulation that, by agreeing with these values, would validate the model: two 25nm radius, 3nm thick magnetic layers separated by a 0.5nm nonmagnetic spacer, with large anisotropy (1×10^6J/m^3) in the bottom layer, a constant J_2 of 1.5×10^{-3}J/m^2, a varying J_1, and no demagnetization. The layers were relaxed from an initial, randomized state for 5ns. These results are shown in Fig. 4.1(a, b, c).

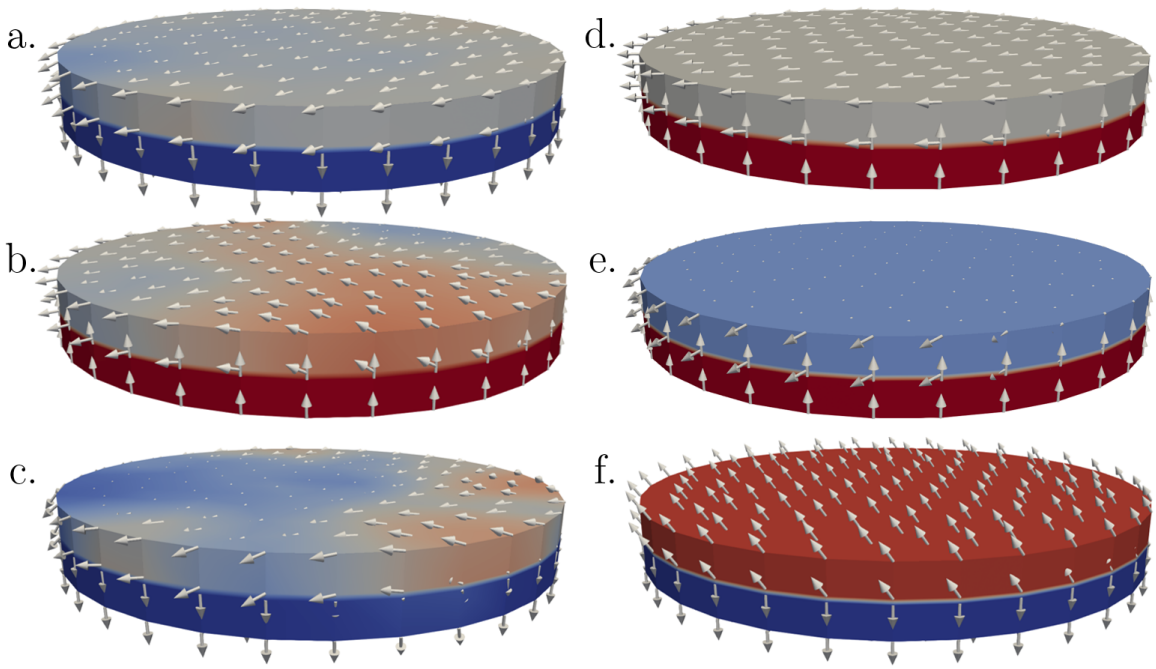

Figure 4.1: Left: initial validation of the interlayer exchange coupling term in magnum.pi, using version 3.8.1, for various values of J_1: $0 \times 10^{-3}\mathrm{J/m^2}$ (a.), $1.5 \times 10^{-3}\mathrm{J/m^2}$ (b.), $2.5 \times 10^{-3}\mathrm{J/m^2}$ (c.), and $J_2 = 1.5 \times 10^{-3}\mathrm{J/m^2}$. Demagnetization was not included, and only FM1 had non-zero anisotropy. One would expect the layers to be homogeneous and relax to 90° (a.), 120° (b.), and 146° (c.), respectively. Instead, the layers are non-homogeneous and have ill-defined coupling angles. Each arrow represents a single magnetic moment, while the colour represents the local average direction of the moment: red for the positive 'z' direction, blue for negative. Right: validation of the interlayer exchange coupling term in magnum.pi, using version 3.9.5, for various values of J_1: $0 \times 10^{-3}\mathrm{J/m^2}$ (d.), $1.5 \times 10^{-3}\mathrm{J/m^2}$ (e.), $2.5 \times 10^{-3}\mathrm{J/m^2}$ (f.), and $J_2 = 1.5 \times 10^{-3}\mathrm{J/m^2}$. Demagnetization was not included, and only FM1 had non-zero anisotropy. One expects the layers to be homogeneously antiparallel and relax to 90° (d.), 120° (e.), and 146° (f.), respectively, which is the case (to within the numerical precision of magnum.pi).

Table 4.3: Interlayer angle, θ_{min}, for a few pairs of values of interlayer exchange coupling constants, J_1 and J_2.

J_1 (J/m^2)	J_2 (J/m^2)	θ_{min}
0	1.5×10^{-3}	90°
1.5×10^{-3}	1.5×10^{-3}	120°
2.5×10^{-3}	1.5×10^{-3}	146°

When there is no demagnetization field and the total anisotropy is perfectly out-of-plane, FM1 is forced to magnetize perfectly perpendicular to the film plane. Meanwhile, if the total anisotropy of FM2 is chosen to be zero, the magnetic moment of FM2 is free to point in any direction in the absence of coupling between the layers. Therefore, any interlayer angle will be entirely due to coupling and will be formed between FM1 and the easy axis of FM2, the z-axis. The magnitude of this angle should, to within the numerical accuracy of Python/magnum.pi, *exactly* match the values in Table 4.3. Instead, Fig. 4.1(a, b, c) shows pronounced non-homogeneity within the layers (rendering any discussion of interlayer angle meaningless) and, where a positive J_1 should force an anti-parallel state, Fig. 4.1(c.) was instead approximately parallel. Note that the two antiparallel configurations (tail-to-tail or tip-to-tip) are energetically equivalent.

This behaviour was brought to the attention of the PFM lab, who realized that there was a software bug in magnum.pi's caching of the biquadratic coupling term that prevented the proper function of the `BiquadraticInterlayerExchangeField` class. This was quickly remedied by Dr. Claas Abert, resulting in a new release of magnum.pi: version 3.9.5 from 3.8.1. The above simulations were rerun using the new release, the results of which are shown in Fig. 4.1(d, e, f) and are exactly as predicted. The measured interlayer angles for these simulated structures are as follows: 90.000°, 119.996°, and 146.433°.

Uniaxial anisotropy

Commercially available STT-MRAM consists of a free and a hard layer magnetized out-of-plane to minimize writing current [52]. The easy directions of magnetization in the structures studied in this work are uniaxial and are due to magnetocrystalline anisotropy. The total magnetocrystalline anisotropy energy within a layer (and thus the magnitude of its effect on the relaxation angle) is directly proportional to the volume of the layer and the anisotropy constant, K_u. The simple model for the energy density of macrospin interlayer exchange coupling in Section 4.1.1 can be extended to include uniaxial anisotropy in both layers as follows, with context provided by Fig. 4.2:

$$E = -K_{u1} d_1 \cos^2(\theta_1) - K_{u2} d_2 \cos^2(\theta_2) + J_1 \cos(\theta_1 - \theta_2) + J_2 \cos^2(\theta_1 - \theta_2). \quad (4.3)$$

Note that this is now a single equation with two unknowns: the two angles of the macrospins with respect to the positive z-axis, θ_1 and θ_2. This makes finding an analytical solution difficult, but energy minimization is still possible through numerical methods.

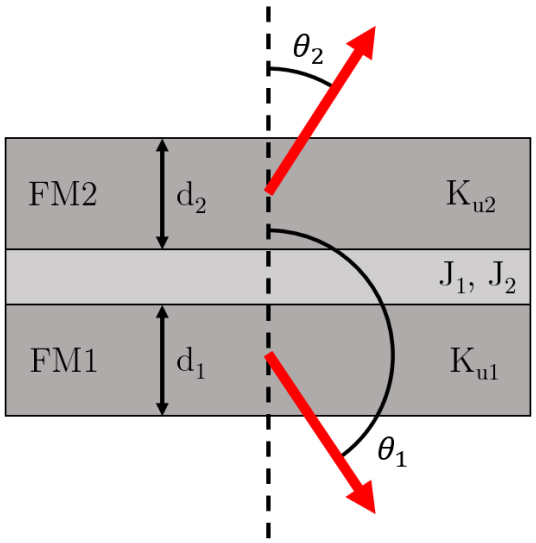

Figure 4.2: Labeled diagram for a macrospin model including uniaxial anisotropies K_{u1} and K_{u2}. d_1 and d_2 are layer thicknesses, while θ_1 and θ_2 are the angles formed by the macrospins with respect to the positive z-axis. J_1 and J_2 are the interlayer coupling coefficients for the interaction between FM1 and FM2, here labeled within a nonmagnetic spacer layer.

To visualize and verify the effect of uniaxial anisotropy on the relaxation of a SAF in magnum.pi, one can compare the simulated relaxation angle across multiple SAFs with varying K_u and thickness (volume), but with unchanging coupling strength. As per Eq. 4.3, K_u and J_1 favour alignment either parallel or antiparallel. The *only source* of non-collinearity is J_2. For a given set of interlayer coupling constants that favour a non-collinear antiparallel state (positive J_1), one expects the introduction of uniaxial anisotropy in *both* layers to pull the magnetic moments apart, widening the interlayer angle, when magnetic energy is completely minimized. Thus, increasing either K_u or the volume of a layer should further increase the angle.

The results of a simulation which tests the direct dependence of angle on K_u (without the effects of demagnetization) in magnum.pi are shown in Fig. 4.3(a, b), while the dependence on layer volume is shown in Fig. 4.3(c, d). Layer radii are 25nm, while the spacer is 0.5nm thick. The relaxation angles provided by numerical minimization of Eq. 4.3 are compared with the results from magnum.pi in Table 4.4, for independently varying the anisotropy in FM2, K_{u2}, (Simulations 1 and 2) and the thickness of FM2, d_2, (Simulations 3 and 4). All simulations demonstrate that the magnum.pi `UniaxialAnisotropyField` class implementation behaves very similarly to the macrospin model without demagnetization, with a maximum deviation of 4.1°.

Table 4.4: Interlayer angle from a macrospin model with uniaxial anisotropies compared with those from magnum.pi for varying K_{u_2} (Simulations 1 and 2) and d_2 (Simulations 3 and 4).

	Simulation 1	Simulation 2	Simulation 3	Simulation 4
K_{u1} (J/m^3)	1.0×10^6	1.0×10^6	1.0×10^6	1.0×10^6
K_{u2} (J/m^3)	0.5×10^5	3.0×10^5	2.0×10^5	2.0×10^5
d_1 (nm)	3.0	3.0	3.0	3.0
d_2 (nm)	3.0	3.0	1.5	6.0
J_1 (J/m^2)	1.5×10^{-3}	1.5×10^{-3}	1.5×10^{-3}	1.5×10^{-3}
J_2 (J/m^2)	1.5×10^{-3}	1.5×10^{-3}	1.5×10^{-3}	1.5×10^{-3}
θ_{min} (Macrospin)	123.8°	162.8°	128.9°	180.0°
θ_{min} (magnum.pi)	124.3°	158.7°	129.6°	179.4°

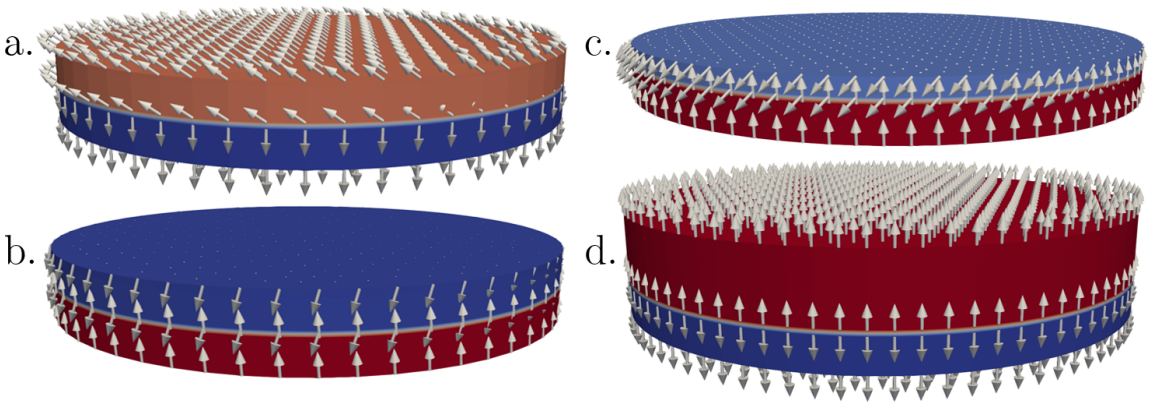

Figure 4.3: (a.) and (b.): validation of the K_u dependence of the anisotropy energy term in magnum.pi, comparing two SAFs with identical dimensions but differing K_u in the upper layer: $K_{u2} = 0.5 \times 10^5$J/m^3 (a.) and $K_{u2} = 3.0 \times 10^5$J/m^3 (b.). K_{u1} is held constant at 1×10^6J/m^3. Both simulations have identical interlayer coupling of $J_1 = J_2 = 1.5 \times 10^{-3}$J/m^2: they differ from Fig. 4.1(b.) only in that both layers now have non-zero anisotropy. Note that (a.) shows only a small increase in angle, to 124°, while the angle in (b.) is much larger: approximately 159°. This dependence on K_u is as expected: the increased anisotropy energy density will pull the energy minima toward the easy axis, widening the relaxation angle with increasing K_u. The layers that appear to deviate farther from the z-axis are those with a smaller anisotropy - the upper layer in both (a.) and (b.). (c.) and (d.): validation of the volume dependence of the anisotropy energy term in magnum.pi, comparing two SAFs with identical K_u but differing thicknesses in the upper layer: $d_2 = 1.5$nm (c.) and $d_2 = 6.0$nm (d.). K_u is held constant at 1×10^6J/m^3 in the bottom layer, with 2×10^5J/m^3 in the top. Both simulations have identical interlayer coupling of $J_1 = J_2 = 1.5 \times 10^{-3}$J/m^2, which would cause a relaxation angle of 120° in the absence of anisotropy. Where the thin and soft upper layer in (c.) develops almost all of the interlayer angle (129°), (d.) relaxes to 179°, nearly collinear. This dependence on volume is as expected: the increased total anisotropy energy will pull the energy minima toward the easy axis, widening the relaxation angle with increasing volume.

Stray field

Each magnetic layer in a structure generates an internal and an external magnetic field. The external field (the stray field) can act on other layers, in much the same way as the Zeeman effect: the magnetic moment of a layer will prefer to align with the local stray field. This can have deleterious effects on the consistency of writing to an MRAM bit [10]. Owing to the shape of the magnetic field emitted by a magnetic dipole, the stray field emitted by an in-plane sample will prefer an antiparallel state, while an out-of-plane sample will prefer a parallel state.

To test for this behaviour in magnum.pi, I relaxed a range of SAFs from a random initial state without interlayer coupling, but with demagnetization ($M_s = 900 \times 10^3 \mathrm{A/m}$) and a varying anisotropy. Layer radii are uniformly 20nm, magnetic layers have 3nm thickness, while the spacer is 0.5nm thick. For small anisotropies, one expects the layers to relax to an antiparallel *in-plane* state, while for large anisotropies, one expects the layers the anisotropy energy density to exceed that of the stray field and the layers to relax to a parallel *out-of-plane* state. The results of this simulation are shown in Fig. 4.4, which shows the transition from antiparallel in-plane to parallel out-of-plane occurring at $K_u = 3.65 \times 10^5 \mathrm{J/m^3}$.

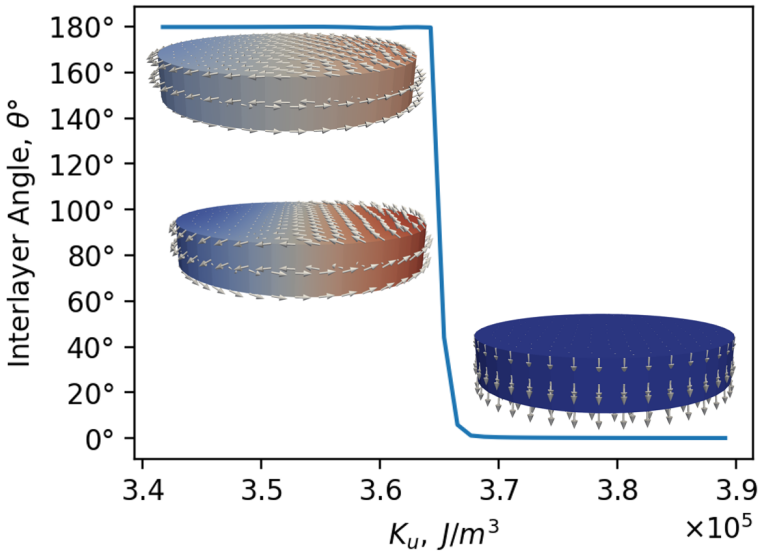

Figure 4.4: Test of the effect of stray field on two non-coupled magnetic layers. For low values of K_u, the stray and internal demagnetization fields dominate: the layers relax to an in-plane, antiparallel configuration. For large values of K_u, the anisotropy dominates: the layers relax to an out-of-plane, parallel configuration. Critically, this result is consistent with that of two simple magnetic dipoles arranged beside each other and on top of one another - the magnetic field lines favour either an antiparallel or parallel configuration, respectively.

Demagnetization field

The internal demagnetization energy in a thin sample is minimized when it is magnetized in-plane and maximized when out-of-plane. If we approximate our sample to be a uniformly magnetized, 20nm radius, 3nm thick, oblate spheroid, we can calculate the contribution of demagnetization (K_s) to the total anisotropy by [53], as follows:

$$\begin{aligned} K_s &= N\frac{\mu_0}{2}M_s^2 = (N_z - N_x - N_y)\frac{\mu_0}{2}M_s^2, \\ N_z &= \frac{m^2}{m^2-1}\left[1 - \frac{1}{\sqrt{m^2-1}}\arcsin\left(\frac{\sqrt{m^2-1}}{m}\right)\right], \quad m = \frac{r}{d/2}, \\ N_x &= N_y = \frac{1-N_z}{2}, \end{aligned} \tag{4.4}$$

which gives $K_s = 3.995 \times 10^5 \mathrm{J/m^3}$ for $M_s = 900 \times 10^3 \mathrm{A/m}$. This result can be compared with a simple magnum.pi simulation of a single ferromagnetic layer relaxed from a random state, with demagnetization and a varying K_u. One expects that the sample will relax to an in-plane state where $K_u < K_s$ and an out-of-plane state when $K_u > K_s$. The results of this simulation are shown in Fig. 4.5, which indicates that the sample relaxes to within a tenth of a degree of perfectly out-of-plane at approximately $K_u = K_s = 3.953 \times 10^5 \mathrm{J/m^3}$. While this value agrees well with the approach above, the distinction is important: the non-collinear region between $\sim 3.71 \times 10^5 \mathrm{J/m^3}$ and $3.88 \times 10^5 \mathrm{J/m^3}$ in Fig 4.5(b.) indicates that these structures relaxed to a non-uniform state. This value of K_s is a critical design constraint: all samples with $M_s = 900 \times 10^3 \mathrm{A/m}$, $r = 20\mathrm{nm}$ radius, $d = 3\mathrm{nm}$ must have anisotropies larger than $3.995 \times 10^5 \mathrm{J/m^3}$ in order to relax out-of-plane. Note that the introduction of bilinear coupling in a SAF will introduce an additional compensatory factor, lowering the required value of K_u somewhat.

4.1.2 SAF interlayer coupling angle

J_1 vs J_2 for various values of K_{u_1} and K_{u_2}

Existing fabrication and measurement capabilities of the PNMD lab are limited to thin films, many orders of magnitude larger in area than the nanopillars required by STT-MRAM. Such a change in aspect ratio and size affects most of the discussed magnetic effects, especially demagnetization: to my knowledge, the range of possible FM1/FM2 coupling angles as a function of J_1 and J_2 in nanopillars was previously unknown. This necessitates a comprehensive exploration of the parameter space, varying J_1, J_2, individual layer anisotropies (K_{u_1} and K_{u_2}), and relaxation conditions.

The following simulations all have the same physical structure and mesh: $r_{1/2} = 20\mathrm{nm}$, $d_{1/2} = 3.0\mathrm{nm}$, and a mesh length of $ml = 3\mathrm{nm}$ (in accordance with a minimum exchange length of $\delta_{Ex} = 3.61\mathrm{nm}$). All spacers have $r_s = 20\mathrm{nm}$ and $d_s = 0.5\mathrm{nm}$. Note: the mesh length is deliberately equal to d, making this an "ordered mesh", which vastly decreases simulation

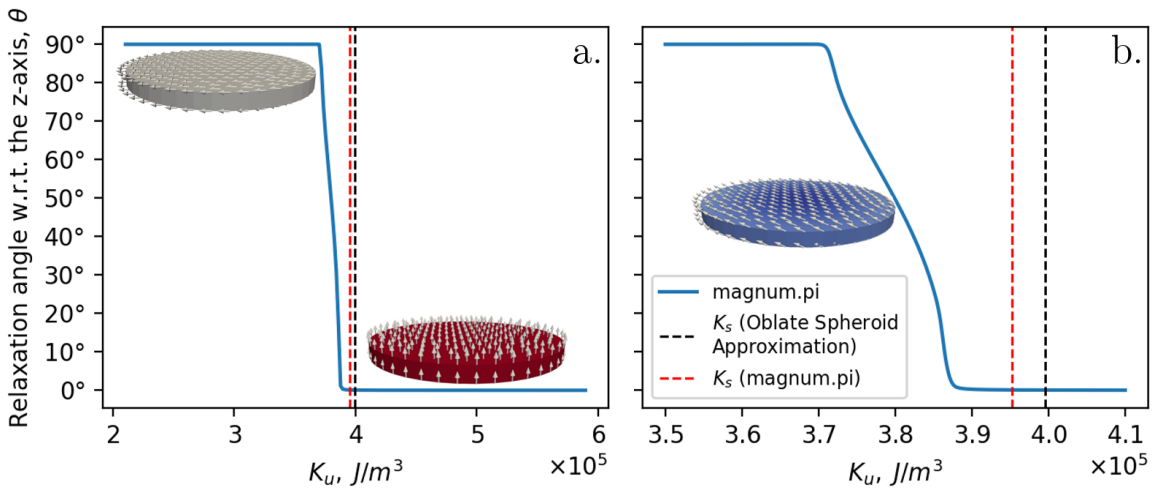

Figure 4.5: Effect of demagnetization on relaxation as a function of the anisotropy in a single layer, plotted as the angle of magnetization of the relaxed spins with respect to the sample surface normal (the z-axis), for a large range of K_u(a.) and an expanded view of the transitional non-uniform region (b.). The sample switches from in-plane to out-of-plane where the strength of the uniaxial anisotropy, K_u, outweighs that of the demagnetization shape anisotropy, K_s, which occurs at approximately $3.81 \times 10^5 \mathrm{J/m^3}$. As per Eq. 2.10, demagnetization energy is largest when $\cos^2(\theta) = 1$, i.e. when the sample is magnetized out-of-plane: $\theta = 0$. Overlaid is the value of K_s give by an approximation of these results for an oblate spheroid, rather than a disk.

time for minimal loss of accuracy. This is justified, as non-homogeneity in the magnetization in the z-axis of these structures is unlikely. Unless otherwise stated, $A_{ex} = 1.3 \times 10^{-11} \mathrm{J/m}$ and $\alpha = 1$, minimizing precessional motion to speed up the simulation without impacting accuracy. The anisotropy axis is always (0, 0, 1) (the z-axis) and $M_s = 900 \times 10^3 \mathrm{A/m}$, which is an average of the current measured values for FM1 and FM2. J_1 and J_2 are varied from $0\,\mathrm{J/m^2}$ to $5.00 \times 10^{-3}\,\mathrm{J/m^2}$ and $0\,\mathrm{J/m^2}$ to $4.00 \times 10^{-3}\,\mathrm{J/m^2}$, respectively, which is a larger range than is currently considered reasonably achievable in samples that have been annealed [54], but provides additional context for future experimental work. Values of K_{u_1} and K_{u_2} ($5.0 \times 10^5 \mathrm{J/m^3}$, $7.5 \times 10^5 \mathrm{J/m^3}$, $1.0 \times 10^6 \mathrm{J/m^3}$) were chosen to include very low values (approaching the strength of demagnetization) and very high (likely to saturate any non-collinear angle). All simulations were relaxed for 100ns, with scalar sampling every 1×10^{-11}s and field sampling every 1×10^{-8}s. Each simulation produces 3600 relaxations, one for each pair of J_1 and J_2. This totals 11GB of data per figure. The magnum.pi script for this simulation is given in Appendix C.1.

For each pair of values of K_{u_1} and K_{u_2}, the simulation is first run with a parallel (PP) initial condition, i.e. the magnetizations of both layers uniformly in the +z-direction, and then with an antiparallel (AP) initial condition, i.e. with the magnetization of FM1 uniformly in -z and FM2 in +z. It should be noted that the PP configuration is most representative of what is reproducible in laboratory conditions: samples relax from saturation in one direc-

tion from an external field. It is difficult to reproduce an AP relaxation in physical samples, but the simulated results provide context for the energy landscape of the structures. All PP relaxations were run with $A_{ex} = 1.3 \times 10^{-10}$J/m to avoid metastable non-homogeneous magnetization configurations. Represented as a phase plot of relaxed interlayer angle, these data provide a "cookbook" for later experimental work, allowing a researcher to reliably choose a given coupling angle for a pair of J_1 and J_2, which are in turn determined by appropriate choices of sputtered materials. As well, these results emphasise the importance of particular values and relative magnitudes of K_u in FM1 and FM2.

Fig. 4.6 shows a phase plot of J_1 vs J_2, for $K_{u_1} = 5.0 \times 10^5$J/m^3, $K_{u_2} = 5.0 \times 10^5$J/m^3 and a PP initial condition. The plot shows four distinct regions, where:

1. the layers relax to an approximately parallel state (i.e. the z-component of both layers has the same sign) with an interlayer separation angle of $< 90°$ (coloured light grey),
2. the layers relax to an approximately parallel state with an interlayer separation angle of $> 90°$ (coloured according to the separation angle),
3. the layers relax to an approximately antiparallel state with a separation angle of $> 90°$ and $< 179°$ (coloured according to the separation angle),
4. the layers relax to an approximately antiparallel state with a separation angle of $> 179°$ (coloured dark grey).

The division between the parallel and antiparallel relaxed states is demarcated by a green contour. For use in the FM1 and FM2 of a non-collinear STT-MRAM structure, all values of J_1 and J_2 that produce approximately parallel or perfectly antiparallel layers are to be ignored: parallel layers produce a strong stray field on FM3 and collinear antiparallel states do not benefit from biquadratic coupling. The regions of interest in this and following plots occur where the creation of antiparallel layers with separation angles between 140° and 150° is possible for J_1 and J_2 less than 2.0×10^{-3}J/m^2, 1.4×10^{-3}J/m^2, respectively, as these are approximately the maximum attainable values in annealed samples [24].

Fig. 4.7 shows a phase plot of J_1 vs J_2, for $K_{u_1} = 5.0 \times 10^5$J/m^3, $K_{u_2} = 5.0 \times 10^5$J/m^3, and an AP initial condition. The difference between Fig. 4.7 and Fig. 4.6 is marked: non-collinear antiparallel structures now appear at much lower values of J_1 and J_2. Where structures relax into two different configurations depending entirely on initial conditions, this is indicative of the presence of a local and a global minimum in the energy landscape. The red portion of the inset in Fig. 4.7 indicates where the relaxing structures fall into different minima between the PP and AP initial conditions. The magnitude of the energy barrier between the two relaxation states for this region is unclear, as is which state is truly the global minimum; this will be explored in later work through a string method approach to barrier estimation [55]. The presence of local minima at certain values of J_1 and J_2 is important—depending on barrier height, states may be "kicked" into undesirable configurations with sufficient thermal energy.

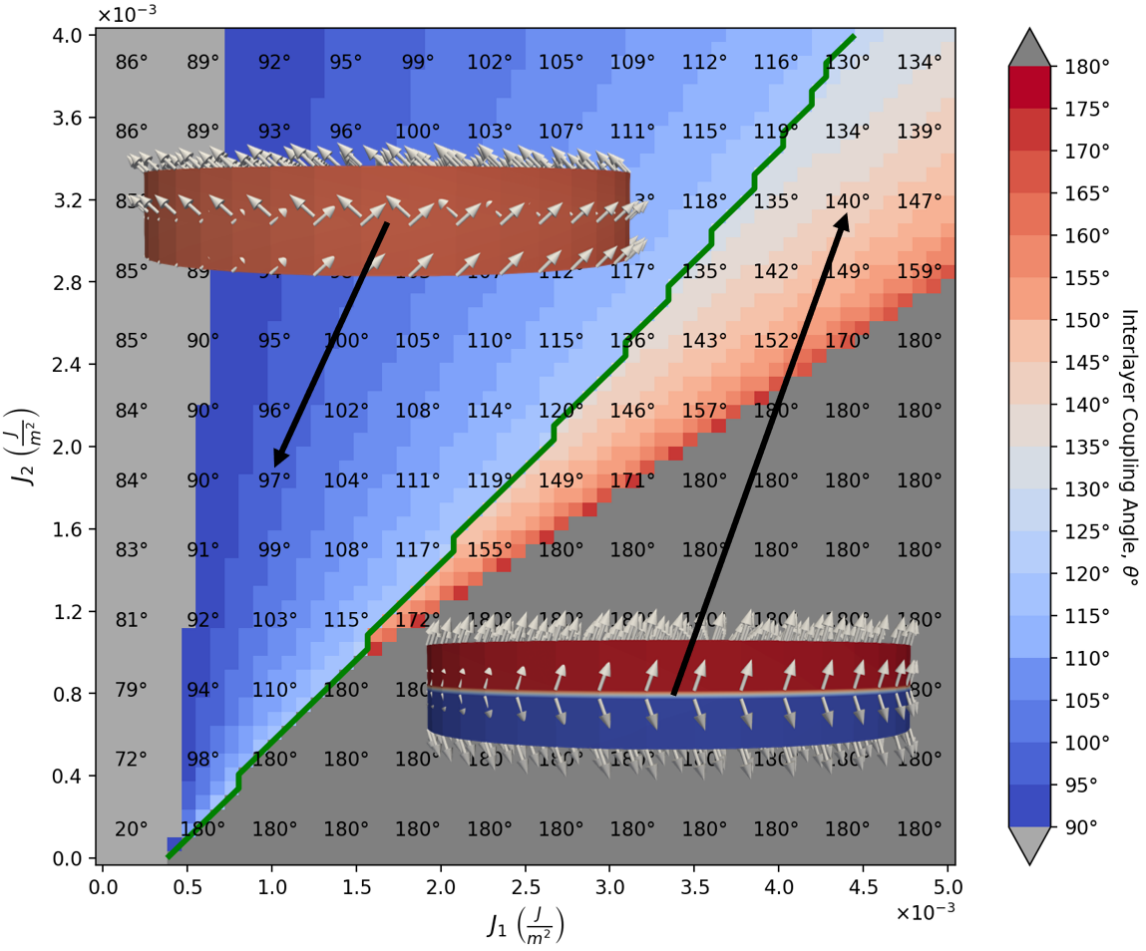

Figure 4.6: SAF interlayer angle phase plot for a 20nm radius FM1 and FM2, plotted as J_1 vs J_2. $K_{u_1} = 5.0 \times 10^5 \mathrm{J/m^3}$, $K_{u_2} = 5.0 \times 10^5 \mathrm{J/m^3}$, with parallel initial conditions. Interlayer angles below 90° are coloured light grey, while interlayer angles above 179° are coloured dark grey. Explanatory insets provide examples of the two relaxation minima: structures to the left of the green contour relaxed to an approximately parallel configuration, with the z-component of magnetization in both layers having the same sign, while structures to the right relaxed to an approximately antiparallel configuration, with the z-component of magnetization in each layer having the opposite sign. Values of J_1 and J_2 for which the structure relaxed to an antiparallel, non-collinear arrangement are of interest for use in STT-MRAM. See Appendix D.1 for this image without insets.

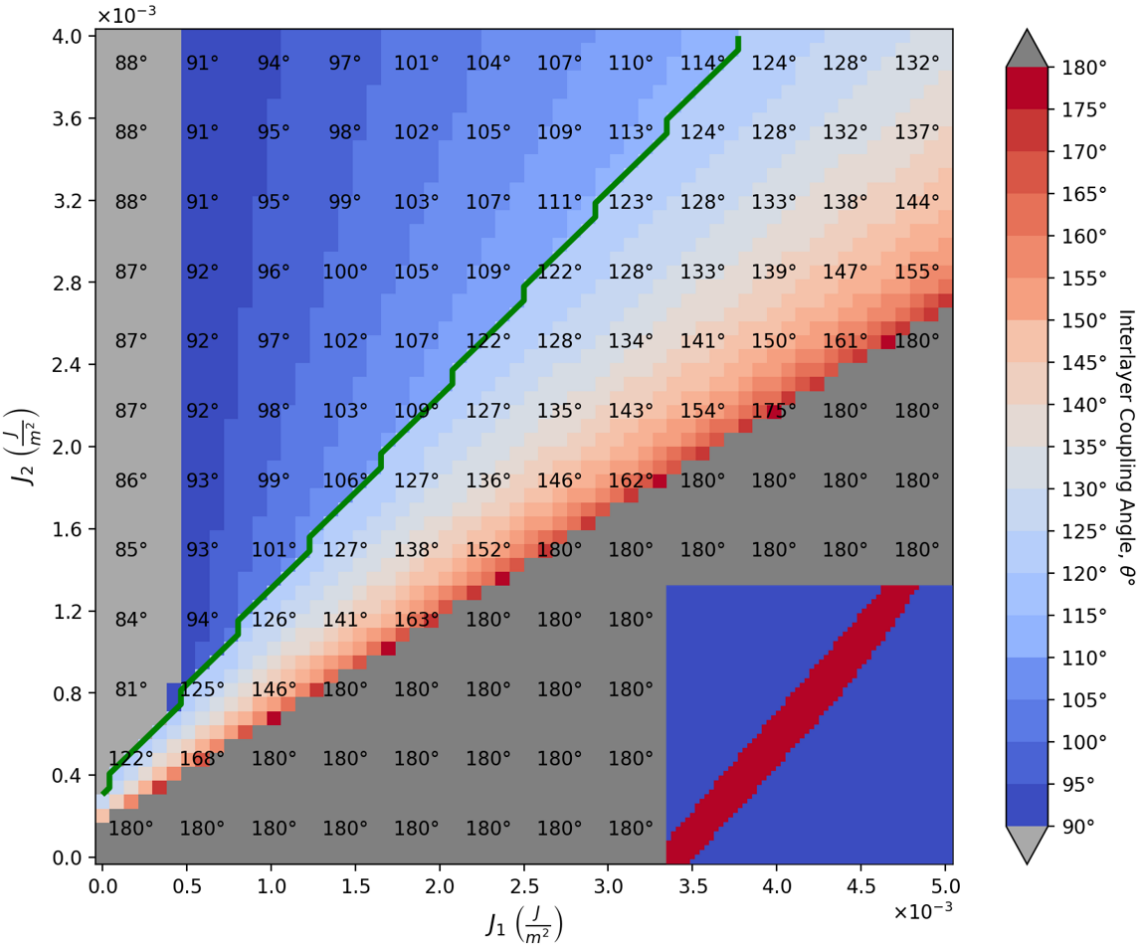

Figure 4.7: SAF interlayer angle phase plot for a 20nm radius FM1 and FM2, plotted as J_1 vs J_2. $K_{u_1} = 5.0 \times 10^5 \mathrm{J/m^3}$, $K_{u_2} = 5.0 \times 10^5 \mathrm{J/m^3}$, with antiparallel initial conditions. The interpretation of the colouring and the green contour is as indicated for Fig. 4.6. On the bottom right, an inset compares the regions of antiparallel and parallel relaxed states in this and Fig. D.1, where red indicates that the structures are in different minima.

Fig. 4.8 shows a phase plot of J_1 vs J_2, for $K_{u_1} = 7.5{\times}10^5\text{J/m}^3$, $K_{u_2} = 7.5{\times}10^5\text{J/m}^3$ and a PP initial condition. While Fig. 4.6 displays few AP non-collinear states for reasonable J_1 and J_2, Fig. 4.8 shows a substantially decreased region of acceptable states, for even larger values of J_1 and J_2. This is in stark contrast with Fig. 4.9, which shows a massive region of AP non-collinear states. However, as before, this difference only indicates the presence of a (potentially problematic) local minimum. Similar results for $K_{u_1} = 1.0 \times 10^6\text{J/m}^3$, $K_{u_2} = 1.0 \times 10^6\text{J/m}^3$ are included in Appendix D.1.

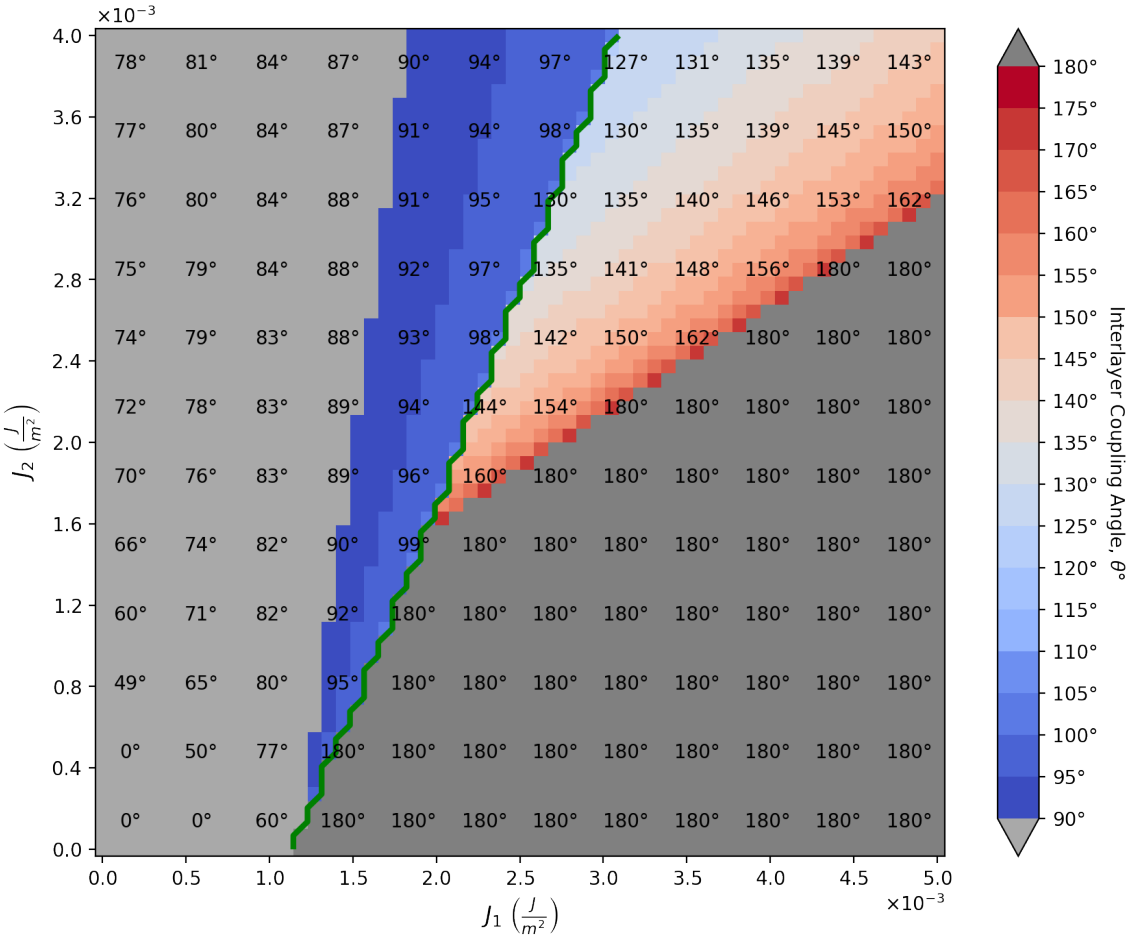

Figure 4.8: SAF interlayer angle phase plot for a 20nm radius FM1 and FM2, plotted as J_1 vs J_2. $K_{u_1} = 7.5 \times 10^5\text{J/m}^3$, $K_{u_2} = 7.5 \times 10^5\text{J/m}^3$, with parallel initial conditions. The interpretation of the colouring and the green contour is as indicated for Fig. 4.6.

Fig 4.10 is a departure from those previously in that $K_{u_1} \neq K_{u_2}$. Here, we see substantial broadening of the AP non-collinear region: stable structures are possible for as low as $J_1 = 0.51 \times 10^{-3}\text{J/m}^2$ and $J_2 = 0.54 \times 10^{-3}\text{J/m}^2$, which creates 147°. Likewise, the AP relaxation in Fig. 4.11 indicates that there is only one energy minimum for all of the region of interest.

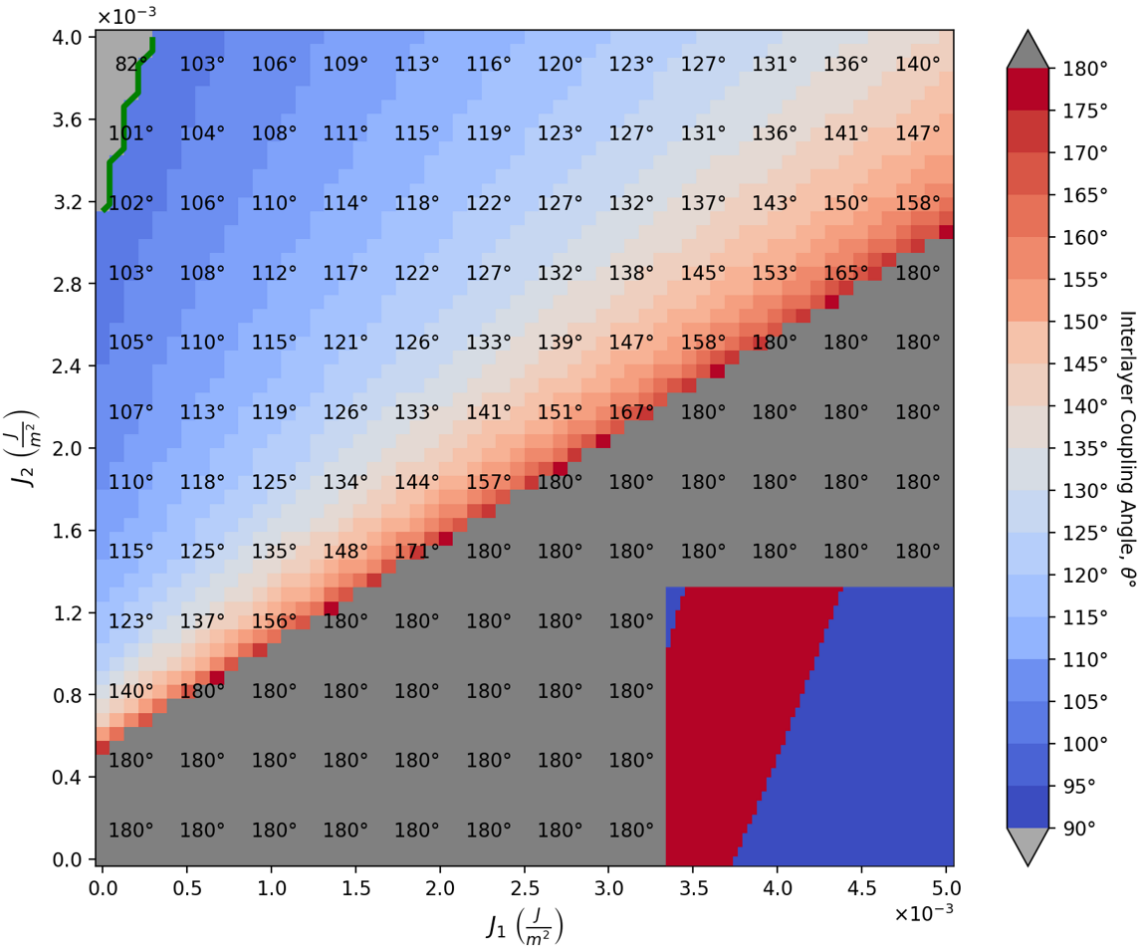

Figure 4.9: SAF interlayer angle phase plot for a 20nm radius FM1 and FM2, plotted as J_1 vs J_2. $K_{u_1} = 7.5 \times 10^5 \mathrm{J/m^3}$, $K_{u_2} = 7.5 \times 10^5 \mathrm{J/m^3}$, with antiparallel initial conditions. The interpretation of the colouring and the green contour is as indicated for Fig. 4.6.

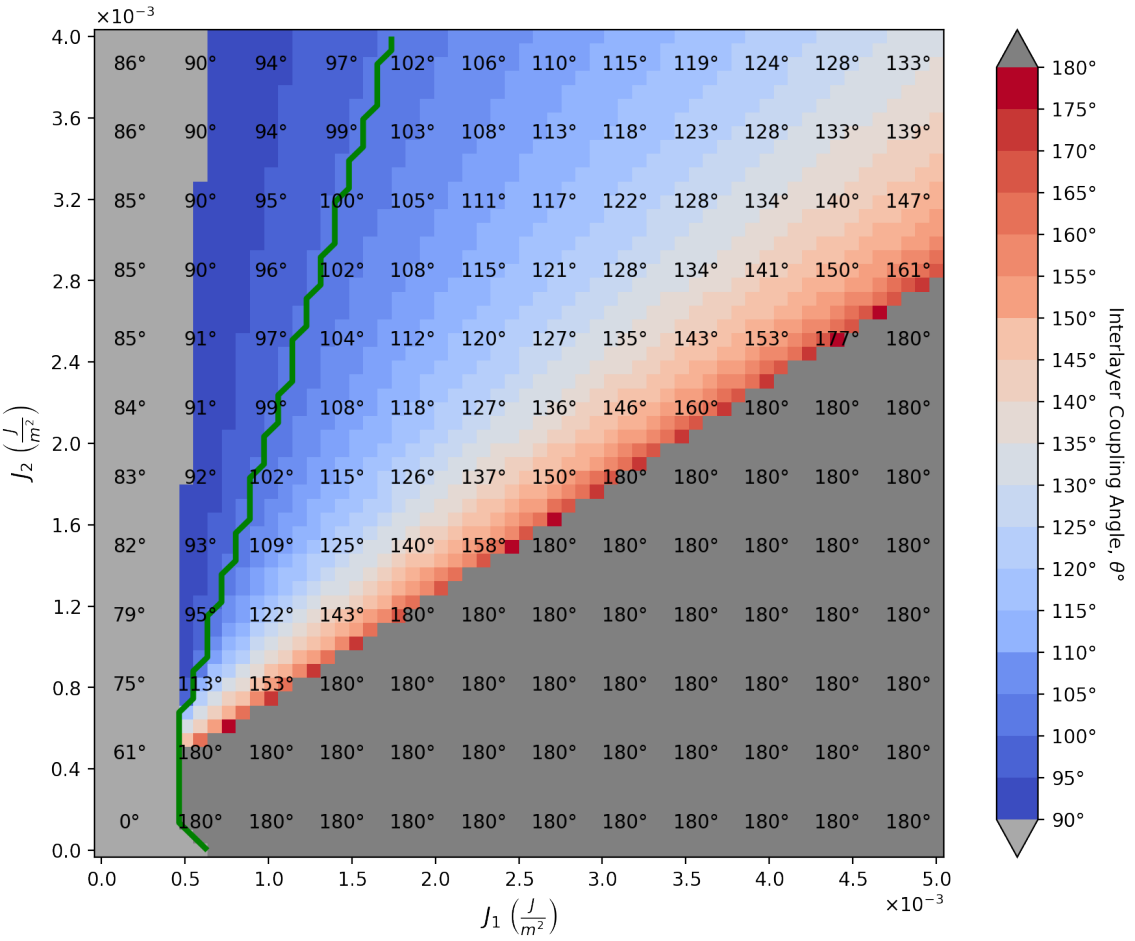

Figure 4.10: SAF interlayer angle phase plot for a 20nm radius FM1 and FM2, plotted as J_1 vs J_2. $K_{u_1} = 7.5 \times 10^5 \mathrm{J/m^3}$, $K_{u_2} = 5.0 \times 10^5 \mathrm{J/m^3}$, with parallel initial conditions. The interpretation of the colouring and the green contour is as indicated for Fig. 4.6.

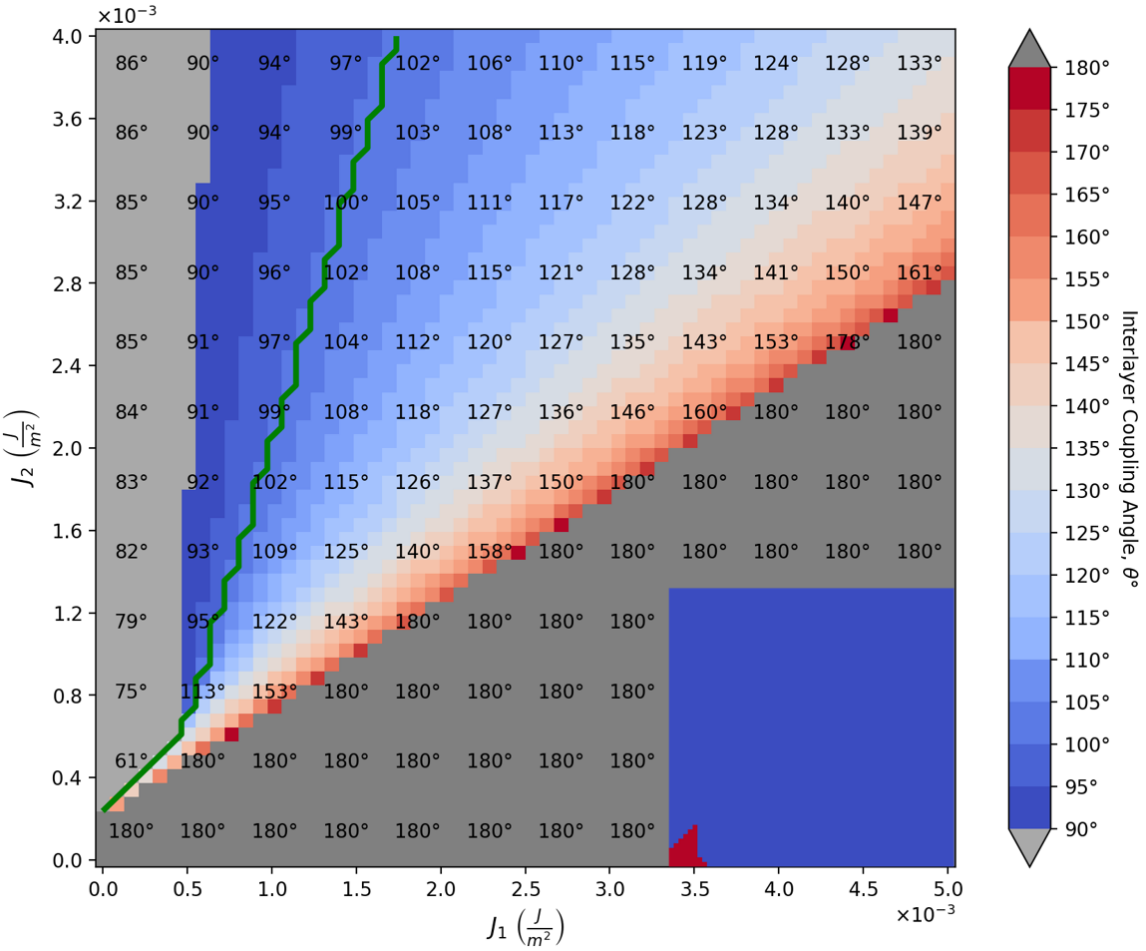

Figure 4.11: SAF interlayer angle phase plot for a 20nm radius FM1 and FM2, plotted as J_1 vs J_2. $K_{u_1} = 7.5 \times 10^5 \mathrm{J/m^3}$, $K_{u_2} = 5.0 \times 10^5 \mathrm{J/m^3}$, with antiparallel initial conditions. The interpretation of the colouring and the green contour is as indicated for Fig. 4.6. On the bottom right, an inset compares the regions of antiparallel and parallel relaxed states in this and Fig. 4.10, where red indicates that the structures are in different minima.

Further increasing the disparity in K_u between the layers leads to an even larger AP non-collinear region, as shown in Fig. 4.12, with smallest allowable values of $J_1 = 0.42{\times}10^{-3}\text{J/m}^2$ and $J_2 = 0.48 \times 10^{-3}\text{J/m}^2$, creating 152°. Again, the AP relaxation in Fig. 4.13 indicates that local minima only exist where the structure relaxes into either parallel or collinear configurations. As this result is especially promising, a third simulation focusing only on the easily attainable values of J_1 and J_2 in annealed samples [54] is provided in Appendix D.1.

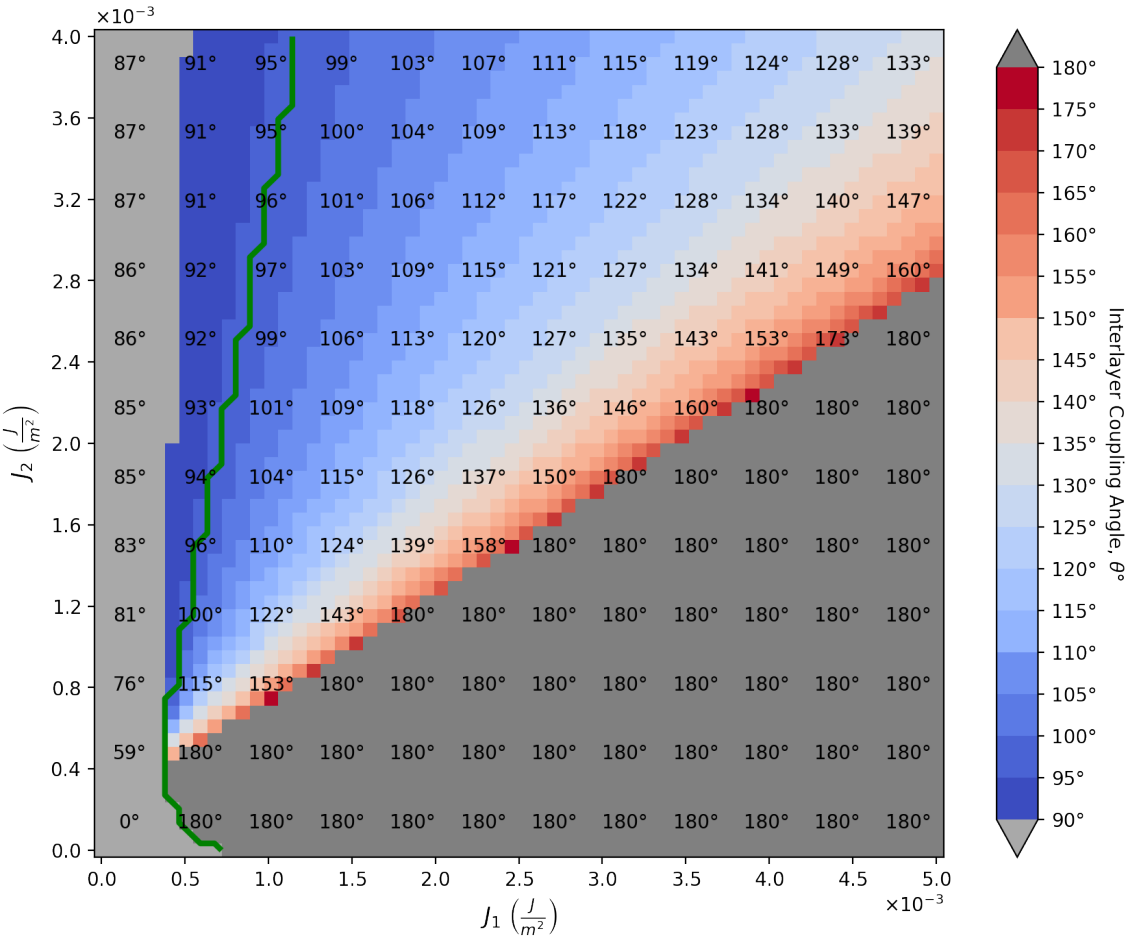

Figure 4.12: SAF interlayer angle phase plot for a 20nm radius FM1 and FM2, plotted as J_1 vs J_2. $K_{u_1} = 1.0 \times 10^6\text{J/m}^3$, $K_{u_2} = 5.0 \times 10^5\text{J/m}^3$, with parallel initial conditions. The interpretation of the colouring and the green contour is as indicated for Fig. 4.6. See Appendix D.1 for this simulation limited to ranges of J_1 and J_2 that are currently considered reasonable to reproduce.

Finally, Fig. 4.14 shows that an increase of K_{u_2} leads to a *decrease* of attainable values of J_1 and J_2 that produce desirable relaxations and a broadening of the region where the relaxations get caught in a local minimum (shown in Fig. 4.15). As well, we see a complete disappearance of the PP region with angles $> 90°$ in both the AP and PP relaxations.

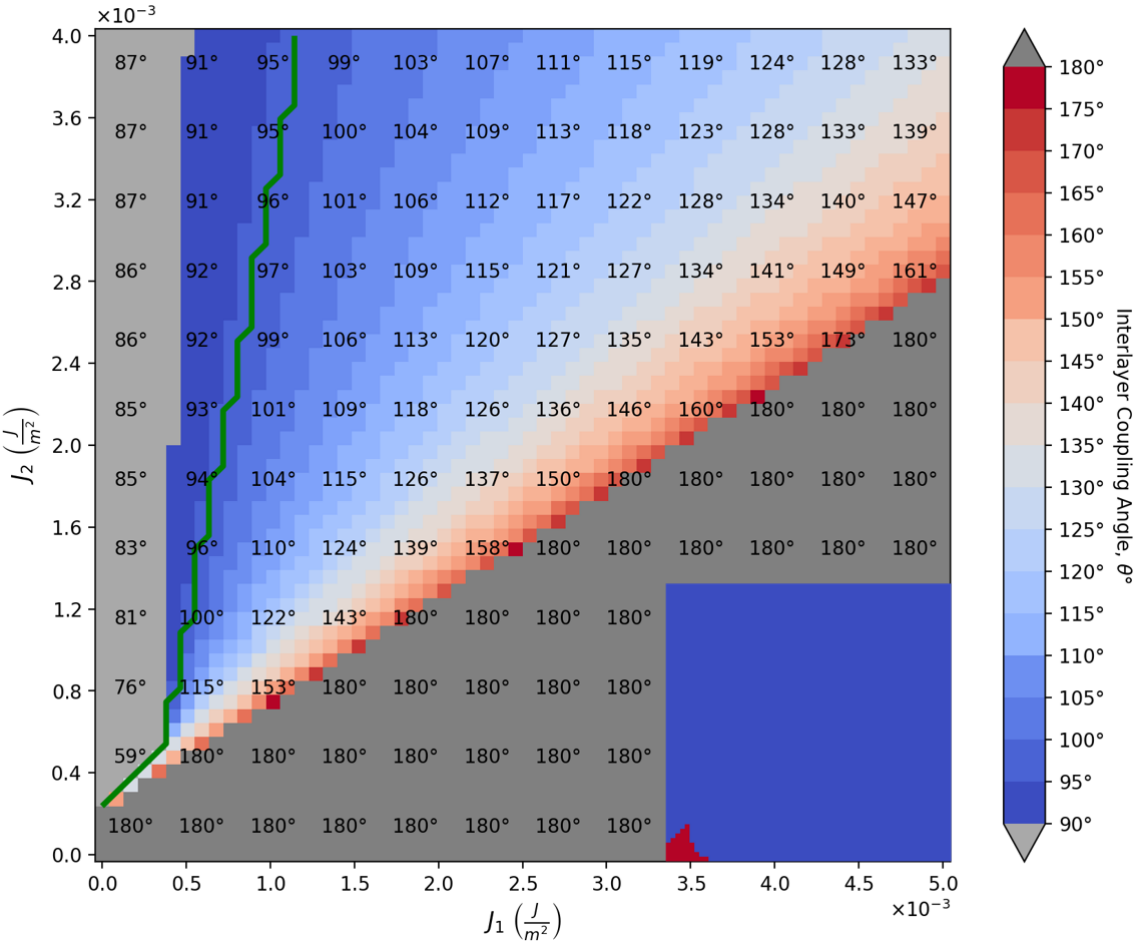

Figure 4.13: SAF interlayer angle phase plot for a 20nm radius FM1 and FM2, plotted as J_1 vs J_2. $K_{u_1} = 1.0 \times 10^6 \mathrm{J/m^3}$, $K_{u_2} = 5.0 \times 10^5 \mathrm{J/m^3}$, with antiparallel initial conditions. The interpretation of the colouring and the green contour is as indicated for Fig. 4.6. On the bottom right, an inset compares the regions of antiparallel and parallel relaxed states in this and Fig. 4.12, where red indicates that the structures are in different minima.

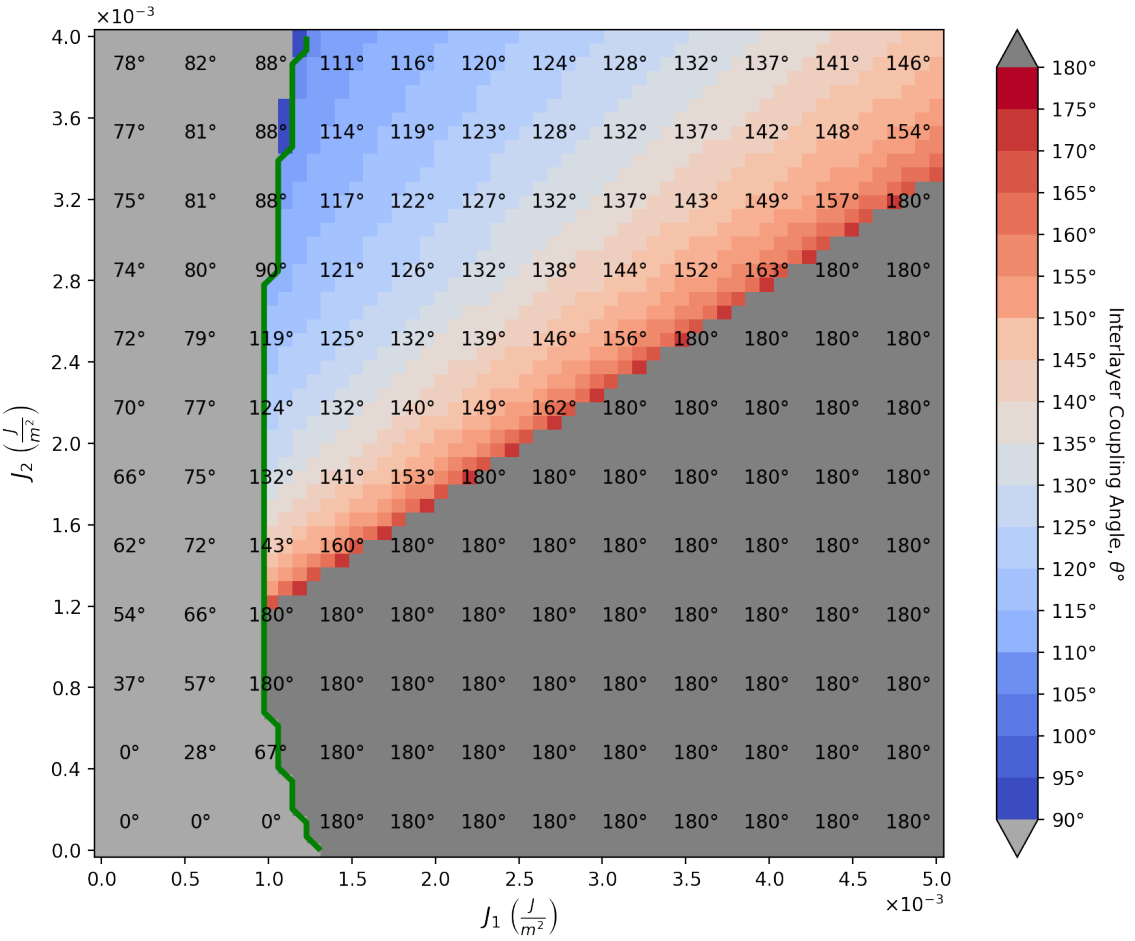

Figure 4.14: SAF interlayer angle phase plot for a 20nm radius FM1 and FM2, plotted as J_1 vs J_2. $K_{u_1} = 1.0 \times 10^6 \mathrm{J/m^3}$, $K_{u_2} = 7.5 \times 10^5 \mathrm{J/m^3}$, with parallel initial conditions. The interpretation of the colouring and the green contour is as indicated for Fig. 4.6.

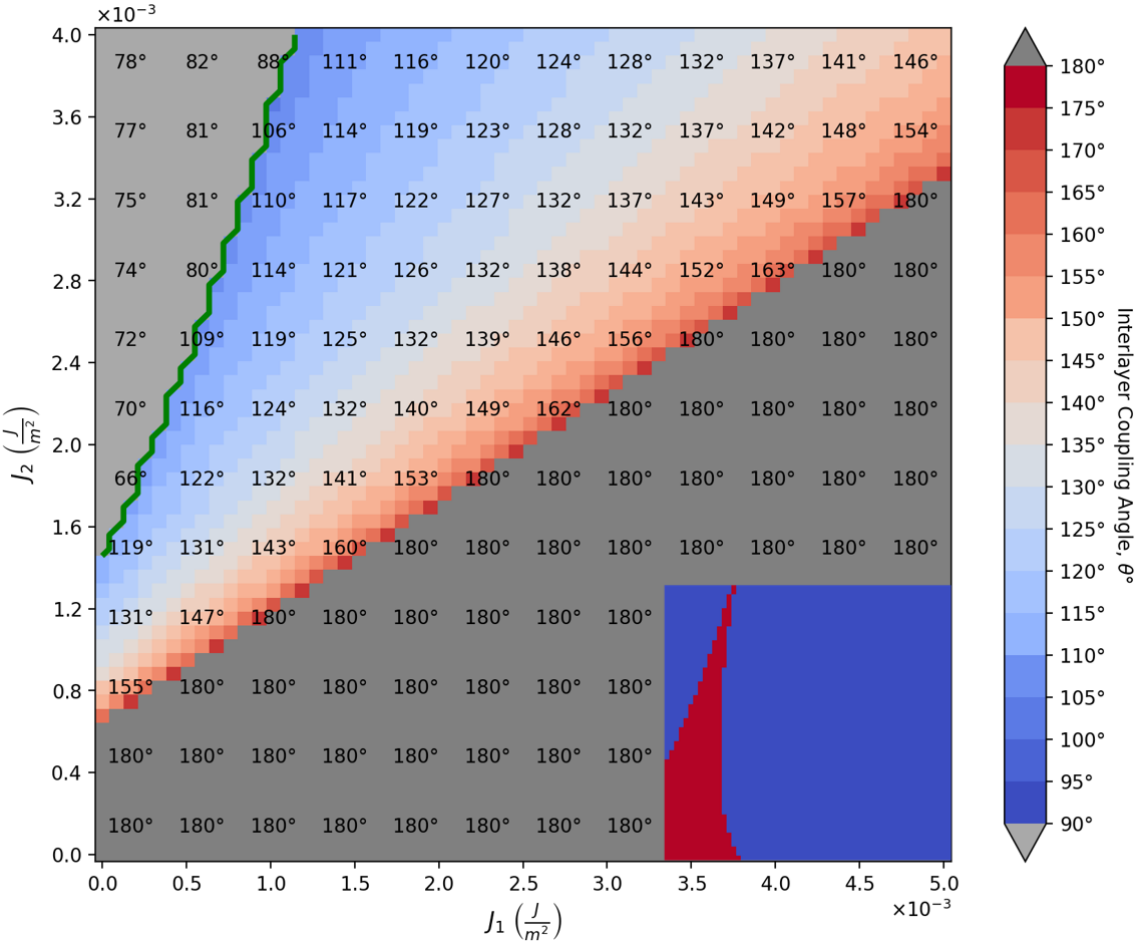

Figure 4.15: SAF interlayer angle phase plot for a 20nm radius FM1 and FM2, plotted as J_1 vs J_2. $K_{u_1} = 1.0 \times 10^6 \mathrm{J/m^3}$, $K_{u_2} = 7.5 \times 10^5 \mathrm{J/m^3}$, with antiparallel initial conditions. The interpretation of the colouring and the green contour is as indicated for Fig. 4.6. On the bottom right, an inset compares the regions of antiparallel and parallel relaxed states in this and Fig. 4.14, where red indicates that the structures are in different minima.

K_{u_1} vs K_{u_2} for a given value of J_1 and J_2

Fig. 4.16 shows what is effectively the inverse of the figures in Section 4.1.2, where, instead of J_1 plotted against J_2 for a given pair of values of K_{u_1} and K_{u_2}, K_{u_1} is plotted against K_{u_2} for a given value of J_1 and J_2: $J_1 = 2.0 \times 10^{-3}\text{J/m}^2$, $J_2 = 1.4 \times 10^{-3}\text{J/m}^2$. This result confirms the previous conclusion: symmetric values of K_{u_1} and K_{u_2} most commonly lead to either parallel or collinear antiparallel configurations, while asymmetric K_{u_1} and K_{u_2} allow for a broad range of controllable non-collinear states. For these values of J_1 and J_2, one layer must have K_u between $5.0 \times 10^5\text{J/m}^3$ and $5.5 \times 10^5\text{J/m}^3$, while the other is free to vary between $5.0 \times 10^5\text{J/m}^3$ and $1.0 \times 10^6\text{J/m}^3$.

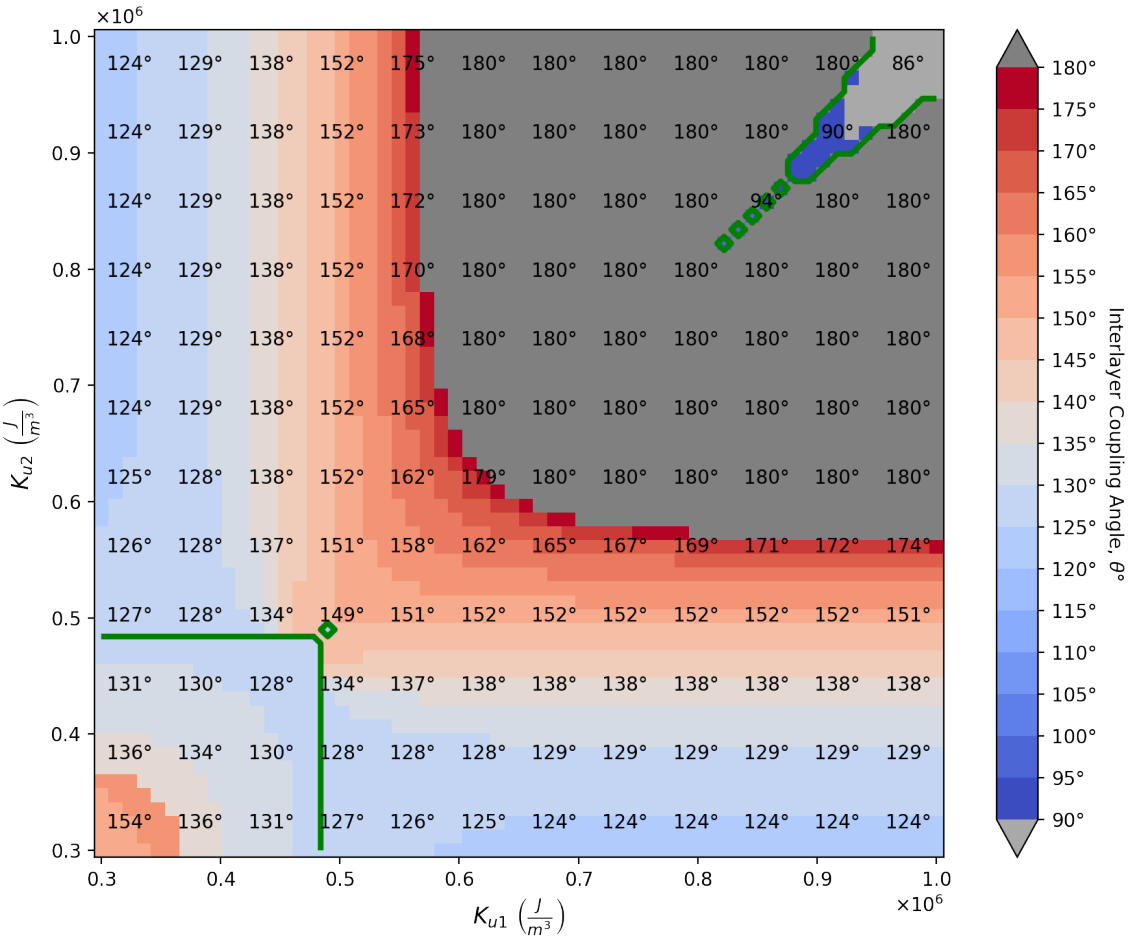

Figure 4.16: SAF interlayer angle phase plot for a 20nm radius FM1 and FM2, plotted as K_{u_1} vs K_{u_2}. $J_1 = 2.0 \times 10^{-3}\text{J/m}^2$, $J_2 = 1.4 \times 10^{-3}\text{J/m}^2$, with parallel initial conditions. The interpretation of the colouring and the green contour is as indicated for Fig. 4.6. The range of values of J_1 and J_2 that produce AP non-collinear states is smallest where $K_{u_1} = K_{u_2}$.

4.2 Dynamic simulations

4.2.1 Field-induced switching coherency

The simple calculations in Section 4.1.1 demonstrate that all relaxed states in the studied structures will be homogeneous. However, it is an open question whether layers with these dimensions and magnetic properties will switch homogeneously or through domain-wall propagation. The maximum coercive field of a single homogeneous layer is often modeled through the Stoner–Wohlfarth model [29], which gives,

$$H_c = \mu_0 H_{mc} - \mu_0 H_d = \mu_0 \frac{2K_{mc}}{\mu_0 M_s} - \mu_0 K_s = \frac{2K_{mc}}{M_s} - (N_z - N_x - N_y)\,\frac{\mu_0^2}{2} M_s^2, \tag{4.5}$$

where H_c is in Tesla and K_s is calculated exactly as in Section 4.1.1 [53]. By this model, one expects H_c to decrease with increasing layer radius as N_z approaches its maximum value of "1" and demagnetization is strengthened. magnum.pi can be compared against the Stoner-Wohlfarth model in a simulation of a single layer of varying radius, subject to a linearly increasing external magnetic field opposite to the direction of magnetization. At a certain field strength, the layer will switch, either coherently or otherwise. It is expected that, where the layers switch coherently (i.e. for small radii), the simulated coercive field should follow the Stoner-Wohlfarth model.

The z-component of magnetization for a field-induced switching process for disks of radii from 5nm to 50nm is shown Fig. 4.17, which covers the range of radii commonly used in out-of-plane STT-MRAM devices [9, 56]. Initially, the magnetization in each layer is aligned 0.5° off the z-axis to produce a non-zero torque from the Zeeman effect at the beginning of the switching process. For each radius, $K_u = 7.0 \times 10^5 \mathrm{J/m^3}$, $M_s = 900 \times 10^3 \mathrm{A/m}$, and $\alpha = 0.1$ to capture the dynamics of the switching process. The external field is varied linearly from 0T to 2.0T over 200ns. The coercive fields of Fig. 4.17 are compared with values calculated by Eq. 4.5 in Fig. 4.18, which shows that magnum.pi consistently underestimates the value of H_c for a given radius, but converges for small radii. This is consistent with the prediction: domain-wall propagation and non-homogeneity in large layers decreases H_c.

If FM3 (the free layer) switches decoherently, i.e. through domain wall-propagation, this will introduce some level of stochasticity in the switching characteristics. One can measure the coherency of a layer in magnum.pi as follows: record the angle with respect to the z-axis of each spin in the mesh and calculate the standard deviation of this ensemble of angles for each timestep of a switching process. Timesteps where the standard deviation is high correspond to stages of a reversal where portions of the layer are magnetized opposite the rest (decoherent), while a low standard deviation corresponds to homogeneous states (coherent). This is shown in Fig. 4.19, which demonstrates that all simulated layers have a non-zero standard deviation of angle during a reversal. However, this method is very sensitive to sampling rate and the size of the field step during the switch—the measurement

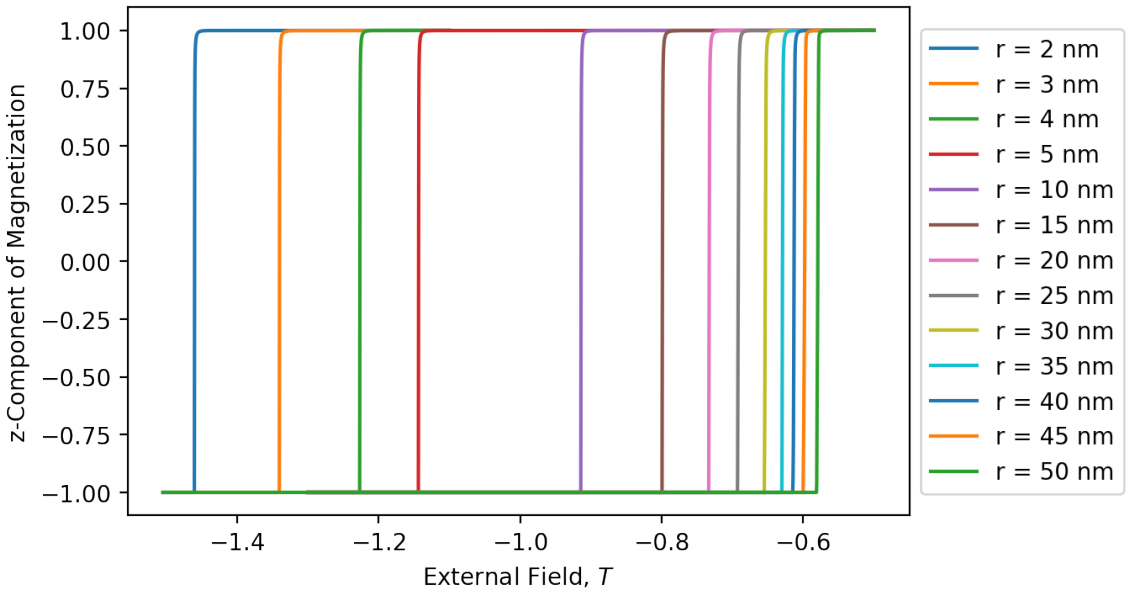

Figure 4.17: Switching characteristics of a single layer with varying radius (r) in an external field, initially magnetized in the positive z-direction. Coercive field (the field at which the layer switches polarity), H_c, increases with decreasing radius.

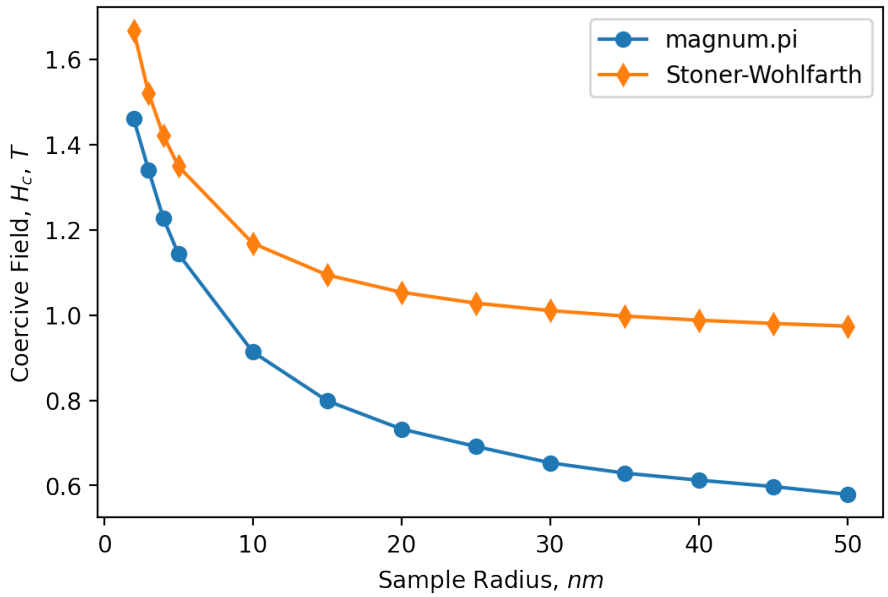

Figure 4.18: H_c for various layer radii as measured in magnum.pi and calculated through the Stoner-Wohlfarth model. magnum.pi consistently underestimated H_c for larger radii, but converges to Stoner-Wohlfarth for small samples. Where the layers switch completely coherently, it is expected that magnum.pi follows Stoner-Wohlfarth.

must capture an event spanning only a few timesteps. As such, this simulation was repeated for layers with radii 10nm to 15nm, which is shown in Fig. 4.20, and only confirms the previous result: all layers with dimensions that satisfy the thermal stability condition (and are magnetized out-of-plane—see Table 4.2) will switch decoherently. Indeed, if FM3 has $r = 10\text{nm}$, $M_s = 7.4\text{A/m}$, $K_u = 4.3 \times 10^5 \text{J/m}^3$, and $d = 3.0\text{nm}$ (similar to existing PNMD FM3 thin-film samples), then $\Delta = 50$, which is thermally unstable.

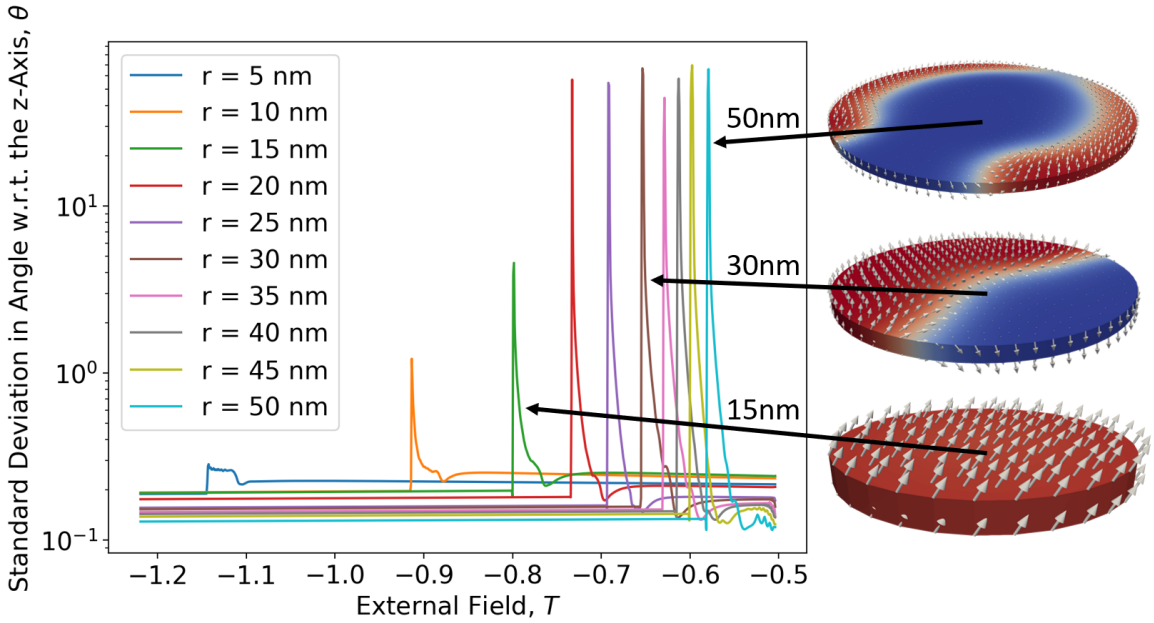

Figure 4.19: Coherency of switching of layers with radii from 5nm to 50nm in an external field. Coherency is measured as the standard deviation of the angle with respect to the z-axis of each spin in the magnum.pi mesh, for each timestep. All layers exhibited *some* decoherency during reversal, though all layers with $r < 20\text{nm}$, have less than $10°$ of standard deviation. Explanatory insets for the instances of maximum decoherency are included for $r = 15\text{nm}$ (bottom), $r = 30\text{nm}$, and $r = 50\text{nm}$ (top).

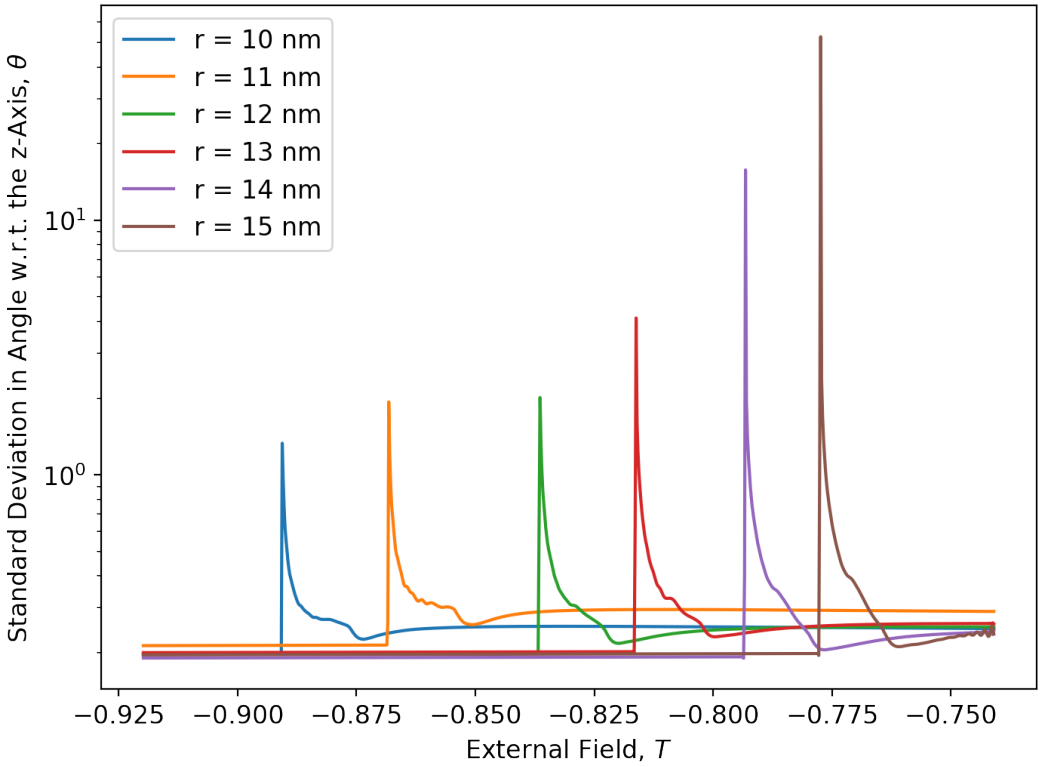

Figure 4.20: Coherency of switching of layers with radii from 10nm to 15nm in an external field. Coherency is measured as the standard deviation of the angle with respect to the z-axis of each spin in the magnum.pi mesh, for each timestep. Even stable layers at the lower end of what is considered easy to fabricate [9, 56], switch decoherently.

4.2.2 Dependence of switching current on FM1/FM2 coupling angle

This section examines a three layer STT-MRAM structure, where FM1 is a fixed coupling layer, FM2 is a fixed reference layer, and FM3 is a free writing layer. Δ in FM1, FM2, and FM3 must be large enough to ensure long-term resilience to thermal fluctuations, but Δ_{FM3} must also always be lower than that of FM2 to maintain write-ability at reasonable current densities [9]. I chose the following material and physical parameters for this analysis: $r = 20\text{nm}$, $d_3 = 2.0\text{nm}$, $K_{u_3} = 4.3 \times 10^5 \text{J/m}^3$, and $M_{s_3} = 740 \times 10^3 \text{A/m}$, which gives a thermal stability in FM3 of $\Delta = 83$. In accordance with the conclusions of Section 4.1.2, I chose $K_{u_1} = 1.0 \times 10^6 \text{J/m}^3$, $K_{u_2} = 5.0 \times 10^5 \text{J/m}^3$, $M_{s_1} = M_{s_2} = 900 \times 10^3 \text{A/m}$, and $d_1 = d_2 = 3.0\text{nm}$ to maximize the range of values of J_1 and J_2 that produce AP non-collinear structures, also giving $\Delta_{FM2} = 91$. The thickness of the second spacer is chosen to be 2.5nm to eliminate any interlayer exchange coupling between FM2 and FM3 [57]. The magnum.pi script for this simulation is given in Appendix C.2.

As described in Section 2.3.2, one can write both MRAM states (where FM2 and FM3 are antiparallel or parallel) by reversing the direction of the writing current. The results of simulating this structure with a linearly increasing current density in the negative z-direction and an initially AP FM2 and FM3 are shown in Fig. 4.21. One can compare this plot against Fig. 4.12 to determine the angles formed by FM1 and FM2 in each regions, though it should be noted that there is a stray field interaction between FM2 and FM3 which will affect the coupling angles. It is clear that the magnitude of the switching current is smallest where FM1 and FM2 are non-collinear, and it is minimized where $\sim 125^\circ < \theta < 179^\circ$. The discontinuities in the switching current landscape are unexpected, one would predict a monotonic increase in current as angle rises above $160^\circ - 170^\circ$. As well, all structures that are collinear switch at random current densities, where FM3 does not switch until a torque is created by the random variation in the magnetic moment caused by the numerical inaccuracy in Python/magnum.pi. This mimics the stochastic switching of STT-MRAM that leverages thermal fluctuations to induce switching. Finally, GMR ratio is maximized when the change in the angle of FM3 with respect to FM2 between states approaches 180°, which occurs as FM1/FM2 coupling angle increases. This necessitates a balance between minimizing switching current through non-collinearity and maximizing the GMR/TMR ratio.

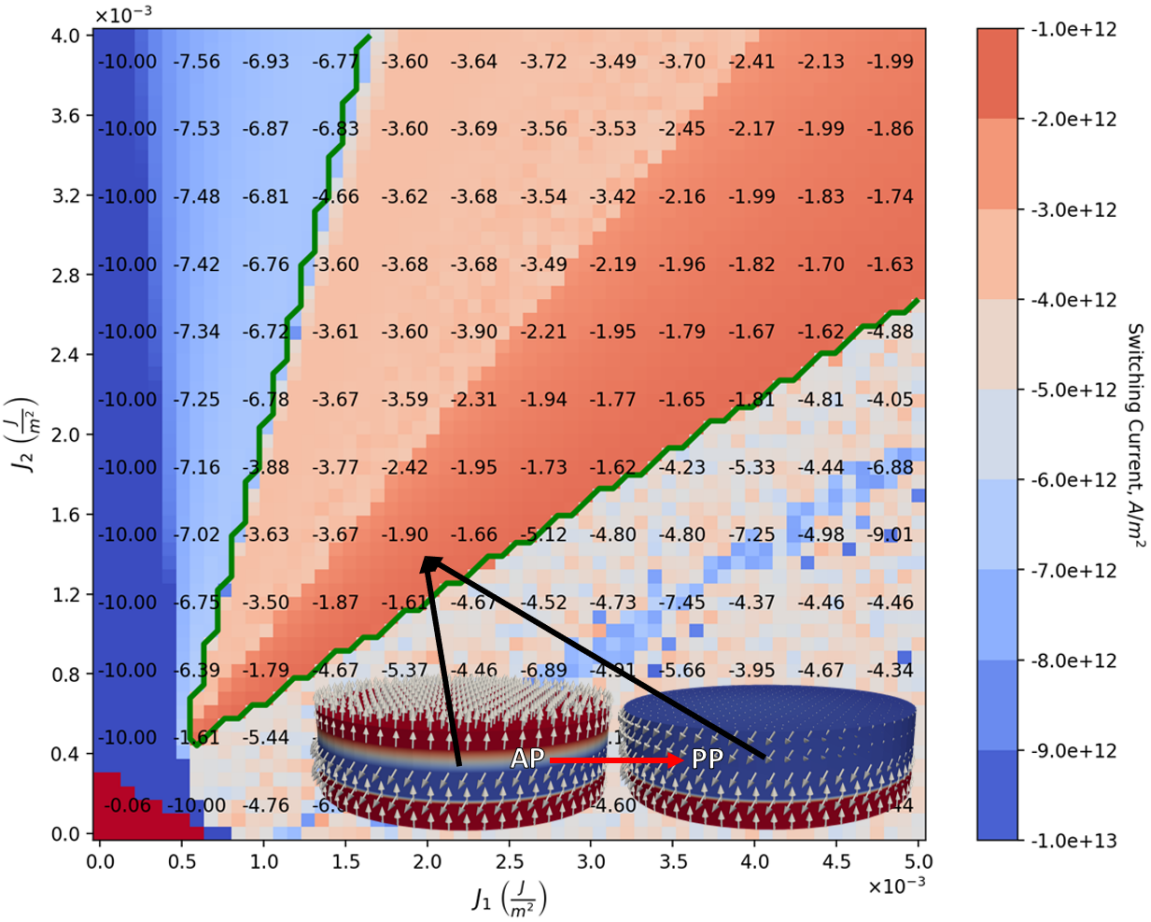

Figure 4.21: Switching current of STT-MRAM initially in an antiparallel state, for varying biquadratic coupling strengths between FM1 and FM2. Structures for which FM1 and FM2 relaxed to an antiparallel state with an interlayer angle $90° < \theta < 179°$ lie between the arms of the green contour. The current is applied in the negative z-direction, which interacts with the moment of FM2, exerting a torque on the comparatively easy FM3 through reflection of minority carriers. The FM3 switching current is minimized for interlayer angles $\sim 125° < \theta < 179°$. Included are two explanatory insets, which correspond to the pre- and post-switch state of the bit for $J_1 = 2.0 \times 10^{-3}\mathrm{J/m^2}$ and $J_2 = 1.4 \times 10^{-3}\mathrm{J/m^2}$. The region below and to the right of the green contour corresponds to perfectly collinear structures, where the switching torque is created by random variation in the magnetic moment caused by the numerical inaccuracy in Python/magnum.pi. The numerical labels within the plot are given in $10^{12}\mathrm{A/m^2}$. This figure is provided without insets in Appendix D.2.

The case where FM2 and FM3 are initially parallel and the current is applied in the positive z-direction is shown in Fig. 4.22. Again, the magnitude of the switching current is smallest where FM1 and FM2 are non-collinear and is minimized where $\sim 122^\circ < \theta < 179^\circ$.

Both Fig. 4.21 and Fig. 4.22 are produced using a simulation that relaxes all three FM layers using the LLG, but only solves the LLG and the STT term in FM3 when applying a current. This is a significant simplification of the magnetization dynamics of the system, as FM2 is prevented from evolving through the torque applied by reflected carriers, which are indeed what causes reversal of FM3 when initially PP. As well, the varying stray field on FM2 from FM3 does not change as FM3 flips. Though this is non-physical, this is considered valid [33]; these results are only intended to demonstrate the relative effect that certain choices of anisotropy in FM1 and FM2 create a large range of minimized switching currents for small J_1 and J_2, rather than obtain an accurate numerical value of the switching current density. Such a restriction in the LLG may explain the discontinuities in the switching current landscape and why the simulations did not show a marked difference in the switching currents for non-collinear AP and PP initial conditions.

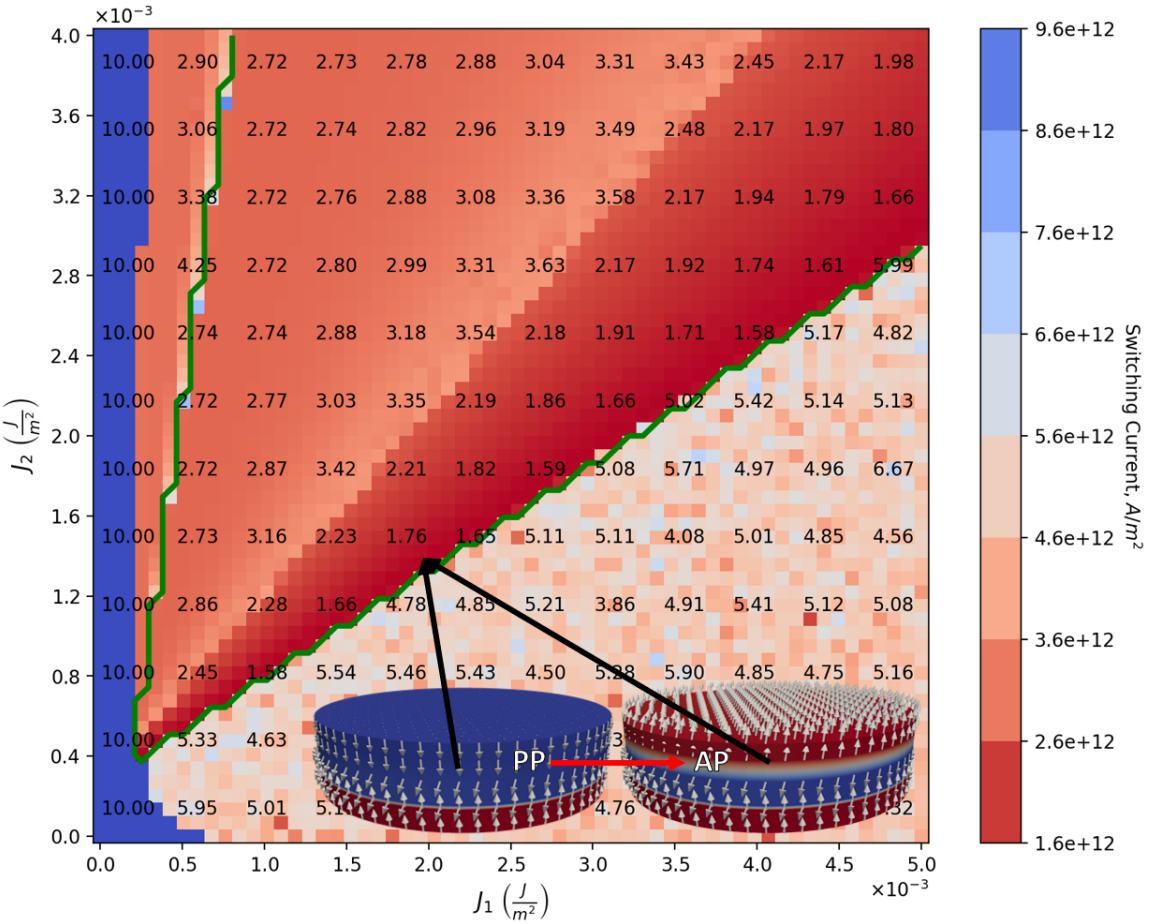

Figure 4.22: Switching current of STT-MRAM initially in a parallel state, for varying bi-quadratic coupling strengths between FM1 and FM2. Structures for which FM1 and FM2 relaxed to an antiparallel state with an interlayer angle $90° < \theta < 179°$ lie between the arms of the green contour. The current is applied in the positive z-direction, which is polarized by FM2 and exerts a torque on the comparatively easy FM3. The FM3 switching current is minimized for interlayer angles $\sim 122° < \theta < 179°$. Included are two explanatory insets, which correspond to the pre- and post-switch state of the bit for $J_1 = 2.0 \times 10^{-3}\mathrm{J/m^2}$ and $J_2 = 1.4 \times 10^{-3}\mathrm{J/m^2}$. The region below and to the right of the green contour corresponds to perfectly collinear structures, where the switching torque is created by random variation in the magnetic moment caused by the numerical inaccuracy in Python/magnum.pi. The numerical labels within the plot are given in $10^{12}\mathrm{A/m^2}$. This figure is provided without insets in Appendix D.2.

Chapter 5

Discussion

The existing market availability of computer memory is dominated by semiconductor memory, each type of which introduces its own problems [6, 7]. DRAM is cheap and dense, but devours power, SRAM is fast and efficient, but is unacceptably expensive and low density. However, STT-MRAM with a non-collinear angle between FM1 and FM2 has *already* been shown to substantially improve on both of these architectures *and* on other existing implementations of MRAM [20], which are limited by a few key design choices which reduce the potential for improvements over traditional memory. Sources predict as much as a 60% reduction in main-memory energy draw for STT-MRAM over DRAM [18].

STT-MRAM has two primary components: a driving transistor for both reading with giant or tunneling magnetoresistance and writing with spin-transfer torque, and a magnetic nanopillar. The nanopillar stores a single bit and is composed of a stable reference layer against which GMR/TMR is measured and a free layer that reverses by STT according to memory state. With the design proposed by previous experimental research at the PNMD lab in collaboration with the PFM lab, the reference layer itself comprises two ferromagnetic layers arranged as a synthetic antiferromagnet around a nonmagnetic spacer: a lower layer, FM1, to pin the middle (reference) layer, FM2. These layers provide the stable foundations of the memory bit, compensating for each other's external magnetic moments when properly oriented and spin-filtering switching currents to produce a writing torque on FM3. It is critical that FM1 and FM2 are thermally stable, non-collinearly arranged, and compatible with various materials. The fabrication and control of coupling angle in these layers is already well studied in thin films by the PNMD lab [21], but key questions remain when these design goals are applied to nanostructures.

5.1 Summary and impact of results

The research presented here has shown that $r \approx 70$nm is a good upper bound on the radius of the FM layers of non-collinear STT-MRAM, based on the condition of homogeneity of relaxed states. Likewise, there is a lower bound on the radius of $r \approx 15$nm imposed by the

thermal stability condition of $\Delta \geq 60$ and the requirement for out-of-plane samples that $K_s < K_u$, though this depends strongly on the layer thickness. This is comparable to existing designs with $\sim$ 20nm junction sizes [10, 9, 51], including devices that have been scaled for 4Gb modules [17]. Section 4.1.1 provides a minimum strength of magnetocrystalline anisotropy to ensure an out-of-plane magnetization, which is known to improve thermal stability [52], and Sections 4.1.1, 4.1.1, and 4.1.1 provide a verification of the behaviour of the most important energy terms as implemented in magnum.pi, including the discovery of a critical software bug in the simulation of J_2. A set of simulations of SAFs with varying coupling strength and anisotropies show a critical design constraint to maximize the range of attainable J_1 and J_2 [54, 21] that produce desirable non-collinear antiparallel coupling angles: K_{u_1} and K_{u_2} *must* be asymmetric and not both larger than $5 \times 10^5 \mathrm{J/m}^3$. As well, these simulations reveal a complex and varied energy landscape, where local magnetic energy minima appear for certain choices of K_{u_1}, K_{u_2}, J_1, and J_2. These minima are of great interest, and may create difficulties when manufacturing these layers or reduce the thermal stability of the memory.

I compared the dynamics of layer reversal in magnum.pi against an accepted theory of magnetodynamics, the Stoner-Wohlfarth criterion, which shows that magnum.pi does indeed converge to the theoretical values of coercivity as layer coherency increases. These results also show that all layers will switch decoherently (through domain-wall propagation) at the radii in question. Lastly, by combining the above results in a full three-layer STT-MRAM structure, I showed that switching current is consistently minimized in structures with non-collinear FM1 and FM2, with the lowest current for layers with interlayer angle $122^\circ < \theta < 179^\circ$, created by experimentally attainable values of J_1 and J_2. While the numerical values for the critical current are not to be treated as accurate due to simplifications in the model, these simulated switching currents are consistent with results for this metric in other work [9, 11, 12].

5.2 Use of magnum.pi

With the exception of very early testing of the biquadratic coupling term, magnum.pi met and exceeded all expectations of performance and capabilities. However, it is important to be cognizant of the limitations of such models. Most magnetic properties are exogenous to the simulations, rather than arising physically from quantum effects or properties of the lattice. Where J_1 is known to vary in sign and magnitude with spacer thickness according to the theory of RKKY coupling [57], it is instead a constant depending on user input, and couples independently of the thickness of the spacer. All values of J_1 and J_2 that are considered "attainable" in this work are taken from the PNMD lab's sputtered thin films and experimental measurements on the VSM [54, 21]. Likewise, where the spin-filtering of STT arises through electronic interactions with the lattice, the polarization is instead a variable

set by the user in the `SpinTorqueSlonczewski` class of magnum.pi. This can be addressed by instead using the `SpinDiffusionSolver` in future work, though this comes with a dramatic increase in computational workload. The effects of thermal fluctuations were not included in any of the simulations in this work, though magnum.pi does support it. While magnum.pi does not strictly *require* a high-performance computing cluster, it is certainly beneficial for the many simulations required for each phase plot in this work. For context, if each of the 3600 simulations for the figures of Section 4.2.2 took an average of 21 minutes, each would take 52.5 days to produce on a single-threaded personal computer. Unfortunately, learning to properly employ the vast resources of Cedar takes some time. Accurate simulation of J_2 was required for this work, which makes magnum.pi the best choice out of the available options for commercial and open source micromagnetic simulation environments [39]. I feel that I am now able to practically employ magnum.pi for most uses as a daily tool in what is primarily an experimental, rather than computational, lab.

5.3 Future work

The PNMD lab does not currently have the infrastructure to produce or measure nanopillars and it is regrettable that I was unable to verify the results of this thesis with experimental measurements. Further work in magnum.pi will include an investigation of the effect of non-collinear coupling on the GMR/TMR ratio and on switching speed, as well as a thorough study of the presence of local minima in SAF relaxation states through a string method approach to barrier estimation.

Bibliography

[1] T. Kennedy, "History of computer memory," 2018, last accessed 21 August 2022. [Online]. Available: https://www.cs.odu.edu/~tkennedy/cs300/development/Public/M01-HistoryOfComputerMemory/index.html

[2] A. V. Khvalkovskiy, D. Apalkov, S. Watts, R. Chepulskii, R. S. Beach, A. Ong, X. Tang, A. Driskill-Smith, W. H. Butler, P. B. Visscher, D. Lottis, E. Chen, V. Nikitin, and M. Krounbi, "Basic principles of STT-MRAM cell operation in memory arrays," *Journal of Physics D: Applied Physics*, vol. 46, no. 7, p. 074001, feb 2013. [Online]. Available: https://doi.org/10.1088/0022-3727/46/7/074001

[3] I. Ennen, D. Kappe, T. Rempel, C. Glenske, and A. Hütten1, "Giant magnetoresistance: Basic concepts, microstructure, magnetic interactions and applications," *Sensors*, vol. 16, p. 904, 2016. [Online]. Available: https://www.ncbi.nlm.nih.gov/pmc/articles/PMC4934330/

[4] A. A. Mamun, G. Guo, and C. Bi, *Hard Disk Drive: Mechatronics and Control*. CRC Press, 2007. [Online]. Available: https://www-taylorfrancis-com.proxy.lib.sfu.ca/books/mono/10.1201/9781420004106/hard-disk-drive-abdullah-al-mamun-chao-bi-guoxiao-guo

[5] W.-K. Cheng, P.-Y. Shen, and X.-L. Li, "Retention-aware dram auto-refresh scheme for energy and performance efficiency," *Micromachines*, vol. 10, no. 9, 2019. [Online]. Available: https://www.mdpi.com/2072-666X/10/9/590

[6] H. Choi, D. Hong, J. Lee, and S. Yoo, "Reducing dram refresh power consumption by runtime profiling of retention time and dual-row activation," *Microprocessors and Microsystems*, vol. 72, p. 102942, 2020. [Online]. Available: https://www.sciencedirect.com/science/article/pii/S0141933119302686

[7] T. Coughlin, *Digital Storage in Consumer Electronics: The Essential Guide*. Springer International Publishing, 2017. [Online]. Available: https://books.google.ca/books?id=K2dCDwAAQBAJ

[8] G. Phillips, "How does cpu cache work and what are l1, l2, and l3 cache?" 2023, last accessed 11 March 2023. [Online]. Available: https://www.makeuseof.com/tag/what-is-cpu-cache

[9] D. H. Kang and M. Shin, "Critical switching current density of magnetic tunnel junction with shape perpendicular magnetic anisotropy through the combination of spin-transfer and spin-orbit torques," *Scientific Reports*, vol. 11, no. 1, p. 22842, 2021. [Online]. Available: https://doi.org/10.1038/s41598-021-02185-3

[10] L. Wu, S. Rao, M. Taouil, E. J. Marinissen, G. Sankar Kar, and S. Hamdioui, "Impact of magnetic coupling and density on stt-mram performance," in *2020 Design, Automation & Test in Europe Conference & Exhibition*, 2020, pp. 1211–1216.

[11] D. Aravinthan, P. Sabareesan, and M. Daniel, "Effect of biquadratic coupling on current induced magnetization switching in co/cu/ni-fe nanopillar," *AIP Conference Proceedings*, vol. 1731, no. 1, p. 130032, 2016. [Online]. Available: https://aip.scitation.org/doi/abs/10.1063/1.4948138

[12] ——, "Impact of biquadratic coupling on critical current density in co/cu/ni-fe nanopillar," *AIP Conference Proceedings*, vol. 1728, no. 1, p. 020443, 2016. [Online]. Available: https://aip.scitation.org/doi/abs/10.1063/1.4946494

[13] M. Arora, "Origin of perpendicular magnetic anisotropy in co/ni multilayers," Ph.D. dissertation, Simon Fraser University, 2017.

[14] J. Slonczewski, "Current-driven excitation of magnetic multilayers," *Journal of Magnetism and Magnetic Materials*, vol. 159, no. 1, pp. L1–L7, 1996. [Online]. Available: https://www.sciencedirect.com/science/article/pii/0304885396000625

[15] E. Technologies, "Everspin | the mram company," 2008, last accessed 8 September 2022. [Online]. Available: https://www.everspin.com/

[16] E. Design, "4-mbit device is first commercially available mram," 2006, last accessed 8 September 2022. [Online]. Available: https://www.electronicdesign.com/technologies/dsps/article/21776170/4mbit-device-is-first-commercially-available-mram

[17] S.-W. Chung, T. Kishi, J. W. Park, M. Yoshikawa, K. S. Park, T. Nagase, K. Sunouchi, H. Kanaya, G. C. Kim, K. Noma, M. S. Lee, A. Yamamoto, K. M. Rho, K. Tsuchida, S. J. Chung, J. Y. Yi, H. S. Kim, Y. Chun, H. Oyamatsu, and S. J. Hong, "4gbit density stt-mram using perpendicular mtj realized with compact cell structure," in *2016 IEEE International Electron Devices Meeting (IEDM)*, 2016, pp. 27.1.1–27.1.4.

[18] E. Kültürsay, M. Kandemir, A. Sivasubramaniam, and O. Mutlu, "Evaluating stt-ram as an energy-efficient main memory alternative," in *2013 IEEE International Symposium on Performance Analysis of Systems and Software (ISPASS)*, 2013, pp. 256–267.

[19] S. S. Lab, "High performance spin transfer torque magnetic random access memory (stt-mram) devices," 2021, last accessed 8 September 2022. [Online]. Available: https://sfu.portals.in-part.com/eYdN1RADgzBG?utm_source=technologies&utm_medium=portal

[20] R. Sbiaa, "Magnetization switching by spin-torque effect in off-aligned structure with perpendicular anisotropy," *Journal of Physics D: Applied Physics*, vol. 46, no. 39, p. 395001, sep 2013. [Online]. Available: https://doi.org/10.1088/0022-3727/46/39/395001

[21] Z. R. Nunn, C. Abert, D. Suess, and E. Girt, "Control of the noncollinear interlayer exchange coupling," *Science Advances*, vol. 6, no. 48, p. eabd8861, 2020. [Online]. Available: https://www.science.org/doi/abs/10.1126/sciadv.abd8861

[22] M. E. McHenry and D. E. Laughlin, "19 - magnetic properties of metals and alloys," in *Physical Metallurgy*, 5th ed., D. E. Laughlin and K. Hono, Eds. Oxford: Elsevier, 2014, pp. 1881–2008. [Online]. Available: https://www.sciencedirect.com/science/article/pii/B9780444537706000198

[23] L. Pauling, "A theory of ferromagnetism," *Proceedings of the National Academy of Sciences of the United States of America*, vol. 39, no. 6, pp. 551–560, 1953. [Online]. Available: http://www.jstor.org/stable/88708

[24] T. McKinnon, "Study of magnetic interlayer coupling in synthetic antiferromagnets for use in mram devices," Ph.D. dissertation, Simon Fraser University, 2020.

[25] C. Eyrich, "Exchange stiffness in thin-film cobalt alloys," Master's thesis, Simon Fraser University, 2012.

[26] M. Stiles, *Interlayer Exchange Coupling*. Berlin, Heidelberg: Springer Berlin Heidelberg, 2005, pp. 99–142. [Online]. Available: https://doi.org/10.1007/3-540-27163-5_4

[27] M. Arora, N. R. Lee-Hone, T. Mckinnon, C. Coutts, R. Hübner, B. Heinrich, D. M. Broun, and E. Girt, "Magnetic properties of co/ni multilayer structures for use in STT-RAM," *Journal of Physics D: Applied Physics*, vol. 50, no. 50, p. 505003, nov 2017. [Online]. Available: https://doi.org/10.1088/1361-6463/aa97fa

[28] Z. R. Nunn and E. Girt, "Non-collinear coupling across ruco and rufe alloys," *arXiv: Materials Science*, 2019. [Online]. Available: https://arxiv.org/abs/1901.07055

[29] M. Coey, *Magnetism and Magnetic Materials*. Cambridge University Press, 2010. [Online]. Available: https://www.cambridge.org/core/books/magnetism-and-magnetic-materials/AD3557E2D4538CAA8488A8C1057313BC

[30] P. Bruno, "Tight-binding approach to the orbital magnetic moment and magnetocrystalline anisotropy of transition-metal monolayers," *Phys. Rev. B*, vol. 39, pp. 865–868, Jan 1989. [Online]. Available: https://link.aps.org/doi/10.1103/PhysRevB.39.865

[31] D. D. Tang and Y.-J. Lee, *Magnetic Memory: Fundamentals and Technology*. Cambridge: Cambridge University Press, 2010, vol. 9780521449649.

[32] B. Dieny and M. Chshiev, "Perpendicular magnetic anisotropy at transition metal/oxide interfaces and applications," *Rev. Mod. Phys.*, vol. 89, p. 025008, Jun 2017. [Online]. Available: https://link.aps.org/doi/10.1103/RevModPhys.89.025008

[33] C. Abert, "Micromagnetics and spintronics: models and numerical methods," *The European Physical Journal B*, vol. 92, no. 6, jun 2019. [Online]. Available: https://doi.org/10.1140%2Fepjb%2Fe2019-90599-6

[34] The Royal Swedish Academy of Sciences, "The discovery of giant magnetoresistance," *AAPPS Bulletin*, vol. 17, pp. 2–11, Dec 2007. [Online]. Available: http://userpages.irap.omp.eu/~sbottinelli/Downloads/BE_8_TheDiscoveryOfGMR.pdf

[35] J. Slonczewski, "Currents and torques in metallic magnetic multilayers," *Journal of Magnetism and Magnetic Materials*, vol. 247, no. 3, pp. 324–338, 2002. [Online]. Available: https://www.sciencedirect.com/science/article/pii/S0304885302002913

[36] C. Abert, "magnum.pi, release 3.6.5," 2021, last accessed 8 September 2022. [Online]. Available: http://w3techs.com/technologies/overview/content_language/all

[37] C. Abert, L. Exl, F. Bruckner, A. Drews, and D. Suess, "magnum.fe: A micromagnetic finite-element simulation code based on fenics," *Journal of Magnetism and Magnetic Materials*, vol. 345, pp. 29–35, 2013. [Online]. Available: https://www.sciencedirect.com/science/article/pii/S0304885313004022

[38] D. Süss, "Physics of functional materials," 2022, last accessed 8 September 2022. [Online]. Available: https://ufind.univie.ac.at/en/pvz_sub.html?id=727

[39] J. Leliaert and J. Mulkers, "Tomorrow's micromagnetic simulations," *Journal of Applied Physics*, vol. 125, no. 18, p. 180901, 2019. [Online]. Available: https://doi.org/10.1063/1.5093730

[40] C. Geuzaine and J.-F. Remacle, "A three-dimensional finite element mesh generator with built-in pre- and post-processing facilities," 2009, last accessed 8 September 2022. [Online]. Available: https://gmsh.info/

[41] M. Donahue and D. Porter, "Oommf user's guide, version 1.0," *Interagency Report NISTIR 6376*, 1999. [Online]. Available: https://math.nist.gov/oommf/oommf_cites.html

[42] A. Vansteenkiste, "mumax3, gpu-accelerated micromagnetism," 2013, last accessed 8 September 2022. [Online]. Available: https://mumax.github.io/

[43] M. Boissonneault, "Technical documentation," 2022, last accessed 8 September 2022. [Online]. Available: https://docs.alliancecan.ca/wiki/Technical_documentation

[44] Wiki, "Cedar," 2021, last accessed 8 September 2022. [Online]. Available: https://docs.alliancecan.ca/wiki/Cedar

[45] SchedMD, "slurm workload manager documentation," 2022, last accessed 12 March 2023. [Online]. Available: https://slurm.schedmd.com/

[46] lustre, "slustre* software release 2.x," 2017, last accessed 12 March 2023. [Online]. Available: https://doc.lustre.org/lustre_manual.xhtml

[47] gentoo linux, "Welcome to the gentoo wiki!" 2023, last accessed 12 March 2023. [Online]. Available: https://wiki.gentoo.org/wiki/Main_Page

[48] I. Y. Loh, "Mechanism and assessment of spin transfer torque (stt) based memory," Master's thesis, Massachusetts Institute of Technology, 2009.

[49] E. Ipek, F. Longnos, S. Xiao, and W. Yang, "Vertical writes: Closing the throughput gap between deeply scaled stt-mram and dram," *IEEE computer architecture letters*, vol. 17, no. 2, pp. 151–154, 2018.

[50] *1Gb Non-Volatile ST-DDR4 Spin-transfer Torque MRAM*, Everspin Technologies, 10 2022, rev. 1.3.

[51] T. P. Almeida, S. Lequeux, A. Palomino, R. C. Sousa, O. Fruchart, I.-L. Prejbeanu, B. Dieny, A. Masseboeuf, and D. Cooper, "Quantitative visualization of thermally enhanced perpendicular shape anisotropy stt-mram nanopillars," *Nano letters*, vol. 22, no. 10, pp. 4000–4005, 2022.

[52] E. E. Fullerton, S. Mangin, D. Ravelosona, J. A. Katine, M. J. Carey, and B. D. Terris, "Current-induced magnetization reversal in nanopillars with perpendicular anisotropy," *Nature materials*, vol. 5, no. 3, pp. 210–215, 2006.

[53] J. Osborn, "Demagnetizing factors of the general ellipsoid," *Physical review*, vol. 67, no. 11-12, pp. 351–357, 1945.

[54] T. McKinnon, B. Heinrich, and E. Girt, "Thermally robust synthetic antiferromagnetic fixed layers containing fecob for use in stt-mram devices," *Journal of Magnetism and Magnetic Materials*, vol. 546, p. 168646, 2022. [Online]. Available: https://www.sciencedirect.com/science/article/pii/S0304885321008829

[55] W. E, W. Ren, and E. Vanden-Eijnden, "Simplified and improved string method for computing the minimum energy paths in barrier-crossing events," *The Journal of Chemical Physics*, vol. 126, no. 16, p. 164103, 2007. [Online]. Available: https://doi.org/10.1063/1.2720838

[56] N. Perrissin, N. Caçoilo, G. Gregoire, S. Lequeux, L. Tillie, N. Strelkov, A. Chavent, S. Auffret, L. D. Buda-Prejbeanu, R. C. Sousa, L. Vila, I. L. Prejbeanu, and B. Dieny, "Perpendicular shape anisotropy spin transfer torque-mram: determination of pillar tilt angle from 3d stoner–wohlfarth astroid analysis," *Journal of Physics D: Applied Physics*, vol. 52, no. 50, p. 505005, oct 2019. [Online]. Available: https://dx.doi.org/10.1088/1361-6463/ab4215

[57] M. Arora, N. R. Lee-Hone, T. Mckinnon, C. Coutts, R. Hübner, B. Heinrich, D. M. Broun, and E. Girt, "Magnetic properties of co/ni multilayer structures for use in stt-ram," *Journal of physics. D, Applied physics*, vol. 50, no. 50, p. 505003, 2017.

Appendix A

Example Gmsh meshing script

The following is an example of a Gmsh meshing ".geo" input script. First, radial points are defined, which are connected into a line loop. This line loop is filled in to form a surface, which is extruded into each of the desired layers using previously-defined physical dimensions. Lastly, each surface is labeled for later referencing and filled in to create volumes.

```
ml = 2.0; // mesh length, determined by smaller of two exchange lengths
radius = 20; // all dimensions in nanometers

// Layer Thicknesses
tFM1 = 3.00; // thickness of the first layer, all nm
tS1 = 0.50; // thickness of spacer layer
tFM2 = 3.00; // thicknesss of the second layer
tS2 = 2.50; // thickness of second spacer layer
tFM3 = 2.00; // thicknesss of the free layer

// Number of discretization layers per layer
nzFM1 = 1; // FM1
nzS1 = 1; // Spacer 1 (coupling)
nzFM2 = 1; // FM2
nzS2 = 1; // Spacer layer (GMR/TMR)
nzFM3 = 1; // FM3, Free layer

// Define perimeter points for initial surface
Point(1) = {0, 0, 0, ml}; // Geometrical Entity: Point/Line/Surface/Volume (# of ent.) {x
↪  coord, y coord, z coord, mesh length};
Point(2) = {radius, 0, 0, ml};
Point(3) = { 0, radius, 0, ml};
Point(4) = {-radius, 0, 0, ml};
Point(5) = { 0,-radius, 0, ml};

// Define straight connecting lines for rhombus surface
// Line(1) = {2,3};
// Line(2) = {3,4};
// Line(3) = {4,5};
// Line(4) = {5,2};

// Define arcing connecting lines for circular surface
Circle(1) = {2,1,3}; // {start, middle, end};
```

```
Circle(2) = {3,1,4}; // {start, middle, end};
Circle(3) = {4,1,5}; // {start, middle, end};
Circle(4) = {5,1,2}; // {start, middle, end};

// Create line loop from separate lines
Line Loop(5) = {1,2,3,4}; // Order matters -> head to tail

// Create 2D surface from line loop
Surface(1) = {5};

// Extrude 2D surface into 3D volumes for each layer
s0[] = Extrude{0, 0, tFM1} {Surface{1}; Layers{nzFM1};}; // use initial surface created manually to extrude to a volume
s1[] = Extrude{0, 0, tS1} {Surface{s0[0]}; Layers{nzS1};}; //use the upper surface of the newly extruded volume
s2[] = Extrude{0, 0, tFM2} {Surface{s1[0]}; Layers{nzFM2};};
s3[] = Extrude{0, 0, tS2} {Surface{s2[0]}; Layers{nzS2};};
s4[] = Extrude{0, 0, tFM3} {Surface{s3[0]}; Layers{nzFM3};};

// Create physicalized surfaces of volumes for each edge of surfaces
Physical Surface('1') = {1}; // give ID of the surface that you want to assign the ID in (ID). Bottom of bottom layer
Physical Surface('2') = {s0[0]}; // top of FM1
Physical Surface('3') = {s1[0]}; // top of S1
Physical Surface('4') = {s2[0]}; // top of FM2
Physical Surface('5') = {s3[0]}; // top of S2
Physical Surface('6') = {s4[0]}; // top of FM3
// Can assign readable IDs, ie. Physical Surface('interface4')

// Create volumes for each layer of MRAM
Physical Volume(1) = {s0[1]}; // FM1
Physical Volume(2) = {s1[1]}; // S1
Physical Volume(3) = {s2[1]}; // FM2
Physical Volume(4) = {s3[1]}; // S2
Physical Volume(5) = {s4[1]}; // FM3
```

Appendix B

Example SLURM submission script

The following is an example of a SLURM ".slrm" HPC job script. This script requests 75 separate jobs to run on 75 nodes on the Cedar supercomputer, where all 48 cores and 187GB of RAM on each node is reserved. Each simulation on each core on each node is allowed to run for a maximum of one hour, and the output directory is named according to the pair of K_{u_1} and K_{u_2} for that simulation. In total, this script requests 3600 simulations, which corresponds to the 3600 pairwise combinations of J_1 and J_2 required for the phase plots in Section 4.1.2. The job is restricted to run on Intel Skylake and Intel Cascade Lake CPUs because of incompatibilities of certain CPU instruction sets used by compiled code.

```
#!/bin/bash
#
#SBATCH -J J1J2Phase # short description, max 14 chars
#SBATCH --mail-type=ALL #
#SBATCH --mail-user=<user@email.ca> # to notify you of completion/failure
#SBATCH --constraint=[skylake|cascade] # restrict jobs to run on nodes w/ certain CPU architectures
#
#SBATCH --nodes=1 # number of nodes
#SBATCH --ntasks-per-node=48 # number of cores per node
#SBATCH --time=01:00:00 # time you want sims to run (hh:mm:ss)
#SBATCH --mem=0 # memory per node, set to 0 b/c requesting whole node
#SBATCH --array=0-74 # job array, will request n-m separate jobs

: ${SLURM_ARRAY_TASK_ID:=0} # for testing

################ Sim 1, Ku1 = 5e5 J/m3, Ku2 = 5e5 J/m3 #################
simName=s1_5 # Run 5: Large J1J2 Range, PP Ordered Start, 40ns
# simName=s1_9 # Run 9: Large J1J2 Range, AP Ordered Start, 100ns, No Precession, high exch

################ Sim 2, Ku1 = 7.5e5 J/m3, Ku2 = 7.5e5 J/m3 #################
# simName=s2_5 # Run 5: Large J1J2 Range, PP Ordered Start, 40ns
# simName=s2_9 # Run 9: Large J1J2 Range, AP Ordered Start, 100ns, No Precession, high exch
```

```
23
24  ################ Sim 3, Ku1 = 7.5e5 J/m3, Ku2 = 5e5 J/m3 #################
25  # simName=s3_5 # Run 5: Large J1J2 Range, PP Ordered Start, 40ns
26  # simName=s3_8 # Run 8: Large J1J2 Range, AP Ordered Start, 50ns, No Precession
27
28  ################ Sim 4, Ku1 = 1e6 J/m3, Ku2 = 5e5 J/m3 #################
29  # simName=s4_4 # Run 4: Small J1J2 Range, PP Ordered Start, 40ns
30  # simName=s4_5 # Run 5: Large J1J2 Range, PP Ordered Start, 40ns
31  # simName=s4_8 # Run 8: Large J1J2 Range, AP Ordered Start, 50ns, No Precession
32
33  ################ Sim 5, Ku1 = 1e6 J/m3, Ku2 = 7.5e5 J/m3 #################
34  # simName=s5_4 # Run 4: Small J1J2 Range, PP Ordered Start, 40ns
35  # simName=s5_5 # Run 5: Large J1J2 Range, PP Ordered Start, 40ns
36  # simName=s5_8 # Run 8: Large J1J2 Range, AP Ordered Start, 50ns, No Precession
37
38  ################ Sim 6, Ku1 = 1e6 J/m3, Ku2 = 1e6 J/m3 #################
39  # simName=s6_5 # Run 5: Large J1J2 Range, PP Ordered Start, 40ns
40  # simName=s6_8 # Run 8: Large J1J2 Range, AP Ordered Start, 50ns, No Precession
41  # simName=s6_9 # Run 9: Large J1J2 Range, AP Ordered Start, 100ns, No Precession, high
    ↪  exch
42
43  ####################################
44
45  FDDIR=/scratch/gmlertzm
46  MAGNUMPI_IMG=/home/gmlertzm/.magnumpi/magnum.pi_v3.9.5c.sif
47  FIREDRAKE_CACHE=$FDDIR/.firedrake_cache
48  module load singularity/3.8
49
50  jobDir=$SLURM_SUBMIT_DIR
51  projectName=$(basename ${jobDir})
52  scriptName=run_$projectName
53  outDir=output_job_${projectName}_${simName}
54  logs=$outDir/${projectName}_${simName}_logs
55  mkdir -p $outDir $logs $FIREDRAKE_CACHE
56
57  TASKS_PER_NODE=$SLURM_NTASKS_PER_NODE
58  RANKs=()
59  PIDs=()
60
61  echo projectName: $projectName
62  echo simName: $simName
63  echo SLURM_SUBMIT_DIR: $SLURM_SUBMIT_DIR
64  echo SLURM_JOB_NODELIST: $SLURM_JOB_NODELIST
65  echo SLURM_JOB_CPUS_PER_NODE: $SLURM_JOB_CPUS_PER_NODE
66  echo SLURM_MEM_PER_NODE: $SLURM_MEM_PER_NODE
67
68  # Run run_script.py with given rank, direct to outdir
69  for i in `seq $TASKS_PER_NODE`
70  do
71      RANKs[$i]=$(printf "%04d" $(($SLURM_ARRAY_TASK_ID * $TASKS_PER_NODE + $i - 1)))
72      singularity exec -H $PWD:/home/ -B $FIREDRAKE_CACHE:/firedrake/.cache $MAGNUMPI_IMG
    ↪  bash -c "source /firedrake/bin/activate && OMP_NUM_THREADS=1 python
    ↪  ${scriptName}.py --rank=${RANKs[$i]} --output
    ↪  ${outDir}/${projectName}_output_${RANKs[$i]}" > ${logs}/run_${RANKs[$i]}.out 2>
    ↪  ${logs}/run_${RANKs[$i]}.err &
73      PIDs[$i]=$!
74      echo "Starting Rank ${RANKs[$i]} (PID: ${PIDs[$i]})"
75  done
```

```
76
77  # Wait for background jobs
78  for i in `seq $TASKS_PER_NODE`
79  do
80      wait ${PIDs[$i]}
81      echo "Rank ${RANKs[$i]} (PID: ${PIDs[$i]}): finished with return value $?"
82  done
```

Appendix C

Example magnum.pi simulation scripts

C.1 SAF phase plot

The following is an example of a "static" magnum.pi running script. This code is set up to vary two inputs across predefined ranges: the bilinear coupling constant (J_1) and the biquadratic coupling constant (J_2) for two identical layers of a synthetic antiferromagnet (SAF) for one pair of values of K_{u_1} and K_{u_2}. The value of each parameter for a particular run of the simulation is chosen by the '-r' flag at runtime, which is ultimately enumerated by a batch script. The code produces a simulation that relaxes from either a parallel or antiparallel initial state. The time and the magnetization of each layer are saved to a log file, while the total magnetization, anisotropy energy, exchange energy, and interlayer exchange energy are saved to ".vtk" files for viewing in Paraview. Scalars are saved every 10 timesteps and fields are saved every 10000 timesteps of a 100ns relaxation. This script produced the data for the figures of Section 4.1.2.

```
from magnumpi import *
import numpy as np
import argparse
from pathlib import Path
import os
import itertools as iter

# Define parameter and parameter values to vary with rank
paramDescription = 'J1, J2' # description of program
defaultParam = 0 # default argument

# Read in rank arguments from batch script and set up arg list
parser = argparse.ArgumentParser(description = paramDescription) # sets a description for arguments
parser.add_argument('-o', '--output', default = 'output', type = str) # sets arguments to the rank from incoming batch script
parser.add_argument('-r', '--rank', default = defaultParam, type = int) # sets arguments to the rank from incoming batch script
```

```
args = parser.parse_args() # sets args to rank from batch script

# Large Sim:
J1List = np.linspace(0.00, 5.00, 60)*1e-3 # for J/m^2
J2List = np.linspace(0.00, 4.00, 60)*1e-3 # for J/m^2

# Small Sim:
# J1List = np.linspace(0.00, 2.00, 60)*1e-3 # for J/m^2
# J2List = np.linspace(1.00, 1.50, 60)*1e-3 # for J/m^2

# PP Sim:
initFM1ZComp = 1.0 # positive z dir
initFM2ZComp = 1.0 # positive z dir
A = 1.3e-11 #J/m, exchange interaction

# AP Sim:
# initFM1ZComp = -1.0 # negative z dir
# initFM2ZComp = 1.0 # positive z dir
# A = 1.3e-10 #J/m, exchange interaction

params = list(iter.product(J1List, J2List))
paramValues = params[args.rank] # set paramValues to proper value according to rank
J1 = -1*paramValues[0] # set J1 to a particular value according to rank
J2 = -1*paramValues[1] # set J2 to a particular value according to rank

################ Sim 1, Ku1 = 5e5 J/m3, Ku2 = 5e5 J/m3 #################
Ku1 = 5e5 # J/m3
Ku2 = 5e5 # J/m3

################ Sim 2, Ku1 = 7.5e5 J/m3, Ku2 = 7.5e5 J/m3 #################
# Ku1 = 7.5e5 # J/m3
# Ku2 = 7.5e5 # J/m3

################ Sim 3, Ku1 = 7.5e5 J/m3, Ku2 = 5e5 J/m3 #################
# Ku1 = 7.5e5 # J/m3
# Ku2 = 5e5 # J/m3

################ Sim 4, Ku1 = 1e6 J/m3, Ku2 = 5e5 J/m3 #################
# Ku1 = 1e6 # J/m3
# Ku2 = 5e5 # J/m3

################ Sim 5, Ku1 = 1e6 J/m3, Ku2 = 7.5e5 J/m3 #################
# Ku1 = 1e6 # J/m3
# Ku2 = 7.5e5 # J/m3

################ Sim 6, Ku1 = 1e6 J/m3, Ku2 = 1e6 J/m3 #################
# Ku1 = 1e6 # J/m3
# Ku2 = 1e6 # J/m3

# Create saving directories
fileName = Path(__file__).stem # retrieve name of running script
outDir = args.output
projectName = fileName.split('_')[-1] # retrieve name of project from running script
relaxDir = f'{outDir}/relax_{projectName}_r={args.rank}' # creates a directory for each
↪  rank

print(f'Relaxing {projectName} with {paramDescription} = {J1:0.1e}, {J2:0.1e}, Ku1 =
↪  {Ku1:0.1e}, Ku2 = {Ku2:0.1e}, rank = {args.rank}')
```

```
72
73  # Read mesh
74  mesh = Mesh(f'mesh_{projectName}/mesh_{projectName}.msh')
75
76  # Initialize state and group properties for each layer
77  state = State(
78      mesh, # define which mesh should be used for simulations
79      cell_domains = {
80          'magnetic': (1, 3), # taking volume labels from mesh, assign own names
81          'conducting': (1, 2, 3), # define volumes to be used in sim, name and categorize
    ↪  them.
82          'FM1': 1,
83          'FM2': 3,
84          'spacer': 2
85      },
86      facet_domains = {
87          'interface1': 2, # all physical surfaces that you need, top of FM1
88          'interface2': 3 # top of spacer
89      },
90      scale = 1e-9 # all mesh dimensions in nm, thus: scale must be set to 1e-9
91  )
92
93  # Define material parameters for all magnetic layers
94  state.material = Material(
95      alpha = 1.0, # damping 0 -> 1
96      Ms = 900e3, # sat mag, A/m
97      A  = A # exchange interaction, J/m (bulk Cobalt)
98  )
99
100 # Define material parameters for FM1
101 state.material['FM1'] = Material(
102     Ku = Ku1, # uniaxial anisotropy, J/m3
103     Ku_axis = (0, 0, 1) # anisotropy axis
104 )
105
106 # Define material parameters for FM2
107 state.material['FM2'] = Material(
108     Ku = Ku2, # uniaxial anisotropy, J/m3
109     Ku_axis = (0, 0, 1) # anisotropy axis
110 )
111
112 # Initialize Energy Terms
113 exchange  = ExchangeField()
114 aniso     = UniaxialAnisotropyField()
115 iexchange = BiquadraticInterlayerExchangeField(J1, J2) # if J2 = 0 -> it becomes
    ↪  equivalent to InterlayerExchange
116 demag     = DemagField()
117
118 # Define state.h as the effective field which includes all the desired energy terms
119 state.h      = exchange + aniso + iexchange + demag
120 state.exch   = exchange.h
121 state.aniso  = aniso.h
122 state.iexch  = iexchange.h
123 state.demag  = demag.h
124
125 ###########################################################################
126 # Relax the structure from random init
127 ###########################################################################
```

```
128
129 # Initialize magnetizations of magnetic layers
130 state['FM1'].m = Constant(( 0.0, 0.0, initFM1ZComp)) # initial magnetization of FM1
131 state['FM2'].m = Constant(( 0.0, 0.0, initFM2ZComp)) # initial magnetization of FM1
132
133 # Initialize LLG
134 llg = LLGSolver(no_precession = True) # solve LLG to relax initial state
135
136 # Set up logging
137 Timer.enable(skip = 1)
138 logger = Logger(
139     relaxDir, # Logger('name of dir')
140     ['t', 'm[FM1]', 'm[FM2]'], # First list is scalars: m[FM1] is avg mag in FM1,
    ↪  log.dat
141     ['m', 'aniso', 'exch', 'iexch'], # Second list is fields, VTKs
142     scalars_every = 10, # output scalars every 50 entries,
143     fields_every = 10000 # fields every 10000
144 )
145
146 # Run simulation
147 while state.t < 100e-9: # time to relax
148     logger << state
149     llg.step(state, 1e-12) # step by picosecond
150 Timer.print_report()
151
152 print(f'Finished relaxing {projectName} with {paramDescription} = {J1:0.1e}, {J2:0.1e},
    ↪  Ku1 = {Ku1:0.1e}, Ku2 = {Ku2:0.1e}, rank = {args.rank}')
```

C.2 Switching current of an STT-MRAM structure

The following is an example of a "dynamic" magnum.pi running script. This code is set up to vary inputs across a predefined range: the bilinear and biquadratic interlayer exchange coupling constant (J_1 and J_2) for the coupling between the bottom two layers of a three-layer STT-MRAM stack. The values of J_1 and J_2 for a particular run of the simulation are chosen by the '-r' flag at runtime, which is ultimately enumerated by a batch script. The code produces a simulation that initially relaxes from a randomized magnetization, and then uses the relaxed state as the input to simulate a spin-transfer torque (STT) write operation, which is performed by a linearly increasing current density in a direction opposite to that of FM3 z-direction. The time, the current density, and the magnetization of each layer are saved to a log file, while the total magnetization, anisotropy energy, exchange energy, and interlayer exchange energy are saved to ".vtk" files for viewing in Paraview. For the simulation of STT, scalars are saved every 10 timesteps and fields are saved every 4000 timesteps of a 20ns relaxation. This script produced the data for the figures of Section 4.2.2.

```
1 from magnumpi import *
2 import numpy as np
3 import scipy as sp
4 import argparse
5 from pathlib import Path
6 import itertools as iter
7
```

```
# Define parameter and parameter values to vary with rank
paramDescription = 'J1J2' # description of parameter
defaultParam = 0 # default argument

# Read in rank arguments from batch script and set up arg list
parser = argparse.ArgumentParser(description = paramDescription) # sets a description for arguments
parser.add_argument('-o', '--output', default = 'output', type = str) # sets arguments to the rank from incoming batch script
parser.add_argument('-r', '--rank', default = defaultParam, type = int) # sets arguments to the rank from incoming batch script
args = parser.parse_args() # sets args to rank from batch script

# J1/J2 Lists:
J1S1List = np.linspace(0.00, 5.00, 60)*1e-3 # for J/m^2
J2S1List = np.linspace(0.00, 4.00, 60)*1e-3 # for J/m^2
params = list(iter.product(J1S1List, J2S1List))
paramValues = params[args.rank] # set paramValues to proper value according to rank
J1S1 = -1*paramValues[0] # set J1 to a particular value according to rank
J2S1 = -1*paramValues[1] # set J2 to a particular value according to rank

# simName=s1 # 20ns, phase, crit current, j0_0 = -5e10, j0_1 = -1e13, LLG in FM3, no STTS1, AP FM2/FM3
j0_0 = -5e10 # A/m2, initial applied spin torque current
j0_1 = -1e13 # A/m2, final applied spin torque current
relaxTime = 50e-9 # ns
simTime = 20e-9 # ns

# simName=s1 # 20ns, phase, crit current, j0_0 = -5e10, j0_1 = -1e13, LLG in FM3, no STTS1, PP FM2/FM3
# j0_0 = 5e10 # A/m2, initial applied spin torque current
# j0_1 = 1e13 # A/m2, final applied spin torque current
# relaxTime = 50e-9 # ns
# simTime = 20e-9 # ns

# Create saving directories
fileName = Path(__file__).stem # retrieve name of running script
slrmOutDir = args.output
projectName = fileName.split('_')[-1] # retrieve name of project from running script
relaxDir = f'{slrmOutDir}/relax_{projectName}_J2S1={J2S1:0.1e}' # creates a directory for each value of J2
simDir = f'{slrmOutDir}/data_{projectName}_J2S1={J2S1:0.1e}' # creates a directory for each value of J2

print(f'Relaxing {projectName} with J1S1 = {J1S1:0.1e}, J2S1 = {J2S1:0.1e}, rank = {args.rank}')

# Read mesh
mesh = Mesh(f'mesh_{projectName}/mesh_{projectName}.msh')

# Initialize state and group properties for each layer
state = State(
    mesh, # define which mesh should be used for simulations
    cell_domains  = {
        'magnetic': (1, 3, 5), # taking volume labels from mesh, assign own names
        'conducting': (1, 2, 3, 4, 5), # define volumes to be used in sim, name and categorize them.
        'FM1': 1, # bottom of SAF
```

```
        'spacer1': 2, # first spacer
        'FM2': 3, # top of SAF
        'spacer2': 4, # second spacer
        'FM3': 5, # free layer
    },
    facet_domains = {
        'bottomContact': 1, # all physical surfaces that you need, bottom of FM1
        'interface1': 2, # top of FM1
        'interface2': 3, # top of spacer 1
        'interface3': 4, # top of FM2
        'interface4': 5, # top of spacer 2
        'topContact': 6 # all physical surfaces that you need, bottom of FM1
    },
    scale = 1e-9 # all mesh dimensions in nm, thus: scale must be set to 1e-9
)

# Define material parameters for each magnetic layer individually
# FM1 is based on RAM4-64
state.material['FM1'] = Material(
    Ms = 900e3, # sat mag, A/m
    # Ms = 1.150e6, # sat mag, A/m
    A  = 1.3e-11, # exchange interaction, J/m3 (bulk Cobalt)
    Ku = 1.0e6, # uniaxial anisotropy, J/m3
    # Ku = 1.11e6, # uniaxial anisotropy, J/m3
    Ku_axis = (0, 0, 1) # anisotropy direction
)

# FM2 is based on RAM4-61
state.material['FM2'] = Material(
    Ms = 900e3, # sat mag, A/m
    # Ms = 1.08e6, # sat mag, A/m
    A  = 1.3e-11, # exch interaction, J/m3 (bulk Cobalt)
    Ku = 5.0e5, # uniaxial anisotropy, J/m3
    # Ku = 9.18e5, # uniaxial anisotropy, J/m3
    Ku_axis = (0, 0, 1) # anisotropy dir
)

# FM3 (FL) is based on RAM4-38
state.material['FM3'] = Material(
    Ms = 7.4e5, # sat mag, A/m
    A  = 1.3e-11, # exch interaction, J/m3 (bulk Cobalt)
    Ku = 4.3e5, # uniaxial anisotropy, J/m3
    Ku_axis = (0, 0, 1) # anisotropy dir
)

# Initialize Energy Terms
exchange    = ExchangeField()
aniso       = UniaxialAnisotropyField()
demag       = DemagField()
iexchangeS1 = BiquadraticInterlayerExchangeField(
    A1 = J1S1,
    A2 = J2S1, # if J2 = 0 this becomes equivalent to InterlayerExchange
    interface1 = 'interface1',
    interface2 = 'interface2',
    spacer_region = 'spacer1'
)

# Define state.h as the effective field which includes all the desired energy terms
```

```
state.h      = exchange + aniso + iexchangeS1 + demag
state.exch   = exchange.h
state.aniso  = aniso.h
state.iexch  = iexchangeS1.h
state.demag  = demag.h

##########################################################################
# Relax the structure from random init
##########################################################################

# Initialize magnetizations of magnetic layers
state['FM1'].m = Constant(( 0.0, 0.0, 1.0)) # initial magnetization of FM1, positive z dir
state['FM2'].m = Constant(( 0.0, 0.0, 1.0)) # initial magnetization of FM2, positive z dir
state['FM3'].m = Constant(( 0.0, 0.0, -1.0)) # initial magnetization of FM3, negative z dir

# High damping for relaxation
state.material['magnetic'].alpha = Constant(1.0) # damping 0 -> 1

# Initialize LLG
llg = LLGSolver() # solve LLG to relax initial state

# Set up logging of relaxation
Timer.enable(skip = 1)
logger = Logger(
    relaxDir, # Logger('name of dir')
    ['t', 'm[FM1]', 'm[FM2]', 'm[FM3]'], # First list is scalars: m[FM1] is avg mag in FM1, .dat
    ['m', 'aniso', 'exch', 'iexch'], # Second list is fields, VTKs
    scalars_every = 100, # output scalars every 100 entries
    fields_every = 25000 # fields every 25000
)

# Run relaxation
while state.t < relaxTime: # time to relax
    logger << state
    llg.step(state, 1e-12) # step by picosecond
Timer.print_report()

print(f'Finished relaxing {projectName} with J1S1 = {J1S1:0.1e}, J2S1 = {J2S1:0.1e}, rank = {args.rank}')

##########################################################################
# Apply Current
##########################################################################

llg.reset() # clear state from relaxation
state.t = 0.0 # reset time of sim

print(f'Simulating {projectName} with J1S1 = {J1S1:0.1e}, J2S1 = {J2S1:0.1e}, rank = {args.rank}')

# Initialize Spin Torque Transfer term for Spacer 2
sttS2 = SpinTorqueSlonczewski(
    P = 0.7, # polarization degree of current (X% of current is polarized to a given spin), 0.7 is reasonable
```

```
    Gamma = 0.8, # spin torque param
    interface1 = 'interface3', # top of FM2
    interface2 = 'interface4', # top of S2
    spacer_region = 'spacer2'
)

# Define time-dependent current
interpCurrent = ExprTimeInterpolator({
    0:       (0.0, 0.0, j0_0),
    simTime: (0.0, 0.0, j0_1)} # xyz Components of the applied current
)

# Define state.h as the effective field which includes all the desired energy terms
state.h = exchange + aniso + iexchangeS1 + sttS2 + demag
state.j = interpCurrent

# Low damping for simulation
state.material['magnetic'].alpha = Constant(0.1)

# Re-initialize LLG
llg = LLGSolver(region = 'FM3', rtol = 1e-7, atol = 1e-7)

# Set up logging for simulation
Timer.enable(skip = 1)
logger = Logger(
    simDir, # Logger('name of dir')
    ['t', 'j', 'm[FM1]', 'm[FM2]', 'm[FM3]'], # First list is scalars: m[FM1] is avg mag
    ↪  in FM1, VTKs
    ['m', 'aniso', 'exch', 'iexch'], # Second list is fields
    scalars_every = 10, # output scalars every 10 entries,
    fields_every = 4000 # fields every 1000
)

# Run simulation
while state.t < simTime: # time to simulate
    logger << state
    llg.step(state, 1e-12) # step by picosecond
Timer.print_report()

print(f'Finished simulating {projectName} with J1S1 = {J1S1:0.1e}, J2S1 = {J2S1:0.1e},
↪  rank = {args.rank}')
```

Appendix D

Supplemental Figures

D.1 SAF interlayer coupling angle

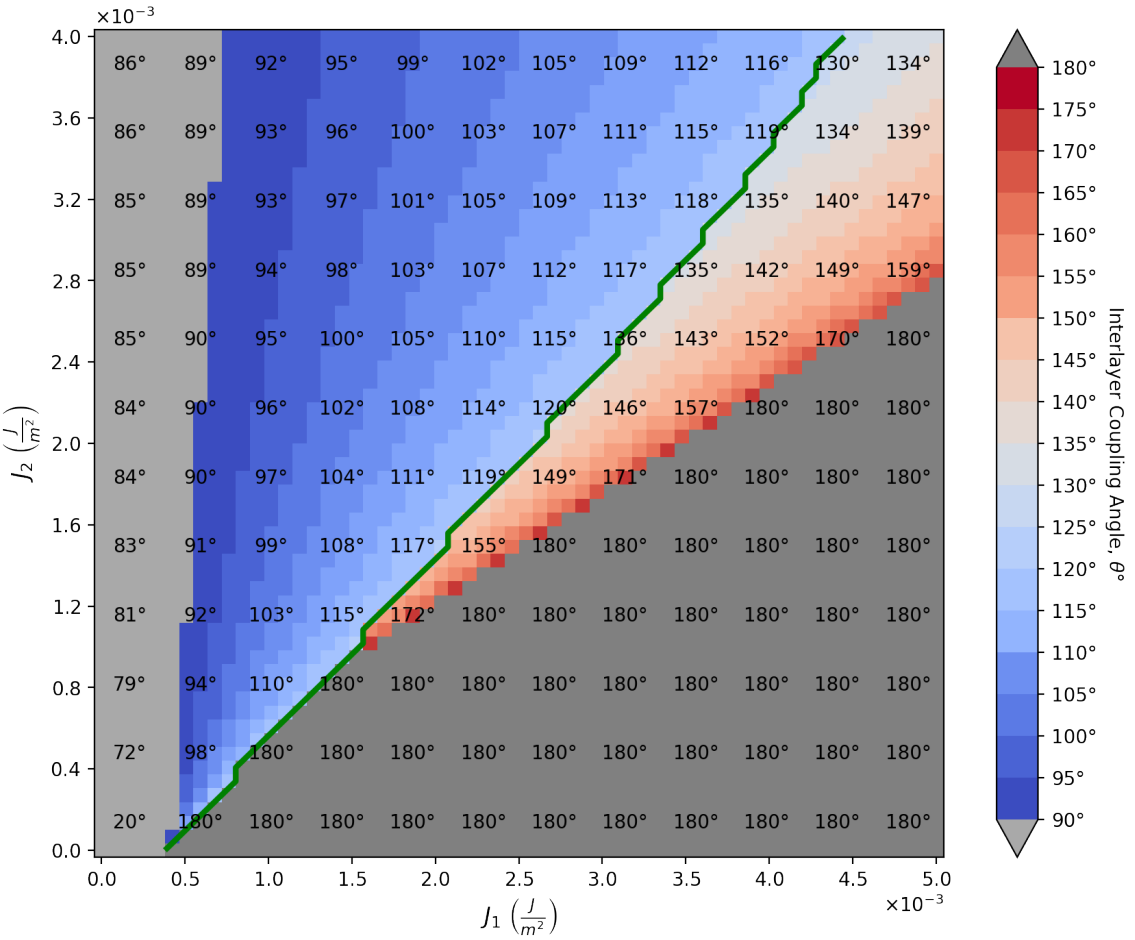

Figure D.1: SAF interlayer angle phase plot for a 20nm radius FM1 and FM2, plotted as J_1 vs J_2. $K_{u_1} = 5.0 \times 10^5 \mathrm{J/m^3}$, $K_{u_2} = 5.0 \times 10^5 \mathrm{J/m^3}$, with parallel initial conditions. Interlayer angles below 90° are coloured light grey, while interlayer angles above 179° are coloured dark grey to enhance the detail of the colourmap over the range of angles of interest. Structures to the left of the green contour relaxed to an approximately parallel configuration, with the z-component of magnetization in both layers having the same sign, while structures to the right relaxed to an approximately antiparallel configuration, with the z-component of magnetization in each layer having the opposite sign. Values of J_1 and J_2 for which the structure relaxed to an antiparallel, non-collinear arrangement are of interest for use in STT-MRAM.

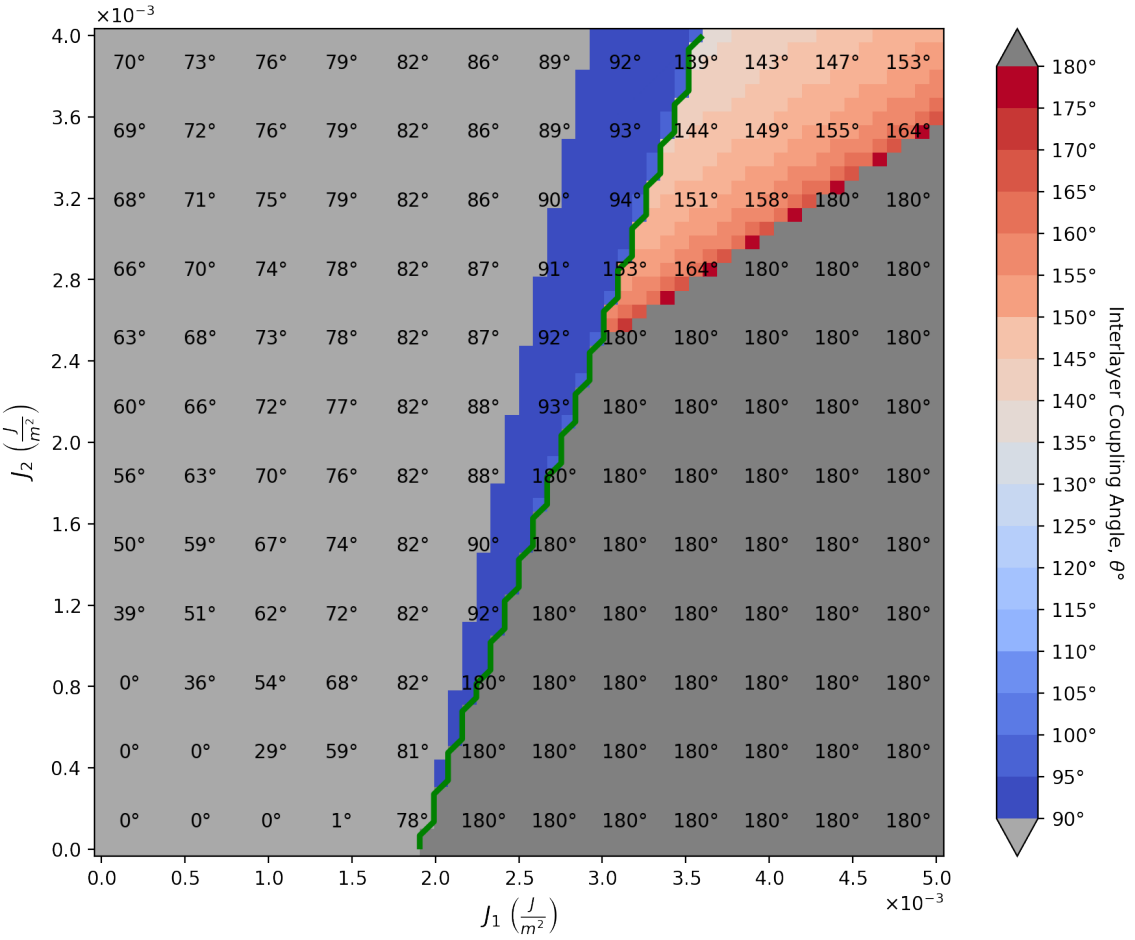

Figure D.2: SAF interlayer angle phase plot for a 20nm radius FM1 and FM2, plotted as J_1 vs J_2. $K_{u_1} = 1.0 \times 10^6 \mathrm{J/m^3}$, $K_{u_2} = 1.0 \times 10^6 \mathrm{J/m^3}$, with parallel initial conditions. Interlayer angles below 90° are coloured light grey, while interlayer angles above 179° are coloured dark grey. Structures to the left of the green contour relaxed to an approximately parallel configuration, with the z-component of magnetization in both layers having the same sign, while structures to the right relaxed to an approximately antiparallel configuration, with the z-component of magnetization in each layer having the opposite sign. Values of J_1 and J_2 for which the structure relaxed to an antiparallel, non-collinear arrangement are of interest for use in STT-MRAM.

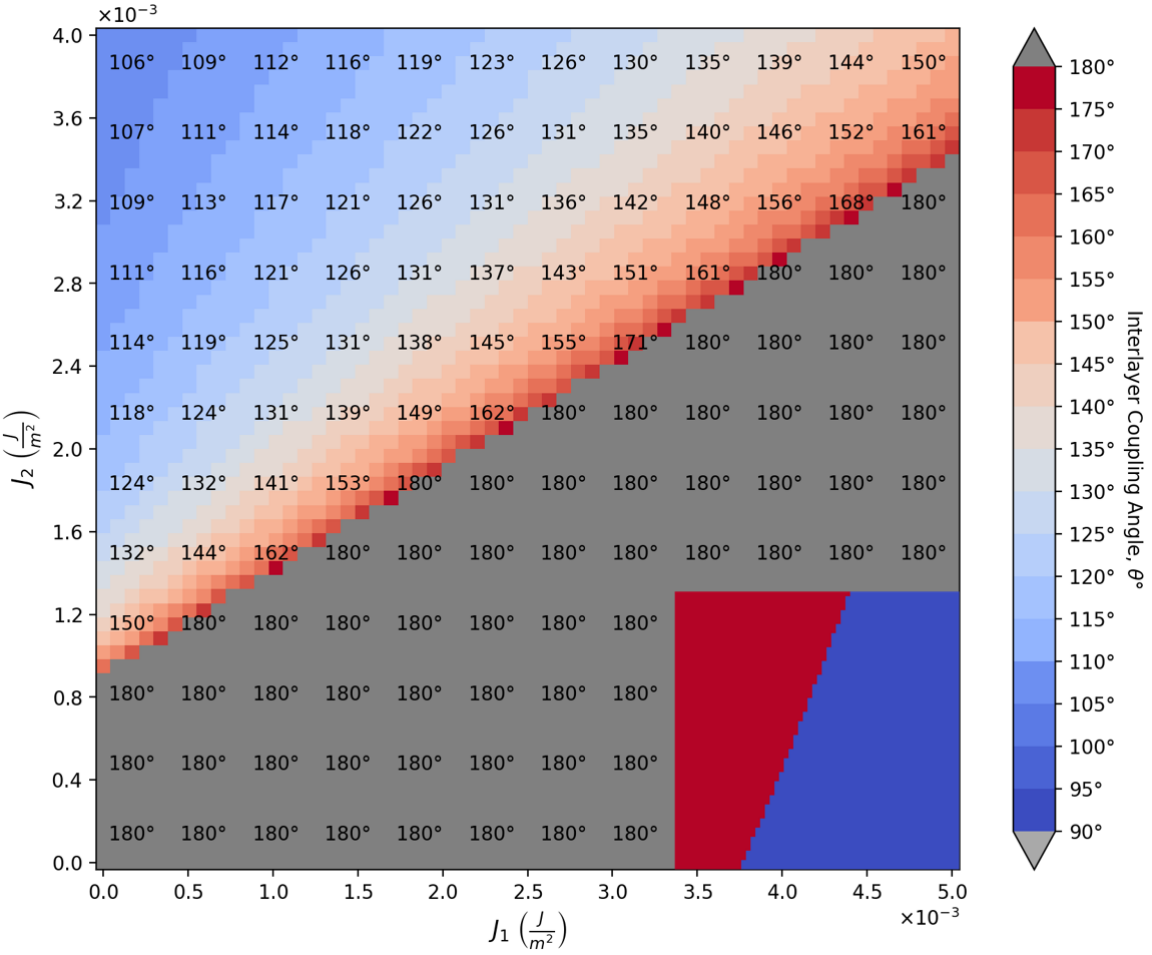

Figure D.3: SAF interlayer angle phase plot for a 20nm radius FM1 and FM2, plotted as J_1 vs J_2. $K_{u_1} = 1.0 \times 10^6 \mathrm{J/m^3}$, $K_{u_2} = 1.0 \times 10^6 \mathrm{J/m^3}$, with antiparallel initial conditions. Interlayer angles below 90° are coloured light grey, while interlayer angles above 179° are coloured dark grey. Structures to the left of the green contour relaxed to an approximately parallel configuration, with the z-component of magnetization in both layers having the same sign, while structures to the right relaxed to an approximately antiparallel configuration, with the z-component of magnetization in each layer having the opposite sign. Values of J_1 and J_2 for which the structure relaxed to an antiparallel, non-collinear arrangement are of interest for use in STT-MRAM. On the bottom right, an inset compares the regions of antiparallel and parallel relaxed states in this and Fig. D.2, where red indicates that the structures are in different minima.

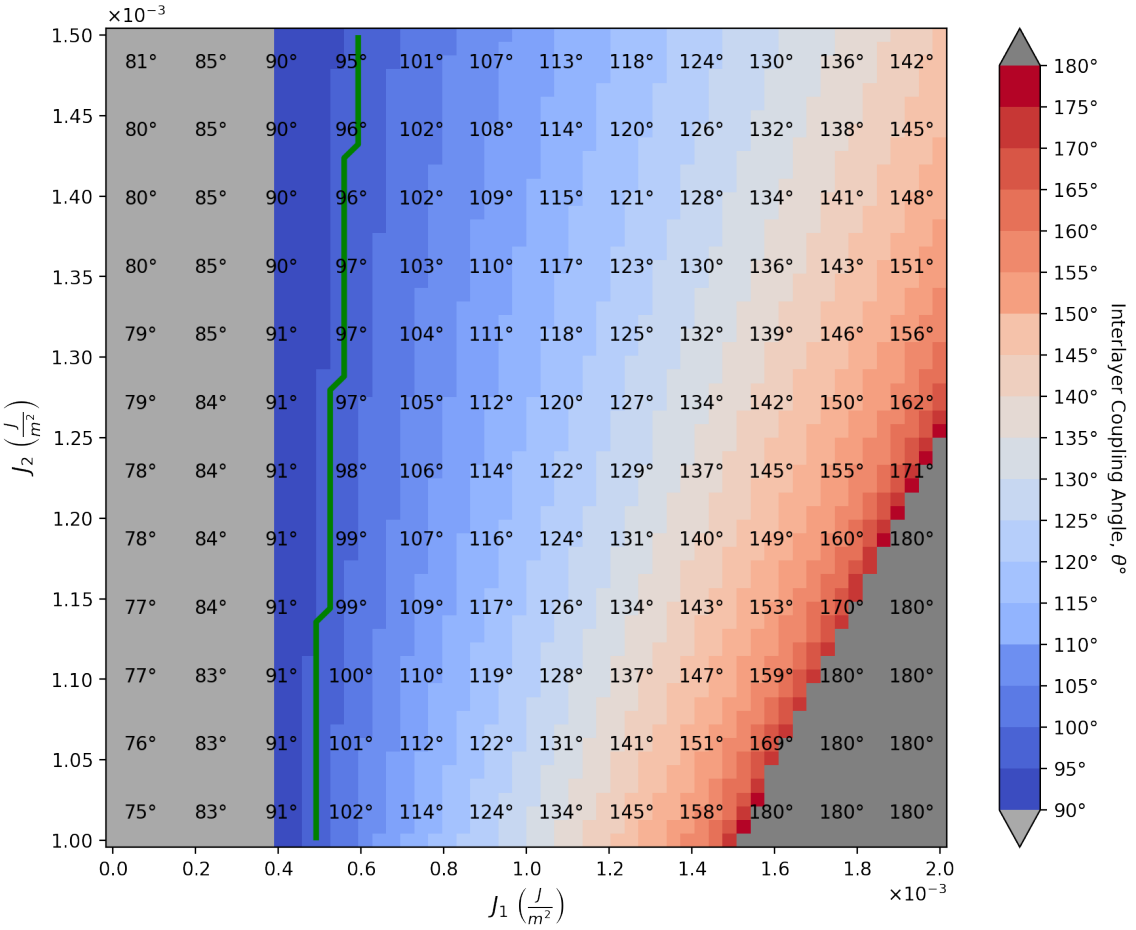

Figure D.4: SAF interlayer angle phase plot for a 20nm radius FM1 and FM2, plotted as J_1 vs J_2. $K_{u_1} = 1.0 \times 10^6 \mathrm{J/m^3}$, $K_{u_2} = 5.0 \times 10^5 \mathrm{J/m^3}$, with parallel initial conditions. Interlayer angles below 90° are coloured light grey, while interlayer angles above 179° are coloured dark grey. Structures to the left of the green contour relaxed to an approximately parallel configuration, with the z-component of magnetization in both layers having the same sign, while structures to the right relaxed to an approximately antiparallel configuration, with the z-component of magnetization in each layer having the opposite sign. Values of J_1 and J_2 for which the structure relaxed to an antiparallel, non-collinear arrangement are of interest for use in STT-MRAM. Equivalent to Fig. 4.12, but only simulated and plotted over ranges of J_1 and J_2 that are currently considered reasonable to reproduce.

D.2 Dependence of switching current on J_2

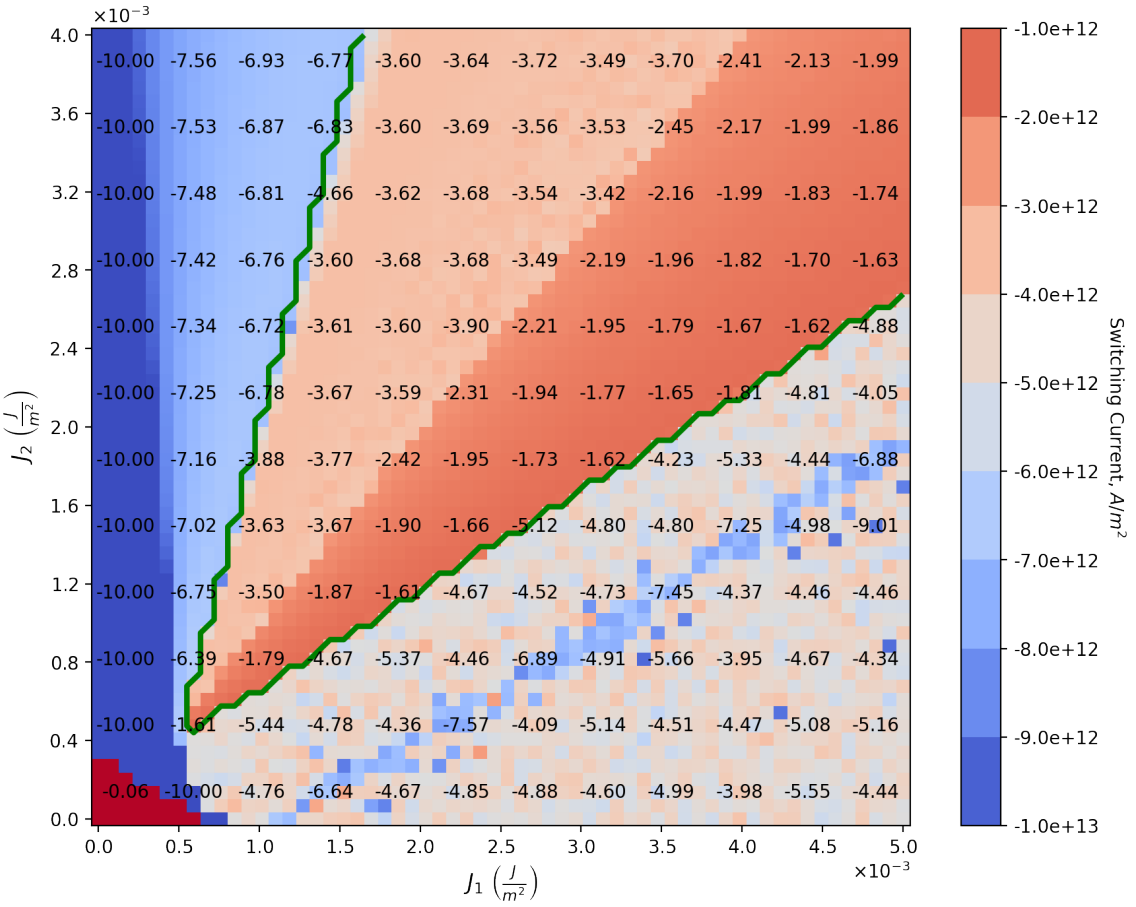

Figure D.5: Switching current of STT-MRAM initially in an antiparallel state, for varying biquadratic coupling strengths between FM1 and FM2. Structures for which FM1 and FM2 relaxed to an antiparallel state with an interlayer angle $90° < \theta < 179°$ lie between the arms of the green contour. The current is applied in the negative z-direction, which interacts with the moment of FM2, exerting a torque on the comparatively easy FM3 through reflection of minority carriers. The FM3 switching current is minimized for interlayer angles $\sim 125° < \theta < 179°$. The numerical labels within the plot are given in $10^{12}\mathrm{A/m^2}$. The region below and to the right of the green contour corresponds to perfectly collinear structures, where the switching torque is created by random variation in the magnetic moment caused by the numerical inaccuracy in Python/magnum.pi.

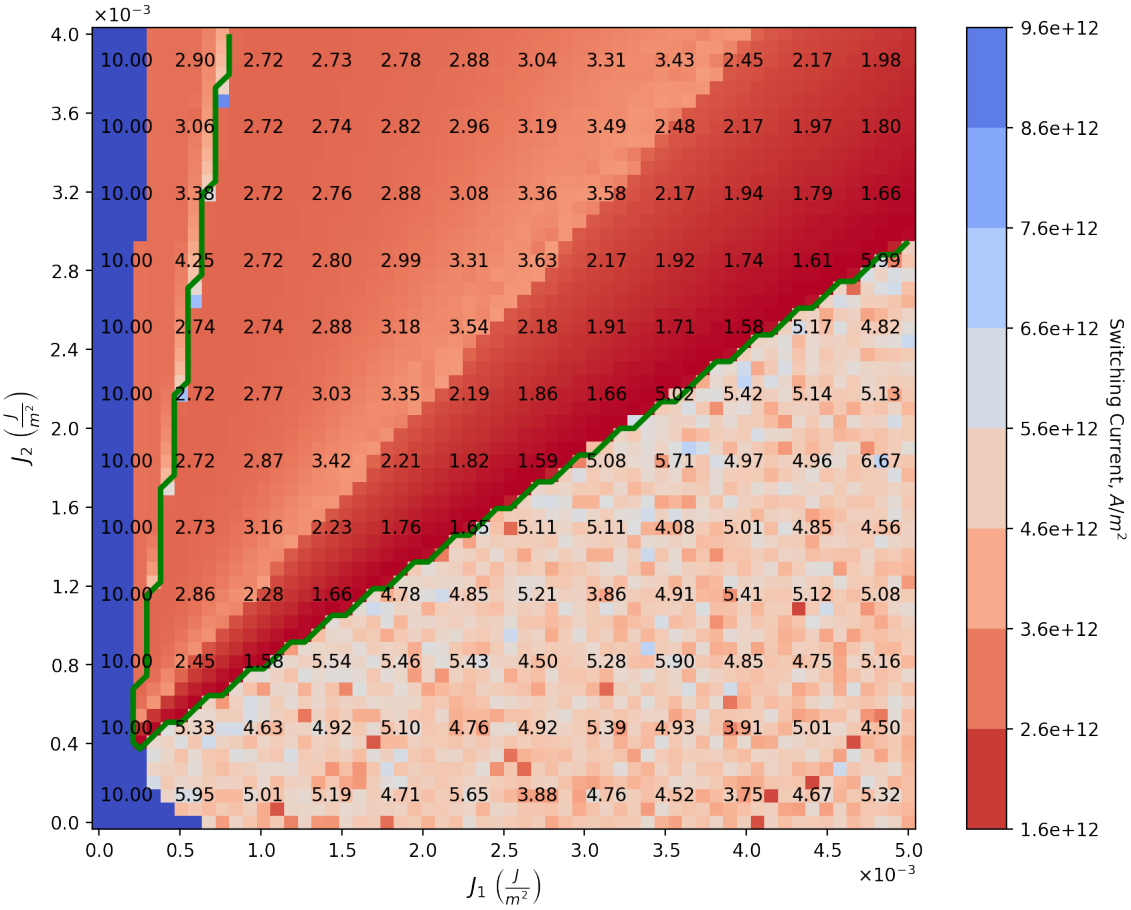

Figure D.6: Switching current of STT-MRAM initially in a parallel state, for varying bi-quadratic coupling strengths between FM1 and FM2. Structures for which FM1 and FM2 relaxed to an antiparallel state with an interlayer angle $90° < \theta < 179°$ lie between the arms of the green contour. The current is applied in the positive z-direction, which is polarized by FM2 and exerts a torque on the comparatively easy FM3. The FM3 switching current is minimized for interlayer angles $\sim 122° < \theta < 179°$. The numerical labels within the plot are given in $10^{12}\mathrm{A/m}^2$. The region below and to the right of the green contour corresponds to perfectly collinear structures, where the switching torque is created by random variation in the magnetic moment caused by the numerical inaccuracy in Python/magnum.pi.